High Frequency VLBI Studies of Sagittarius A* and NRAO 530

Inaugural-Dissertation

zur

Erlangung des Doktorgrades

der Mathematisch-Naturwissenschaftlichen Fakultät

der Universität zu Köln

vorgelegt von

Ru-Sen Lu

aus Hebei, China

Köln 2010

Berichterstatter:

1.Gutachter: Prof. Dr. J. Anton Zensus
2.Gutachter: Prof. Dr. Andreas Eckart

Tag der mündlichen Prüfung: 13.07.2010

To my parents and the rest of my familly

Abstract

Compact radio sources (Kellermann & Pauliny-Toth 1981) are widely accepted to be associated with supermassive black holes at the centers of active galaxies. Very long baseline interferometry (VLBI) observations at short millimeter wavelengths offer the unique advantage to look "deeper" into the central core regions. In this thesis we study two compact radio sources (Sagittarius A* and NRAO 530) with high frequency VLBI techniques.

As a starting point, we give in Chapter 1 a general introduction to observational properties of Active galactic nuclei (AGNs) and a theoretical basis. In Chapter 2, the compact radio source at the center of the Milky Way, Sagittarius A*, is reviewed. In Chapter 3, the technical basis of VLBI is outlined and then the difficulties of VLBI (and therefore the ways to improve) at short millimeter wavelengths are discussed.

Due to its proximity, Sagittarius A* has the largest apparent event horizon of any black hole candidate and therefore it provides a unique opportunity for testing the SMBH paradigm. However, direct imaging of the nucleus is only accessible at short millimeter wavelengths due to the scatter broadening. In Chapter 4, we present results of an inter-day VLBI monitoring of Sagittarius A* at wavelengths of 13, 7, and 3 mm during a global observing campaign in 2007. We measure the flux density and source structure and study their variability on daily time scales.

In addition to the VLBI monitoring of the Galactic Center, we present in Chapter 5 results of multi-epoch multi-frequency VLBI observations of the blazar NRAO 530. NRAO 530 is an optically violent variable (OVV) source and was observed as a VLBI calibrator in our observations of Sagittarius A*. We investigate the spectral properties of jet components, their frequency-dependent position shifts, and variability of flux density and structure on daily time scales. Analysis of archival data over the last ten years allows us to study the detailed jet kinematics.

Finally, a summary and future outlook is given in Chapter 6.

Zusammenfassung

Nach gängigem Verständnis befinden sich in den Zentren aktiver Galaxienkerne große, sogenannte super-massive schwarze Löcher. Diese aktiven Galaxienkerne manifestieren sich als kompakte Radioquellen am Himmel. Mittels der Methode der interkontinentalen radiointerferometrischen Beobachtung (VLBI: Very Long Baseline Interferometry) bei kurzen Millimeter-Wellenängen, ergibt sich die einzigartige Möglichkeit diese Zentralregionen mit höchster Winkelauflösung zu untersuchen. In dieser Doktorarbeit werden die Ergebnisse einer interferometrischen VLBI-Untersuchung von zwei besonders prominenten kompakten Radioquellen mittels der Methode von Millimeter-VLBI vorgestellt. Bei diesen beiden Quellen handelt es sich um die Zentralquelle im Galaktischen Zentrum (Sagittarius A, Sgr A*) und um den entfernten Quasar NRAO530.

Im einleitenden Kapitel 1 dieser Arbeit wird zuerst eine allgemeine und zusammenfassende Darstellung der Aktiven Galaxienkerne (AGK, engl. AGN), und der sie beschreibenden zu Grunde liegenden theoretischen Modelle gegeben. Im zweiten Kapitel wird die kompakte Radioquellen Sgr A* im galaktischen Zentrum und der momentane Stand der wissenschaftlichen Forschung hierzu, in einer allgemeinen Übersicht zusammengefaßt. Im Kapitel 3 werden die technischen Grundlagen und die technischen Grenzen von VLBI-Beobachtungen bei Millimeter-Wellenlängen dargestellt und diskutiert.

Auf Grund der relativ geringen Entfernung zur Erde, hat Sagittarius A * den größten scheinbaren Ereignishorizont-Durchmesser aller bekannten Schwarz-Loch Kandidaten, und erlaubt somit auf einmalige Weise das Schwarz-Loch Paradigma eines (aktiven) Galaxienkernes durch direkte Beobachtungen zu testen. Bedingt durch die Bildverschmierung bei langen Radiowellen durch interstellare Szintillation, ist eine direkte Kartierung des Kerns und der unmittelbaren Umgebung des Schwarzen Loches nur bei kurzen Millimeter-Wellenlängen und mit VLBI möglich. In Kapitel 4 dieser Arbeit präsentiere ich die Resultate einer neuen VLBI-Beobachtungskampagne von 10 Tagen Dauer, die Teil einer umfassenderen multi-spektralen Messkampagne auf Sgr A* im

Mai 2007 war. Die VLBI Beobachtungen wurden bei drei Wellenlängen (13 mm, 7 mm, und 3 mm) durchgeführt und durch Einzelteleskop-Messungen ergänzt. Ziel dieser Beobachtungen war das Erfassen möglicher Flussdichtevariabilität und die Suche nach Variationen der Quellstruktur mit hoher zeitlicher Auflösung auf einer Skala von Tagen.

Ergänzend zum VLBI-Monitoring von Sgr A*, zeige und diskutiere ich in Kapitel 5 dieser Arbeit die Ergebnisse der 3-Frequenz-VLBI Beobachtungen des optisch stark variablen Quasars NRAO 530 (ein OVV Blazar). Diese kompakte extragalaktische Radioquelle wurde als VLBI Kalibrator und System-Test Quelle in den oben beschriebenen VLBI Beobachtungen von Sgr A* mitbeobachtet. Die Daten erlauben eine detaillierte Kartierung des Jets von NRAO530, die Untersuchung der spektralen Eigenschaften der Jet-Komponenten, die Messung einer frequenzabhängigen Positionsverschiebung, sowie die Charakterisierung der Flussdichte- und Strukturvariabilität auf einer Zeitskala von 1-10 Tagen. Ergänzt werden die hier vorgestellten Millimeter-VLBI Beobachtungen durch eine umfassende Analyse vorliegender Archiv-VLBI-Daten aus den vergangenen 10 Jahren. Damit ist ein detailiertes Studium der Jet-Kinematik über diesen Zeitraum möglich.

Im letzen Kapitel (Kap. 6) fasse ich die Ergebnisse der vorangegangenen Kapitel nochmals zusammen und gebe einen Ausblick auf die mögliche zukünftige Entwicklung, besonders in Hinblick auf mm-VLBI bei noch kürzeren Wellenlängen.

Acknowledgements

In the beginning, I would like to thank the directors of the Max-Planck-Institut für Radioastronomie who supported me through the International Max Planck Research School (IMPRS) for Astronomy and Astrophysics. I am gratefull to Prof. Dr. Anton Zensus and Prof. Dr. Andreas Eckart for being the members of my examination board and for their support. In particular, I would like to thank Prof. Dr. Anton Zensus for giving me the opportunity to do this work in the VLBI group of the MPIfR and Prof. Dr. Endreas Eckart for his support and for providing me data of the May 2007 observing campaign.

I wish to express my deep gratitude to my supervisor Dr. Thomas Krichbaum. Thomas never got tired of giving me the advice I need to finish this work. With out his inspiring guidance, invaluable discussions, and encouragement, this study would not have been able to be fulfilled.

I will forever be grateful to my supervisor at Shanghai Astronomical Observatory, Professor Zhi-Qiang, Shen, who introduced me to astrophysical research. I thank him for his direction, dedication and encouragement through all these years.

I would also like to extend my heartfelt thanks to two other members of my IMPRS thesis committee, Dr. Arno Witzel, and Dr. Andreas Brunthaler for their invaluable advice and suggestions.

I would like to thank the various members of the VLBI group, both past and present, for their friendship and assistance. I am grateful to Dr. Richard Porcas, Priv. Doz. Dr. Silke Britzen for their help in preparing talks and the help in several other ways. I thank Dr. David Graham, Dr. Tuomas Savolainen, Dr. Andrei Lobanov, Dr. Yuri Kovalev, Dr. Alexander Pushkarev and Dr. Alan Roy for their help in my data reduction and sharing their knowledge. I am gratefull to Prof. Dr. Eduardo Ros for his support, humor and for the calling of Chinese VLBI activities to my attention from time to time. I am gratefull to Dr. Walter Alef for computer support, answering my questions, and many other helps. I thank Dr. Manolis Angelakis and Marios Karouzos for reading of the thesis, their useful comments, and also for their friendship.

I would like to thank the collaborators and colleagues at the University of Köln, in

Table of Contents

List of Tables

List of Figures

1 Introduction

AGNs exist in the centers of at least 10 per cent of all galaxies[1], in many cases out-shining their entire host galaxy. Systematic studies of bright nuclei of galaxies can be traced back to as early as 1940s when Seyfert (1943) studied non-stellar activity in a sample of galactic nuclei. However, the recognition of the significance of Seyfert's work had to wait until Baade & Minkowski (1954) identified "active galaxies" as the optical counterparts of several bright radio sources. Soon after, Baade (1956) identified the polarized optical and radio emission from the jet of M 87, verifying the synchrotron emission mechanism. This allowed Burbidge (1956) to point out that extragalactic radio sources contain tremendous amounts of energy (up to $\sim 10^{61}$ erg). Such huge energy requirements led to the "energy crisis", widely discussed in the early 1960s, especially with the discovery of quasi stellar objects (QSOs) (Schmidt 1963).

The concept that massive, (stellar-type) objects (up to $\sim 10^9 M_\odot$) power quasars or AGN, through gravitational energy was for the first time introduced by Hoyle & Fowler (1963). Zel'Dovich & Novikov (1965), Salpeter (1964), and Lynden-Bell (1969) further proposed that the huge energy release from an AGN could be explained by the accretion of matter onto a supermassive black hole (SMBH). In this picture the radio emission from AGNs is produced by a relativistic jet due to synchrotron emission of relativistic electrons moving in a magnetic field within the jet (Blandford & Königl 1979). Similarly to these luminous AGNs, Lynden-Bell & Rees (1971) considered the black hole model to be applicable also for the nucleus of the Milky Way. A compact synchrotron radio source powered by gas spiraling into a black hole was proposed as one of the "critical observations" which could test the validity of the black hole scenario. Three years later, Balick & Brown (1974) did detect such a compact radio source in the direction of the Galactic Center (GC, Morris & Serabyn 1996; Melia & Falcke 2001).

---

[1]http://ircamera.as.arizona.edu/NatSci102/lectures/agns.htm

1.1 Active Galactic Nuclei

As we will see in this section, although all AGNs consist of the same ingredients, different subclasses have distinct observational properties. Like all other fields of science, one of the primary goals of AGN studies is to develop a theory that could explain the diversity in observed properties through a single and simple model. In the current unified scheme of AGNs (Antonucci 1993; Urry & Padovani 1995), the different observational properties are interpreted as the result of different viewing angles, i.e., as a geometrical effect. In the following, the basic observational properties for a variety of subclasses are outlined and explain in the context of the unified scheme.

1.1.1 Observational Properties

Seyfert galaxies are mostly spiral galaxies. They are named after Seyfert (1943), who first pointed out that several similar galaxies with bright central regions possibly form a distinct class. The presence of broad emission lines (width from several hundreds to up to 10^4 km/s) from the bright nucleus is the key to classify a galaxy as a Seyfert. Seyfert galaxies are further divided into two subclasses (type 1 and type 2) by Khachikian & Weedman (1974), depending on whether the spectra show both "narrow" (several hundreds km/s) and "broad" emission lines (type 1), or only "narrow" lines (type 2). It is now believed that both types are in essence the same and their apparent difference is caused by different viewing angles. As we will see in the unified scheme, type 1s are those observed from a face-on view of the obscuring torus, while those observed from an edge-on view are classified as type 2s. Therefore, the presence of an optically thick dust torus surrounding the AGN core, that obscures the broad line region (BLR), is critical for the unification of Seyfert galaxies. The presence of the torus is strongly supported by the detection of polarized broad emission lines in the spectrum of NGC 1068, whose spectrum resembles a type 2 Seyfert (Antonucci & Miller 1985). The polarized flux comes from dusty clouds which scatter and polarize the light from the nucleus. In the unified scheme, Seyferts are dim, radio-quiet quasars.

Radio galaxies do not share many common characteristics, apart from being highly luminous in radio wavelengths. Their hosts are elliptical galaxies and their radio structure often shows double-sided radio lobes on kpc scales, with one or (rarely) two jets tracing back to the optical nucleus. The single-sidedness of the radio jet on pc scales is normally interpreted as a consequence of relativistic de-boosting effects. Fanaroff & Riley (1974) divided the radio galaxies into two subclasses (FR-I and FR-II) based on the morphology of their lobes. FR-Is are weaker radio sources with the so-called

"edge-darkened" extended emission and two-sided jets. On the other hand, FR-IIs are more luminous, showing edge-brightened extended emission. Most of them show symmetric lobes with co-linear structure (parallel jet axis) with hot spots either at the edge of the radio lobes or embedded within their radio structure.

Based on the width of their optical emission lines, radio galaxies can form two further sub-categories, Broad Line Radio Galaxies and Narrow Line Radio Galaxies. The former display emission lines with widths similar to those in Seyfert 1 galaxies and the latter show emission line widths similar to those in Seyfert 2 galaxies. These are thought to be radio loud counterparts of Seyfert galaxies.

Quasars were first discovered as strong radio sources, though most quasars (~ 99 %) are now known to be radio quiet when compared to their optical luminosity. Historically, the radio quiet quasars were called Quasi-Stellar Objects (QSOs), in contrast to Quasi-Stellar Radio Sources (Quasars). Now we know that they are the same kind of objects. These sources are some of the most powerful and distant AGNs. The fact that quasars are visible at enormous cosmological distances, as suggested by their high redshifts, implies a huge luminosity. In addition, the short timescales of variability (as short as hours) of their flux indicates that their enormous energy output originates in a very compact region.

Quasars are strong emitters at all wavelengths and show strong and broad emission lines of highly ionized elements (Ca, Mg, O), which is the most important observational characteristic to distinguish quasars from stars and normal galaxies. Both broad and narrow emission lines are present in their optical spectrum, similar to a Type 1 Seyfert galaxy. In this sense, quasars are powerful versions of Seyfert galaxies. The radio morphology of quasars is similar to FR-II sources with the exception that the luminosity ratio between core and jet, and lobes is higher in quasars.

Blazars is a generic term for BL Lac objects (BL Lacs) and Optically Violently Variable quasars (OVVs). Their host galaxies are often giant elliptical galaxies. BL Lac objects (named after the prototype, BL Lac) are highly variable and highly polarized. They show relatively flat and featureless spectra when compared to other AGNs. They are also compact radio sources with non-thermal continuous spectrum ranging from the radio to the γ-rays. These properties are attributed to emission from a relativistic jet oriented close to the line of sight. OVV quasars are similar to BL Lac objects in the sense that they show large and rapid optical variability. However, their spectra have features (e.g., strong broad emission lines), which are different from those in BL Lacs. It is generally believed that OVV quasars are intrinsically powerful radio galaxies while BL Lac objects are intrinsically weak radio galaxies.

1.1.2 A Unified View

The basic composition of an AGN (as illustrated in Figure 1.1) includes a SMBH (10^6–$10^9 M_\odot$) in the very center, which powers the AGN by accreting surrounding matter via a circumnuclear accretion disk. The viscous friction in the accretion disk is thought to be the mechanism, which turns gravitational energy into radiation. Accretion can convert up to 30 % of the rest mass of the in-falling gas into radiation (Thorne 1974), much larger than the efficiency of nuclear fusion ($<$ 1 %). For a quasar with typical mass of $M_\bullet = 10^8 M_\odot$, the Eddington luminosity L_{Edd}, at which the radiation pressure force balances the gravitational force, is $\frac{4\pi G M_\bullet m_p c}{\sigma_T} \sim 1.3 \times 10^{38} \frac{M_\bullet}{M_\odot} \sim 1.3 \times 10^{46}$ erg s^{-1}, where $M_\bullet$ the black hole mass, m_p the proton rest mass, and σ_T the Thomson cross section. Some material is accelerated by strong magnetic fields and ejected perpendicular to the accretion disc in the form of highly collimated jet. The jet can reach large distances, in some extreme cases, up to mega-parsec scales. Further outwards from the central engine is the BLR, surrounded by an opaque molecular torus. Above the torus is a layer of low-velocity gas which is refereed as "narrow line region" (NLR).

The opaque molecular torus and the relativistic jets seem to be two key ingredients for the classification and unification of AGNs. For a range of viewing angles, the opaque torus blocks the view towards the BLR, and we can only see the low velocity gas from the NLR. When observed at a line of sight close to the jet direction, AGNs show broad spectral lines in the optical spectrum (Type 1 AGN, e.g., Seyfert 1s, Broad Line Radio Galaxies and Type 1 Quasars), whereas when observed edge-on, the system only shows narrow emission lines from the low velocity gas in the NLR (Type 2 AGN, e.g., Seyfert 2s, Narrow Line Radio Galaxies and Type 2 Quasars). Sometimes one speaks also about Type 0 objects, which is a special case, in which we are looking directly into the jet.

AGNs can also be divided according to the radio power: "radio-loud" or "radio quiet" in terms of their ratio of radio to optical luminosity. The existence of doppler enhanced relativistic jets seems to be responsible for the radio loudness (Kellermann et al. 1989) and the radio dichotomy is perhaps related to jet production efficiency. However, it is not well understood what is the key parameter that determines the jets production. The black hole mass (Laor 2000; Liu et al. 2006b) and spin (Blandford & Znajek 1977) could be of relevance. Investigations of the jet activity in X-ray binaries suggest that the accretion rate controls the jet production efficiency (Fender et al. 2004). For radio loud AGNs, relativistic beaming effects play an important role in the radio appearance. It is accepted that low power FRIs and BL Lacs form a subgroup of objects where the relativistic jet is viewed at small angles to the observer's line of

sight. At larger viewing angles, the radio emission is dominated by the large-scale lobes and therefore, it is a classical FRI radio galaxy. Correspondingly, OVVs, radio-loud quasars, FRIIs appear to form another powerful subgroup with increasing view angle.
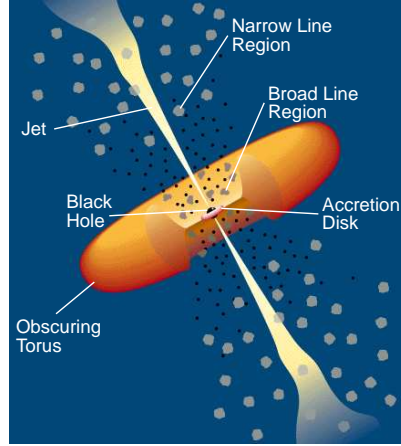
Figure 1.1: A schematic view of the unification scheme (Urry & Padovani 1995).

1.2 Basics of Relativistic Jets

1.2.1 Synchrotron Emission

Synchrotron emission (the relativistic equivalent of cyclotron emission) is generated by charged particles spiraling in a magnetic field at nearly the speed of light. It has become the research tool for the study of extragalactic jet physics since its first observation from a General Electric synchrotron accelerator in 1940s. Synchrotron radiation is observed in astronomical sources, such as jets of compact radio sources, supernova and supernova remnants, stars (non-thermal emission), galaxies and cluster halos. Synchrotron radiation shows characteristic polarization in the plane perpendicular to its propagation, which was used often in order to confirm its presence (e.g., Baade 1956).

Here we outline some characteristics of the synchrotron mechanism. Detailed derivation of the formulae can be found in (e.g., Pacholczyk 1970; Rybicki & Lightman 1979). Due to the relativistic motion of the emitting particles, the radiation is strongly beamed into a cone in the forward direction (abberation) with angular width of about $\frac{1}{\gamma}$ radians, where γ is the Lorentz factor of the electrons. The emission from a

single electron[2] has a characteristic frequency:

$$\nu_c = \frac{\gamma^2 eB}{2\pi m_e c},$$

(1.1)

where e is the electron charge, m_e is the electron mass, $\gamma \equiv \frac{1}{\sqrt{1-\beta_e^2}}$ the Lorentz factor of the electron with velocity β_e, in units of speed of light c, and B the magnetic field. A power-law distribution of particle energies over a large range (N(E)dE $\propto$ E^{-s} dE, where N(E)dE is the number of electrons per unit volume with energies E to E+dE) will produce a superposition of individual electron spectra and produce emission described by a power-law. The optically thin spectral index α ($S_\nu \propto \nu^\alpha$) is $\frac{-(s-1)}{2}$. At low frequencies the synchrotron emission is self-absorbed and below the turnover frequency ν_m, it has a spectral index of 2.5 for a spatially homogeneous source, regardless of the energy distribution of the electrons. In the case of an isotropic distribution of pitch angles (the angle between the magnetic field and the velocity), the average power emitted by an electron follows:

$$P_{syn} = \frac{4}{3}\sigma_T c\gamma^2\beta_e^2 U_B,$$

(1.2)

where σ_T is the Thompson cross section and $U_B = \frac{B^2}{8\pi}$ is the energy density of the magnetic field. Thus, one can estimate the time scale of cooling via synchrotron radiation:

$$t_{syn} = \frac{E}{\langle P_{syn}\rangle} = \frac{\gamma m_e c^2}{\frac{4}{3}\sigma_T c U_B \gamma^2\beta_e^2} \sim \frac{24.6}{B^2\gamma}\text{yr}.$$

(1.3)

From this it directly follows that cooling is faster at higher energies, and consequently, the spectrum gets steeper with increasing time. The relativistic electrons also lose energy through Inverse Compton scattering, a process that occurs when a low-energy (radio) photon ($h\nu \ll m_e c^2$) is scattered by a relativistic electron. The scattering tends to upshift the photon frequency roughly by γ^2. One can derive the total power emitted through this process:

$$P_{Comp} = \frac{4}{3}\sigma_T c\gamma^2\beta_e^2 U_{ph},$$

(1.4)

where U_{ph} is the radiation energy density. It is immediately obvious that:

$$\frac{P_{syn}}{P_{Comp}} = \frac{U_B}{U_{ph}}.$$

(1.5)

Thus, one can judge which process dominates energy loss through the ratio of the energy density of the magnetic field to that of the radiation field.

---

[2]Electrons can be accelerated to relativistic speeds easier than protons of the larger mass of the latter and thus synchrotron emission is much stronger for electrons than for equal energy protons.

Synchrotron radiation is also characterized by its high linear polarization. At the optically thin part of the spectrum, the polarization percentage (m) in a uniform magnetic field is given by:

$$m(\%) = 100 \times \frac{s + 1}{s + \frac{7}{3}}. \tag{1.6}$$

For a typical value of $s = 2$, one finds that the fractional polarization for optically thin emission can be as high as 69 %.

1.2.2 Relativistic Effects

For a bright knot moving with a speed $v \lesssim c$, it is possible that transverse speeds (to the line of sight) speeds appear to be faster-than-light. The apparent superluminal motion, as predicted by Rees (1966), is an illusion resulting from a simple geometric effect. The discovery of superluminal motion was made in early 1970s by repeated VLBI observations of the quasars 3C 279 and 3C 273 (Whitney et al. 1971; Cohen et al. 1971). The observed transverse velocity of an emitting feature is:

$$\beta_{\mathrm{app}} = \frac{\beta \sin \theta}{1 - \beta \cos \theta}, \tag{1.7}$$

where β_{app} and β are the apparent and the true velocity in units of speed of light c and θ is the angle between the direction of motion and the line of sight.

When a source is approaching us at a speed of v ($\lesssim c$) with an angle θ to the line of sight, the observed frequency ν of a periodic signal is related to the frequency ν' in the co-moving (primed) frame by $\nu = \delta \nu'$, where δ is the relativistic Doppler factor:

$$\delta = \frac{1}{\Gamma(1 - \beta \cos \theta)}, \tag{1.8}$$

with $\Gamma \equiv \frac{1}{\sqrt{1-\beta^2}}$ the bulk Lorentz factor. One can show that the quantity $\frac{S}{\nu^3}$ is a Lorentz invariant (Rybicki & Lightman 1979, chap. 4.9). Therefore, the observed flux density (S) is enhanced (relativistic beaming) as:

$$S = S'\delta^p, \tag{1.9}$$

where S' is the flux density in the co-moving frame, and $p = 3 - \alpha$. The spectral index α appears on the equation because the boosting increases the observed frequency. For a continuous jet, p changes to $2 - \alpha$ (Lind & Blandford 1985). Equation 1.9 allows us to derive a flux density ratio (R) between the jet and counter jet for an assumed intrinsically symmetric jet, as:

$$R = (\frac{1 + \beta \cos \theta}{1 - \beta \cos \theta})^{2-\alpha}. \tag{1.10}$$

Obviously, the jet is significantly brighter than the counter jet even for a mildly relativistic jet. This explains why we almost always see one-sided jets.

1.2.3 Brightness Temperature

The radiation from a black body in thermodynamic equilibrium is given by Planck's law:

$$I_\nu = \frac{2h\nu^3}{c^2} \frac{1}{\exp^{\frac{h\nu}{kT}} - 1}, \tag{1.11}$$

where I_ν is the brightness in W.m^{-2}.Hz^{-1}.sr^{-1},
h is the Planck constant (6.63×10^{-34} J sec),
ν is the frequency in Hz,
c is the speed of light in vacuum (2.998×10^8 m sec^{-1}),
k is the Boltzmann constant (1.38×10^{-23} J K^{-1}),
T is the temperature in Kelvin.
In the radio regime, where $h\nu \ll kT$, Plank's law reduces to the Rayleigh-Jeans approximation:

$$I_\nu = \frac{2\nu^2 kT}{c^2} \tag{1.12}$$

The brightness of a black body depends only on its temperature and the observing frequency. Hence, for an observed brightness one can define an equivalent temperature that a black body is needed to have in order to emit the observed intensity at a given frequency:

$$T_{\rm b} = \frac{I_\nu c^2}{2\nu^2 k}. \tag{1.13}$$

The brightness temperature of a VLBI source component with Gaussian brightness distribution is given by:

$$T_{\rm b} = 1.22 \times 10^{12} \frac{S}{\nu^2 \theta^2} \, \text{K}, \tag{1.14}$$

where S is the flux density in Jy, ν the frequency in GHz, and θ (FWHM) in mas, respectively.

The brightness temperature is a good diagnostic for the emission process at work in compact radio sources. VLBI measurements of flux densities and angular sizes for extragalactic radio sources have consistently yielded peak brightness temperatures in the range of $10^{11...13}$ K, which is definitively produced by non-thermal processes since $kT > m_{\rm e}c^2$.

Theoretically, there are strong upper limits on the brightness temperature for an incoherent synchrotron source. They are the inverse Compton limit, which was first

pointed out by Kellermann & Pauliny-Toth (1969), and a tighter limit based on equipartition arguments (Readhead 1994). The inverse Compton limit is based on the argument that at brightness temperatures $T_b > 10^{12}$ K, the energy loss of electrons will be dominated by inverse Compton scattering effects (Equation 1.5). This process will cool the system rapidly and therefore bring the brightness temperature below this limit. Readhead (1994) derived an even tighter limit on the maximum brightness temperature. According to him, sources radiate below 5×10^{10}–10^{11} K when energy densities of the relativistic particles and the magnetic fields are in equipartition. Measured brightness temperature in excess of these limits can be explained by Doppler boosting.

There are also observational limitations to the maximum brightness temperature that can be measured interferometrically. According to Equation 1.14, one finds that the measured brightness temperature depends only on the maximum baseline length (D), for a given flux density, since the resolution is proportional to $\frac{\lambda}{D}$. Therefore, the maximum brightness temperature that can be probed from earth based interferometer is limited by the diameter of the Earth and is coincidentally $\sim 10^{12}$ K (Kellermann & Moran 2001). In other words, ground-based baselines can not resolve a source with brightness temperature $\gg 10^{12}$ K.

2 Sagittarius A* as an AGN

Located at the dynamical center of the Galaxy, the compact radio, NIR, and X-ray source Sagittarius A* (hereafter Sgr A*[3]) is believed to be the emission counterpart of a $\sim 4 \times 10^6 M_\odot$ black hole (see section 2.2.1). As mentioned in Chapter 1, the discovery of Balick & Brown (1974) provided strong support for the black hole scenario and it was a detection using the "right" interferometer after several attempts (see e.g., Goss et al. 2003, for a detailed recounting). Its relative proximity renders it able to be investigated in great detail.

In terms of Eddington luminosity, Sgr A* is extremely dim. Its bolometric luminosity L is $\sim 10^{36}$ erg s^{-1}, which is 8 orders of magnitude lower than its Eddington luminosity ($L_{\rm Edd} \sim 5.2 \times 10^{44}$ erg s^{-1}). The ultra-low luminosity of Sgr A* had raised some doubts about the accretion - black hole paradigm acting at the GC. However, in spite of this apparent diversity, there is now strong evidence that Sgr A* is associated with a SMBH (see next section). Therefore, Sgr A* and AGNs do share a common energy production mechanism, i.e., the accretion of matter onto a SMBH at their centers. Moreover, Sgr A* fits well into the so-called "fundamental plane" (a relationship between radio and X-ray luminosities and mass), indicating a similar physical process at work in accreting black holes of all masses (Fender et al. 2007, and references therein). In this context, Sgr A* serves as a link between stellar mass and $10^9 M_\odot$ black holes.

2.1 The Uniqueness of Sgr A*

Sgr A* stands out from its surrounding radio sources and is unique in several ways. Its compactness (point-like) and non-thermal spectrum are reminiscent of the compact nuclear radio sources associated with typical AGNs. The proximity of Sgr A* (8 kpc), however, offers us a unique opportunity for testing the SMBH paradigm, which is unaccessible in the case of AGNs. For example, the next closest galactic nucleus

---

[3] A few names (e.g., "GCCRS" (Reynolds & McKee 1980), "Sgr-A" (Brown et al. 1978), "Sgr A" Brown & Lo (1982), "Sgr A (cn)" (Backer & Sramek 1982)) were assigned to the compact radio source but only "Sgr A*" (Brown 1982) survived.

(M 31*) is $\sim$ 100 times farther away from us than Sgr A*. As shown in Table 2.1, apparent angular sizes of several black hole event horizons are compared for several (notable) sources. In terms of apparent size, Sgr A* is the largest black hole candidate. Within the next decade, imaging of the event horizon of Sgr A* would even be possible (Doeleman et al. 2009a). Thus, the study of physics near the event horizon will finally provide important insight into other black hole accreting systems.

Table 2.1: Apparent angular size of the event horizon of some black hole candidates

Source	Distance	Mass	θ_{H}	Reference
	[$\times 10^6$ pc]	[$\times 10^6 M_\odot$]	[μas]	
Sgr A*	8.0×10^{-3}	4.0	10	1
M 87	17.9	6.4×10^3	7	2
M 31	0.77	56.2	1.4	3
NGC 4258	7.2	36	0.1	4
Stellar mass	1×10^{-6}	1	0.02	assumed

References: (1) section 2.2.1; (2) Both mass and distance from Gebhardt & Thomas (2009); Note the suddenly double of the mass. (3) Salow & Statler (2004, and references therein); (4) mass from Miyoshi et al. (1995) and distance from Herrnstein et al. (1999). Adapted and updated from Miyoshi & Kameno (2002).

Recently, there has been accumulation of evidence that Sgr A* is the emission counterpart of a $\sim 4 \times 10^6 M_\odot$ black hole at the GC. Specifically, the evidences come mainly from the study of stellar dynamics in the vicinity of Sgr A* and proper motion of Sgr A* (section 2.2.1). Recent improvement on the size determination of Sgr A* with VLBI allows us to set stringent constrains on the mass density with the help of proper motion studies (Bower et al. 2004; Shen et al. 2005; Doeleman et al. 2008). The implied mass density of $9.3 \times 10^{22} M_\odot \mathrm{pc}^{-3}$ (Doeleman et al. 2008) is just 2 orders of magnitude lower than that of a $4 \times 10^6 M_\odot$ black hole within its Schwarzschild radius.

The uniqueness of Sgr A* also lies in the typical timescales of order of minutes to hours for the orbital motion near the last stable orbit of the $4 \times 10^6 M_\odot$ black hole. For instance, rapid variability is expected to occur at the last stable orbit with a period of $\sim$ 30 minutes (for a non-rotating black hole). In the case of a maximally rotating Kerr black hole, the time scales are within $\sim$ 4 (prograde) to 54 (retrograde) minutes depending on its spin (Melia et al. 2001, scaled with $4 \times 10^6 M_\odot$). Compared to the time scale associated with stellar mass black holes and luminous AGNs, these are easily accessible to us. Therefore, Sgr A* is an ideal "poster child" for black hole studies with unique advantages both spatially and temporally.

2.2 Observational Facts about Sgr A*

2.2.1 Mass

The most robust evidence for the existence of a SMBH at the GC comes from the highly concentrated gravitational mass determined through investigations of gas and stellar dynamics in the near infrared (NIR). Evidence has been accumulated over the past three decades from observations of radial velocities of gas and stars (Genzel & Townes 1987). However, reliable determination of the mass content and concentration relies on the measurement of the full velocity field with test particles (stars, since gas is subject to other non-gravitational forces). Here we list some milestones towards this goal.

- Proper motion studies (Eckart & Genzel 1996; Ghez et al. 1998)
  Before proper motion measurements were available, there were only radial velocity measurements of gas and stars. The proper motion measurements relaxed the assumption that stellar obits are largely circularly and isotropically distributed (see Figure 2.1 (b)). The dependence of velocity dispersion on the distance from Sgr A* is in good agreement with that obtained from radial velocities, and therefore solidifies the evidence for the existence of a massive point mass.

- Accelerations (Ghez et al. 2000; Eckart et al. 2002)
  Acceleration measurements of stars permit the determination of the location of the dark mass.

- Keplerian orbits (Schödel et al. 2002; Ghez et al. 2005)
  Keplearian orbits or even full orbital solutions allow then to constrain the position and mass of the black hole.

The mass density distribution (Figure 2.1 (a)), as inferred from velocity dispersion measurements, excludes explanations other than that of a SMBH. As of 2009, as many as 26 stellar obits in the GC have been obtained (Eckart & Genzel 1996, 1997; Eckart et al. 2002; Schödel et al. 2002; Eisenhauer et al. 2003; Ghez et al. 2000, 2005, 2008; Gillessen et al. 2009). All the orbits can be well fitted by a single point mass and focal position (as illustrated in Figure 2.1 (b)). Registration of the radio reference frame and NIR frame (Reid et al. 2007, and references therein) allows comparison of the position of the central point mass inferred from orbit fits to the radio source Sgr A*. They are found to coincide within roughly 20 AU (2 mas). Measurement of the radial velocity

of the young stars (Ghez et al. 2003b) also allows the geometric determination of the distance to the Galactic Center (R_0) from stellar orbits (Eisenhauer et al. 2003, 2005).
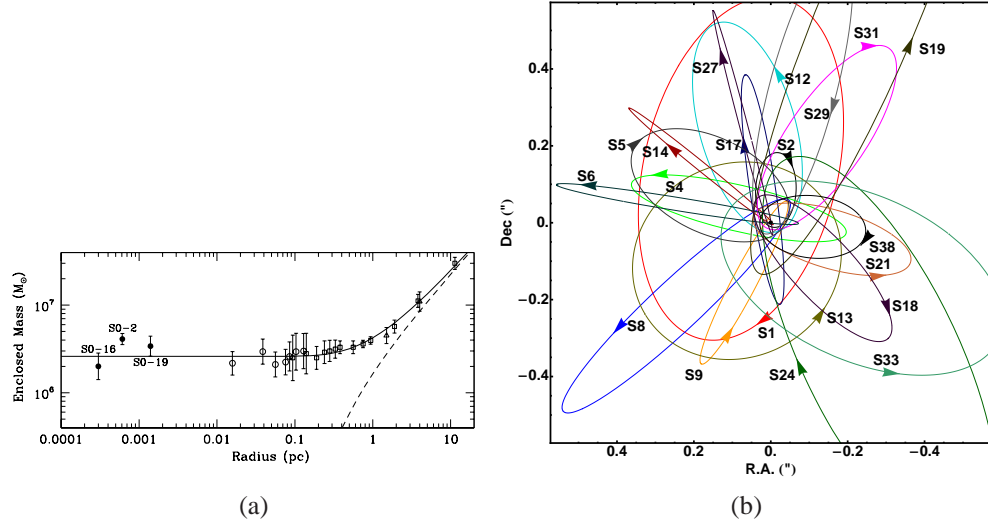
Figure 2.1: (a) The enclosed masses from individual stars orbital motion (filled symbols) and those determined based on velocity dispersion (open symbols) in the nuclear cluster in the Galactic Center. The solid line represents the best fit black hole plus luminous cluster model, with black hole mass $M_\bullet = (3.6 \pm 0.4) \times 10^6 M_\odot$. The dashed line indicates the enclosed mass due to a star cluster alone (from Ghez et al. 2003a). (b): A plot of the stellar orbits of the stars in the central arcsecond of the GC. The coordinate system was chosen so that Sgr A* is at rest. The arrows indicate the direction of motion. Taken from Gillessen et al. (2009).

Complementary to stellar dynamics studies, proper motion studies of Sgr A* via VLBI phase referencing can provide an independent constrain on the mass of Sgr A* itself. If the compact radio source Sgr A* is indeed the gravitational source, it should be nearly at rest at the dynamical center of the Galaxy, and any peculiar motion can provide a mass estimate (Backer & Sramek 1982). The apparent proper motion of Sgr A* observed with the VLA (Backer & Sramek 1999) and VLBA (Reid et al. 1999; Reid & Brunthaler 2004) was shown to be consistent with that expected from the known effects of the Sun's motion relative to Sgr A*, namely the peculiar motion relative to the local standard of rest and secular parallax of Sgr A* due to the rotation of the Sun around the GC. After removing these effects, Reid & Brunthaler (2004) found that the residual proper motion of Sgr A* perpendicular to the Galactic plane is as small as $-0.4 \pm 0.9 \, \mathrm{km \, s^{-1}}$ (Figure 2.2), which leads to the conclusion that Sgr A* contains at least a mass of $\sim 4 \times 10^5 M_\odot$.
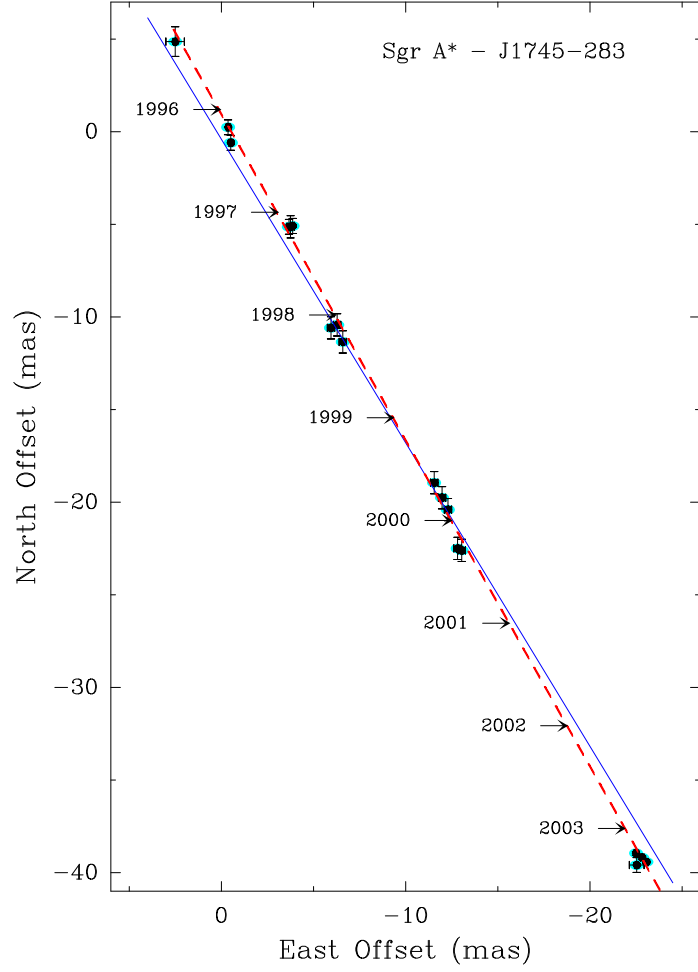
Figure 2.2: Sgr A* position residuals on the sky plane with respect to the background source, J1745-283. Shown as a dashed line is a weighted least squares fit proper motion and the solid line gives the orientation of the Galactic plane. The clear deviation of the motion from the Galactic plane can be well explained by the known component of the solar motion perpendicular to the Galactic plane. After removing the known Z-component of the solar motion, the out-of-plane component of the peculiar motion of Sgr A* is as small as $-0.4 \pm 0.9 \, \mathrm{km \, s^{-1}}$ (from Reid & Brunthaler 2004).

Recent revision of the central black hole's mass and distance has yielded consistent values: $M_\bullet = (4.31 \pm 0.06|_{\text{stat}} \pm 0.36|_{R_0}) \times 10^6 M_\odot$ and $R_0 = 8.33 \pm 0.35$ kpc (Gillessen et al. 2009), $M_\bullet = (4.5 \pm 0.4) \times 10^6 M_\odot$ and $R_0 = 8.4 \pm 0.4$ kpc (Ghez et al. 2008), and $R_0 = 8.4 \pm 0.6$ kpc (Reid et al. 2009). Throughout this thesis we adopt for the GC black hole a total mass of $4 \times 10^6 M_\odot$ and a distance of 8 kpc to us. The Schwarzschild radius ($R_{\text{Sch}} = \frac{2GM_\bullet}{c^2}$) is then 1.2×10^{10} m, or 0.1 AU, or $10\,\mu$as, and 1 light-minute is $1.5\,R_{\text{Sch}}$.

2.2.2 Scattering Effects

Radio waves from Sgr A* are heavily scattered by the intervening ISM. Interstellar scattering arises from fluctuations of the electron density. It causes many observable effects such as the angular broadening of a source, temporal broadening of a pulse signal, flux density fluctuations (scintillation, both diffractive and refractive), and image wander (Rickett 1990). Electron density fluctuations are normally thought to occur over a wide range of scales. Its three dimensional spatial power spectrum P_{3N} often takes the form of a power-law with cutoffs (e.g., Armstrong et al. 1995):

$$P_{3N}(q) \approx C_N^2 q^{-\beta}, \quad L_0^{-1} < q < \ell^{-1} \tag{2.1}$$

where q is the spatial wavenumber and the constant C_N^2 is a measure of the electron density fluctuations. L_0 is the "outer" scale on which the fluctuations occur, and ℓ the "inner" scale on which the fluctuations dissipate. If $\beta < 4$, the spectrum is referred to as shallow and diffractive scattering effects would dominate. If $\beta > 4$, it's a steep spectrum with refractive effects dominant. $\beta = \frac{11}{3}$ corresponds to a Kolmogorov spectrum (Desai & Fey 2001, and references therein). Along many lines of sight, the spectrum index of the power spectrum were found to be close to the Kolmogorov value (Wilkinson et al. 1994; Molnar et al. 1995; J. Franco & A. Carraminana 1999; Lazio & Fey 2001). For a few lines of sight the spectral index is found to be approaching or large than 4 (Moran et al. 1990; Clegg et al. 1993; Desai & Fey 2001).

2.2.2.1 Angular Broadening

Angular broadening, as its name implies, leads to an enlarged angular size of a source. At a given wavelength, the intrinsic size θ_{int} can be obtained via the deconvolution operation:

$$\theta_{\text{int}} = \sqrt{\theta_{\text{meas}}^2 - \theta_{\text{scat}}^2} \tag{2.2}$$

where θ_{meas} and θ_{scat} are the measured apparent size and the scattering disk size, respectively (e.g., Narayan & Hubbard 1988). The wavelength dependence of the scattering

size for a shallow wavenumber spectrum, is: $\theta_{\text{scat}} \propto \lambda^{\frac{\beta}{\beta-2}}$. When the VLBI baseline length becomes comparable to the inner scale of the density fluctuations, the scattering law changes and has the following form: $\theta_{\text{scat}} \propto \lambda^2$ (Lazio 2004).

Soon after the discovery of Sgr A*, it was realized that the observed change of size with wavelength is due to interstellar scattering effects (Davies et al. 1976). Furthermore, Lo et al. (1985, 1993) found that the scatter-broadened image of Sgr A* can be modeled by an elliptical Gaussian with an axes ratio of ~ 0.5 at 8 GHz, indicating an anisotropic scattering effect. The existence of anisotropic scattering towards the GC region was further established when non-circular scattering disks of OH masers within 25′ of Sgr A* were observed. It is, therefore, evident that the electron density inhomogeneities have a preferred direction. Such anisotropy in electron density fluctuations could result, e.g., from an ordered magnetic field (Frail et al. 1994; van Langevelde et al. 1992).

Radio images of several other sources also display the effects of anisotropic scattering. The brightness distribution is close to an elliptical Gaussian with axes ratio varying from source to source, e.g., 2013+370 (Spangler & Cordes 1988), Cygnus X-3 (Wilkinson et al. 1994; Molnar et al. 1995), NGC 6334B (Trotter et al. 1998). Moreover, axes ratio and orientation of the scattering disk have been found to exhibit λ-dependence toward a few more lines-of-sight, e.g., Cygnus X-3 (Wilkinson et al. 1994) and NGC 6334B (Trotter et al. 1998). This has been attributed to an increasingly ordered magnetic field on smaller scales (cf. Figure 13 in Trotter et al. 1998). Such scale-dependent anisotropy interpretation could in principle enable one to estimate the outer scale of the density fluctuations. An alternative interpretation for the change of orientation and ellipticity with wavelength may be that the intrinsic structure begins to shine through at higher frequencies. For Sgr A*, no indication of wavelength dependence of the orientation was found in the past (for a possible deviation from this, see section 4.2.3 of Chapter 4).

The knowledge of the exact nature and location of the scattering material, however, is still poor. It has been argued that the scattering screen which causes angular broadening of Sgr A* occurs in the ionized surface of molecular clouds lying in the central 100 parsecs of the Galaxy (Yusef-Zadeh et al. 1994). The location of the scattering region close to GC was supported by later observations of Lazio & Cordes (1998), who constrained the scattering screen - GC distance to 150 parsecs.

The apparent angular sizes along both the major and minor axis for the elliptical structure of Sgr A* show a wavelength dependence generally consistent with a λ^2 dependence at centimeter wavelengths. Deviations from a λ^2 scaling at shorter wavelengths (millimeter) are commonly interpreted as an effect of intrinsic structure becom-
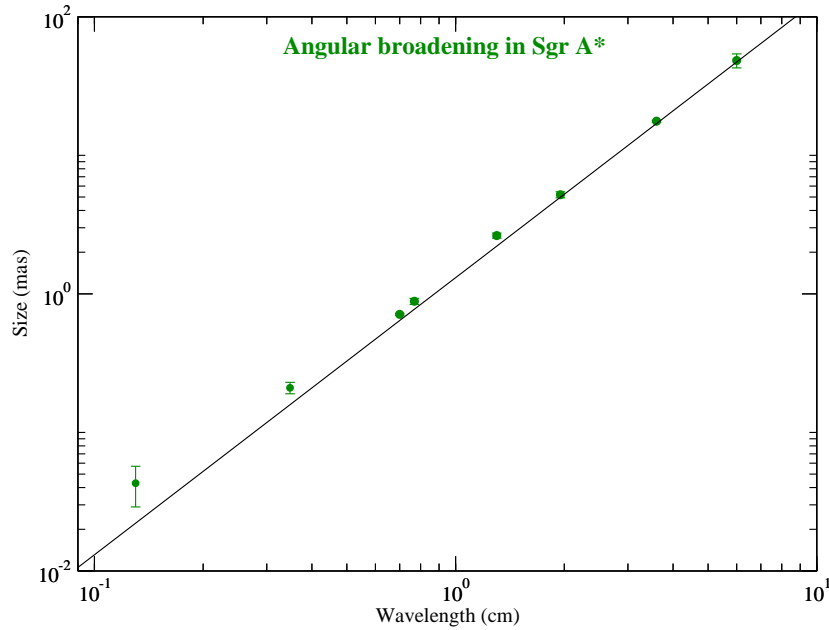
Figure 2.3: Apparent angular size of Sgr A*along the major axis as a function of wavelength. The data are from Bower et al. (2004); Shen et al. (2005); Doeleman et al. (2008). The solid line delineates a λ^2 scatter law (Bower et al. 2006), which is derived from longer wavelengths (17.4–23.8 cm) measurements.

ing dominant (Marcaide et al. 1992; Krichbaum et al. 1993; Yusef-Zadeh et al. 1994; Lo et al. 1998; Krichbaum et al. 1998b; Doeleman et al. 2001, and references therein). Figure 2.3 shows the angular broadening effect in Sgr A*. As mentioned above, the intrinsic size of Sgr A* is obtained by subtraction of the scattering size from the scattering broadened size in quadrature (equation 2.2). Therefore, the scattering law along the line of sight toward the GC is crucial for determining the intrinsic structure (size and shape).

2.2.2.2 Refractive Interstellar Scintillation

Refractive interstellar scattering is associated with electron density fluctuations on sub-parsec scales. These fluctuations act as lenses that focus or defocus the source image, are produced on scales much larger than those responsible for diffractive effects, and cause slow fluctuations of intensity (scintillation). The refractive scattering timescale is determined by the time the sub-parsec scale density fluctuation takes to move across our line of sight. Typically, the timescale is of the order of days for pulsars and from months to years for extragalactic sources (e.g., Lazio & Fey 2001). In contrast, diffrac-

tive scintillation (in analogy to twinkling of stars) is more rapid on timescales of minutes to hours. For a shallow spectrum ($\beta < 4$), refractive effects would in general be suppressed by diffractive effects caused by even smaller density fluctuations (Romani et al. 1986).

Long-term flux variations for Sgr A* seen at low frequencies (< 5 GHz) have been explained in terms of refractive interstellar scattering (Zhao et al. 1989). Nonetheless, the observed modulation index seems to be under-predicted by a thin screen model based on the Kolmogorov spectrum. Models in which the scattering medium extends out can account for the high modulation index and are recently investigated in the context of Sgr A* (Macquart & Bower 2006). Later monitoring data, more densely sampled, found, however, that the variations are more pronounced at higher frequencies, indicating that the intrinsic variations become important (Zhao et al. 1992; Falcke 1999). In addition, the inferred variability timescale does not follow an expected λ^2 dependence from scattering theory (Falcke 1999; Melia & Falcke 2001).

At 0.8 and 1.3 mm, Gwinn et al. (1991) failed to detect significant flux variations on time scales from 0.1 s to one day. They argued that refractive scintillation for Sgr A* is quenched at these wavelengths as the source angular size presumably exceeds the scattering size. In this way, a lower limit to the source size ($\sim 10\,\mu$as) can also be obtained.

Although variability at high frequencies is generally thought to be source intrinsic as discussed below, the nature of radio (centimeter) variability of Sgr A* has been debated. Since radio waves from Sgr A* are heavily scattered, refractive scintillation should contribute to flux variations unless it is quenched. After the claim of quasi-periodic modulations, an intrinsic cause for the variations is favored (Falcke 1999; Zhao et al. 2001). Therefore, both extrinsic and intrinsic variability should be responsible for the modulations at centimeter wavelengths. The difficulty lies in determining the contribution of scattering effects and separating them from the intrinsic variations of the source. Macquart & Bower (2006) collated multi-wavelength (0.7–20 cm) monitoring data available at that time. Their analysis indicates Sgr A* shows no quasi-periodic oscillations on any timescale between 1 week and 200 days. Additionally, extended-medium models account well for the broad characteristics of the variability on timescales larger than a few days and a 10 % of the variability on timescales of a few days at 0.7–3 cm seems to be source intrinsic.

2.2.2.3 Position Wander

In addition to long-term flux density variations, interstellar scattering causes refractive fluctuations of the apparent position of a radio source. The magnitude of this effect is sensitive to the power law index of β. In the case of a "steep" spectrum ($\beta > 4$), models predict strong refractive position shifts, which are far greater than the scattering disk θ_{scat} (Rickett 1990).

Scattering-induced position wander of Sgr A* seems to be much smaller than θ_{scat} and it should occur on timescales larger than 10^3 hours, if at all (Reid et al. 2008). Proper motion studies of Sgr A* provide stringent limits on the long-term position wander. These observations indicate refractive effects to be negligible (Backer & Sramek 1982, 1999; Reid et al. 1999). Small displacement of the image centroids at different frequencies provide further support for this argument (Backer & Sramek 1982, 1999). Moreover, Gwinn et al. (1988) studied refractive position wander for H_2O masers in Sgr B2(N). Their VLBI observations set an upper limit of $18\,\mu$as for the maser spots wander, and thus ruled out "steep" density spectrum towards that line of sight.

The angular broadening effect, refractive scintillation (Macquart & Bower 2006) and lack of image wander of Sgr A* are consistent with a picture of a "shallow" density spectrum ($\beta < 4$) for the scattering medium towards the GC.

2.2.3 Intrinsic Structure

It is clear from the above discussion that attempts to measure the source structure at centimeter wavelength suffer from the angular broadening effect, which dominates the resulting images. The λ^2 dependence of the scattering effect has been driving VLBI observations of Sgr A* to shorter and shorter wavelengths, where the image blurring vanishes. The last few years have seen great progress in the size determination of Sgr A*. Millimeter-VLBI observations of Sgr A* at 43 and 86 GHz suggest a break in the λ^2 dependence of the scattering law. This implies that the intrinsic source structure becomes visible and begins to dominate over the scatter broadening effect above $\nu \simeq$ 43 GHz (Krichbaum et al. 1998c; Lo et al. 1998; Doeleman et al. 2001; Bower et al. 2004; Shen et al. 2005; Bower et al. 2006; Krichbaum et al. 2006). The recent detection of Sgr A* with VLBI at 1.3 mm at a fringe spacing of $\sim 60\,\mu$as has pushed the limit of the size of the compact VLBI emission down to $\sim 4\,R_{Sch}$ ($\sim 43\,\mu$as). This is smaller than the theoretically expected size of the emission region around a $4 \times 10^6\,M_\odot$ SMBH, assuming it is not rotating (Doeleman et al. 2008). At present it is unclear whether the

compact emission seen with 1.3 mm-VLBI is related to the (relativistically aberrated) silhouette around the BH, a hot spot or inhomogeneity in the accretion disk, or to something else (Broderick & Loeb 2006; Broderick et al. 2009; Huang et al. 2007).

At the same time, as we are probing the emission distribution in the vicinity of the SMBH with high frequency VLBI, Gaussian parametrization of the source structure may ultimately need modifications due to general relativistic effects near the black hole (Broderick & Loeb 2006). Comparison of emission models with visibilities and closure quantities (closure phase and closure amplitude) from VLBI observations will play a key role in discerning between different theoretical models (Markoff et al. 2007; Doeleman et al. 2009b; Huang et al. 2009b; Dexter et al. 2009; Fish et al. 2009; Broderick et al. 2009)

2.2.4 Spectrum

It has been claimed that the time-averaged radio spectrum ($S_\nu \propto \nu^\alpha$) of Sgr A* roughly follows a $\nu^{\frac{1}{3}}$ law (Duschl & Lesch 1994). Later studies (e.g., Serabyn et al. 1997), in particular, simultaneous observations (Falcke et al. 1998; An et al. 2005, and references therein) found a few additional features. There probably exist two breaks in the inverted radio spectrum (Melia & Falcke 2001). The first is found to be around $10\,\mathrm{GHz}$ above which the spectrum becomes slightly inverted. This may become negligible for time-averaged spectrum ($\alpha \sim 0.3$ from centimeter to millimeter wavelengths Zhao et al. 2001). The second break, which is observed in the mm/sub-mm band marks the advent of the so-called "mm/sub-mm bump". Notice that the simultaneous spectrum of An et al. (2005) might have missed the "bump" peak due to the frequency coverage in their observations. At very long wavelengths ($< 1\,\mathrm{GHz}$), there might be a turnover at possibly variable frequencies (Davies et al. 1976; An et al. 2005), as revealed thanks to the recent detection of Sgr A* at ~ 90 cm (Nord et al. 2004).

Figure 2.4 shows the spectrum of Sgr A* between ~ 1–$670\,\mathrm{GHz}$. In the mm/sub-mm regime the spectrum is characterized by a submm-excess. The existence of the "bump" has been uncertain since flux densities measured with single dishes/connected interferometers and different beam sizes may suffer from confusion by other sources (e.g., the diffuse free-free emission, transient sources, and dust emission Falcke et al. 1998; Bower et al. 2005b; Krichbaum et al. 2006). However an extrinsic cause of the "bump" does not seem plausible since the "bump" is also visible with VLBI measurements (Chapter 4).

However, the mm/sub-mm excess is still poorly understood. Phenomenally speaking, neither the frequency at which the excess begins to be significant nor the fre-
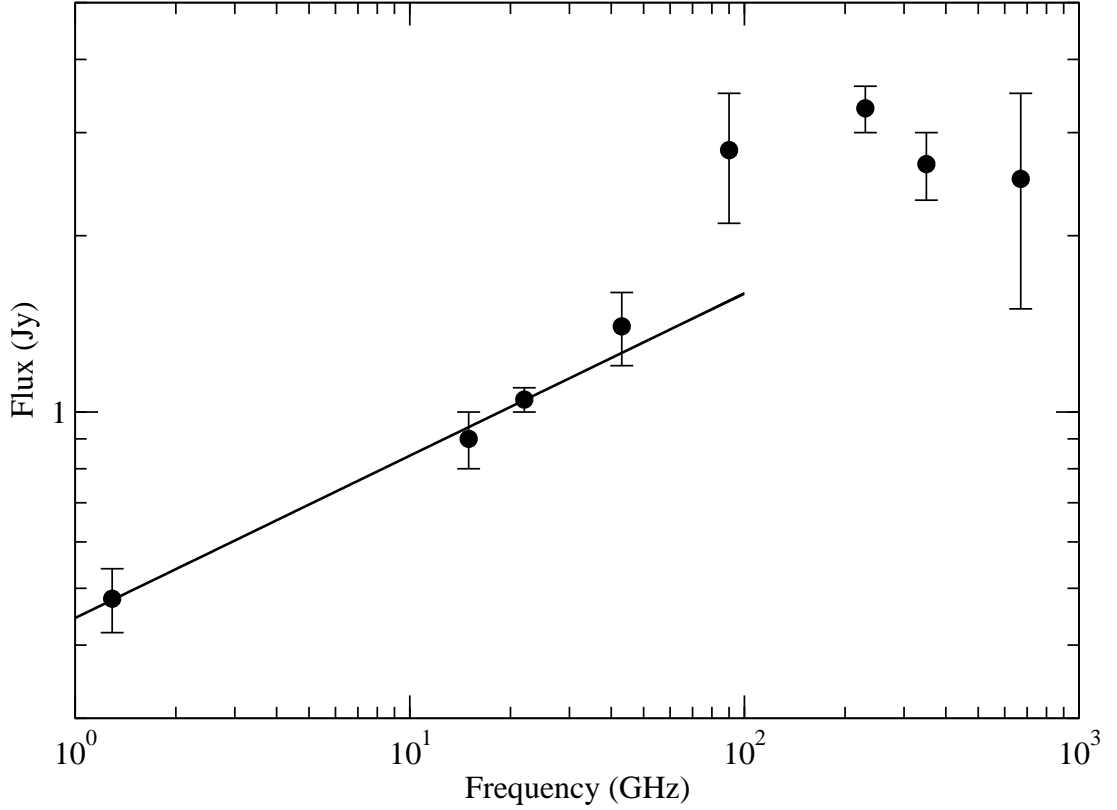
Figure 2.4: Spectrum of Sgr A* between 1 and 670 GHz. Shown with filled circles is a quasi-simultaneous spectrum estimated from data obtained in the time period close to April 1, 2007 from a multi-wavelength campaign (Yusef-Zadeh et al. 2009). The error bars on the data indicate the variability of Sgr A* during the observations. A power law fit ($S_\nu \propto \nu^\alpha$) to the radio data up to 43 GHz is shown with the solid line ($\alpha \sim 0.3$). Above 43 GHz a flux density excess can be observed.

quency of the peak emission were very clear (Falcke et al. 1998; Zhao et al. 2003). Based on SMA observations, Marrone et al. (2006a) concluded that the average spectrum peaks between 230 and 690 GHz. Yusef-Zadeh et al. (2006b) using simultaneous multi-frequency data found the quiescent spectrum to peak at 350 GHz . The quasi-simultaneous spectrum in Figure 2.4 shows a peak at 230 GHz. Unfortunately, the observations at 350 GHz were performed on April 6, which are not simultaneous with observations for the 2 adjacent frequencies at 230 and 670 GHz (on April 1).

Radio observations provided strong constrains to the modeling of matter accretion and radiation near the black hole. In jet models (Falcke & Markoff 2000), the flat radio spectrum is a consequence of superposition of self-absorbed synchrotron emission from the jet and the "bump" may result from the compact "nozzle" component, the

acceleration zone of the jet. While in the view of the RIAF, this mm/submillimeter bump is primarily produced by thermal electrons in the inner parts of the accretion disk (Yuan et al. 2003). In either case, the "bump" arises from the vicinity of the black hole.

Besides radio photons, the ISM is also transparent for IR and high energy (above 2 keV) photons towards the GC. The spectrum plunges after the "bump" due to the modest luminosities at these high energies. Although various attempts were made to detect Sgr A* at frequencies other than radio (e.g., Eckart et al. 1992), only recently have breakthroughs been made in NIR (Genzel et al. 2003; Ghez et al. 2004) and X-rays (Baganoff et al. 2001; Goldwurm et al. 2003; Porquet et al. 2003). These discoveries owe a great deal to the advance in observation techniques and instruments (i.e., adaptive optics in the NIR (Genzel 2007) and the advent of high resolution and sensitivity Chandra and XMM-Newton X-ray telescopes). It is particularly interesting that in both NIR and X-ray bands, Sgr A* is the source of strong flares (see also section 2.2.5). For the variable NIR emission, variability in the infrared spectrum, for which spectral index correlates with flux density (the brighter, the harder), has been reported (Gillessen et al. 2006). However, this was not confirmed by Keck observations. The latter observations showed a constant spectral index of $\alpha = -0.6 \pm 0.2$ (Hornstein et al. 2007).

The X-ray emission shows two distinct components. The quiescent emission is soft (photon index $\Gamma \sim 2.7$) and extended ($\sim 1''$) (Baganoff et al. 2003). But for the unresolved flare emission, no consensus has been reached as for the spectrum. It is still not clear whether all flares have the same spectrum. The flare detected by *Chandra* showed a hard ($\Gamma = 1.3^{+0.5}_{-0.6}$) spectrum (Baganoff et al. 2001), while for the two strongest X-ray flares ever observed, the spectra are soft ($\Gamma = 2.5 \pm 0.3$ and 2.3 ± 0.3) (Porquet et al. 2003, 2008).

Sgr A* may also be a γ-ray source. INTEGRAL observations (20–600 keV) revealed a faint and persistent emission from the very center of the Milky Way, which coincides with Sgr A* within $1'$ (Goldwurm 2007, and references therein). Emission above 100 MeV from the GC region have also been reported by the EGRET (Mayer-Hasselwander et al. 1998). However, poor resolution and lack of detected variability make the association of detected sources at the GC with the central black hole not definitive. With significantly improved performance, the Fermi Gamma-ray Space Telescope will definitely provide more (compared to EGRET) information to unfold the mystery.

In the very high energy (VHE) regime, TeV γ-ray emission has been detected from the direction of Sgr A* by several ground-based instruments (Aharonian et al. 2006b,

and references therein). Due to the poor resolution of γ-ray telescopes, a few possible sites and processes of γ-ray production have been discussed in the literature. Sgr A* seems to be the most likely site for the detected TeV γ-ray emission (see Aharonian et al. (2009) for reference) and recently Sgr A East appears to be excluded (The HESS Collaboration 2009). In this context, Aharonian & Neronov (2005) discussed possible emission mechanisms which can give rise to TeV γ-ray emission in the immediate vicinity of the SMBH, with both hadronic and leptonic origins.

Again, if the VHE radiation indeed comes from a region close to the event horizon of the SMBH, temporal intensity variations along with flares would be expected. Contrary to expectations, no variability on any available time scales was found so far for the Galactic center γ-ray source (Aharonian et al. 2008, 2009), unlike M 87 (Aharonian et al. 2006a). These findings disfavor same mechanisms and emission regions for TeV emission (if associated with Sgr A*) as variable X-ray and IR emission from Sgr A*. Nevertheless, these observations do set upper limits on the high energy emission of Sgr A*.

2.2.5 Flux Density Variability

Sgr A* is known to vary at all wavelengths. The presence of variability in the radio flux density was suggested already with the discovery of Sgr A* was made (Balick & Brown 1974). The time scales in the radio are found to vary from weeks to years (Brown & Lo 1982; Zhao et al. 1989, 1992; Herrnstein et al. 2004). Long timescale variability at the longer centimeter wavelengths is generally ascribed to interstellar scintillation (section 2.2.2). However, there also exist long timescale flux variations at short, centimeter/millimeter, wavelengths where interstellar effects are negligible. A possible bimodal distribution of flux density (i.e., low state vs. high state) at these frequencies may exist and it may reflect two distinct states of accretion onto the SMBH (Herrnstein et al. 2004; Li et al. 2009, and references therein).

Short timescale variations (Intra-day Variability) are source intrinsic and are of special interest because they allow us to probe regions in the vicinity of the central black hole. At 1.3 and 0.7 cm, Yusef-Zadeh et al. (2006a) reported a low level (4.5 and 7 %) of flare activity on a timescale of few hours. Variability on hourly time scales was also reported by several authors at various frequencies in the mm/sub-mm regime (Tsuboi et al. 1999; Miyazaki et al. 2004; Mauerhan et al. 2005; Eckart et al. 2006b; Li et al. 2009). Generally, it appears that the variability amplitude increases with frequency during the "outbursts".

Soon after the first report of flares from Sgr A* in the X-rays (Baganoff et al. 2001),

flares were detected also in the near-infrared (NIR) wavelengths (Genzel et al. 2003). Flaring activity with duration of ~ 1 hour duration has been intensively studied. Of particular interest are subflares on shorter time scales modulating broader flares, consistent with quasi-periodicity of ~ 20 minutes (e.g., Genzel et al. 2003; Eckart et al. 2006a). However, it is argued that although the peaks in the light curves have often been interpreted as discrete flares, the NIR emission varies continuously and the variations are described well as red noise (Do et al. 2009). Possibly, these quasi-periodic oscillations are transient events (Meyer et al. 2008). Furthermore, polarimetric studies showed that the variable NIR emission is highly polarized, indicating the non-thermal origin of the NIR emission (Eckart et al. 2006a, 2008b). Variations in both the degree and position angle of the polarization were also observed (Meyer et al. 2006b; Trippe et al. 2007; Nishiyama et al. 2009).

X-ray flares observed by *Chandra* and *XMM* (Porquet et al. 2008, and references therein) showed a variety of intensities with the brightest one ever observed reaching 160 times the quiescent level (Porquet et al. 2003). The short rise/fall time of these flares (several hundred seconds) implies that they arise from within a few $R_{\rm Sch}$ from the SMBH. The simultaneity of NIR and X-ray flare indicates that they come from the same inner region of the SMBH (Eckart et al. 2004; Yusef-Zadeh et al. 2006b; Dodds-Eden et al. 2009). Observations of NIR and X-ray flares have revealed a few general features:

- X-ray flares are rare compared to NIR ones (Baganoff et al. 2003; Eckart et al. 2006b).

- Every X-ray flare seems to have a counterpart in NIR but not vice-versa (e.g., Hornstein et al. 2007).

There is also increasing evidence that the NIR/X-ray flares are linked to variations in radio through submillimeter wavelengths (Eckart et al. 2008c, 2006b; Marrone et al. 2008; Yusef-Zadeh et al. 2008, 2009). Following the first successful simultaneous detection of flare emission in NIR and X-rays (Eckart et al. 2004), more and more efforts have been made to monitor the source simultaneously in several wavelengths. These observations provide important constrains on the nature of the emission from Sgr A*. According to Zamaninasab et al. (2010), the best model to explain the X-ray/NIR variability is the orbiting hot spot model, which combines synchrotron emission, adiabatic cooling and inverse Compton (IC) scattering.

2.2.6 Polarization

Polarization as a unique probe of physical conditions in Sgr A* was accessed only recently. Observations of LP emission bear the potential to probe the magnetic field structure in the emission region and turbulence in the accretion flow of Sgr A*. Given the synchrotron nature of the radio/millimeter radiation of Sgr A*, we would expect high LP. However, detection of LP at low frequencies (≤ 86 GHz) has failed or was only marginal (Bower et al. 1999a,c, 2001; Yusef-Zadeh et al. 2007). Aitken et al. (2000) detected the polarized emission for the first time at higher frequencies ranging from 150 to 400 GHz. This suggests that the polarimetric investigation of Sgr A* can only be explored at short mm/submm regime. The follow-up observations made with the VLA, the BIMA array, and the Sub-Millimeter Array (SMA) confirmed that the polarized flux density increases systematically towards sub-mm wavelengths and that the polarized emission is variable (both in polarization degree and position angle) on time-scales down to less than a day (Bower et al. 2003, 2005a; Marrone et al. 2006b, 2007).

The linearly polarized mm/sub-mm emission in Sgr A* is suggested to originate within less than a few tens of R_{Sch} from the SMBH, perhaps in a magnetized accretion disk. Recent BIMA and SMA observations infer an external Faraday rotation measure of $\sim -(4...5) \times 10^5$ rad cm^{-2} and a position angle of $\sim 170°$ for the intrinsic polarization emission (Macquart & Bower 2006; Marrone et al. 2007). The implied low accretion rate is less than $2 \times 10^{-7} M_\odot$/yr (Marrone et al. 2007), which strongly argues against high accretion rate models (e.g., standard ADAF, Bondi-Hoyle models).

On the other hand, these observations, with typical angular resolution not better than $1''$, are not able to penetrate into the mm/sub-mm emission region. Depolarization caused by in situ Faraday rotation and by appreciable inhomogeneities in the rotation measures (RM) of an external Faraday screen are empirically thought to be unimportant. However, single dish/connected interferometers suffer from in-beam confusion from the surrounding diffuse emission on sub-mas scales. Furthermore, simulations of the emission from the accretion disk of Sgr A* (Bromley et al. 2001; Broderick & Loeb 2006; Huang et al. 2009a) predicted swings in polarization angle along the circumference of the accretion disk and a patchy distribution for the polarized emission. Averaging over the entire source of Sgr A* would underestimate the polarization degree. Comparatively speaking, VLBI observations at mm/sub-mm can in principle improve the resolution by four orders of magnitude and therefore could measure the polarization without beam dilution. Future polarization sensitive VLBI experiments will be of high importance (Fish et al. 2009).

Circular polarization (CP) is believed to be a common feature of quasars and blazars (Wardle et al. 1998; Homan & Wardle 1999; Macquart et al. 2000; Rayner et al. 2000; Homan & Lister 2006; Vitrishchak et al. 2008), and it has also been detected in Galactic micro-quasars (Fender et al. 2000; Macquart et al. 2002). Generally, CP peaks are associated with compact core regions, and the degree of CP (m_{cp}) is far less than the degree of LP (m_{lp}). Homan & Lister (2006) studied the statistical properties of CP in a flux limited MOJAVE sample. No evidence for any correlation between m_{cp} and other 20 properties of AGN was found.

Successful detection of circular polarization in Sgr A* using the VLA at 5 and 8 GHz was first reported by Bower et al. (1999b). This discovery came as a surprise in light of the absence of linear polarization at these frequencies. The detection was quickly confirmed independently by observation using the ATCA at 5 GHz (Sault & Macquart 1999). Bower et al. (2002) studied long-term behavior of CP in Sgr A*, and showed that the CP is variable on timescales of days to months with the degree of variability increasing with frequency. Moreover, the sign of circular polarization is constant over a time period of 20 yrs. The average spectrum of the m_{cp} is inverted between 1.4 and 15 GHz. On the theoretical side, the production of the observed circular polarization presently point more towards to the Faraday conversion of LP to CP (Wardle & Homan 2003). The conversion may be source intrinsic or also due to the scatter screen.

CP was also detected in M 81* (Brunthaler et al. 2001), a low-luminosity AGN (LLAGN) that behaves in many respects like Sgr A*. The polarization properties of Sgr A* and M 81* are similar in the sense that fractional circular polarization is far greater than fractional linear polarization ($m_{cp}/m_{lp} \gg 1$) (Brunthaler et al. 2006). This is generally thought to be in contrast to the polarization properties of most radio jets in AGNs. The similar polarization properties between Sgr A* and other LLAGNs suggest they share similar physics in the production of polarization.

2.3 Theoretical Models

Although the energy production in Sgr A* is widely believed to be black hole accretion in nature, the physical origin of the observed electromagnetic radiation is still uncertain. To explain the observed broad band quiescent emission of Sgr A*, a variety of scenarios have been proposed over the years. These include models where radiation is due to the accreting gas, e.g., Bondi-Hoyle type models (Melia 1994), advection-dominated accretion flow (ADAF) models or the radiatively inefficient accretion flow (RIAF) models (Narayan et al. 1995, 1998; Yuan et al. 2003, 2004) and models where

radiation comes from a jet (Falcke et al. 1993; Falcke & Markoff 2000) and hybrids of the above ideas (Yuan et al. 2002).

The Bondi-Hoyle accretion assumes spherical accretion of the plasma onto the black hole. The accretion flow is assumed to free-fall until a Keplerian disk is formed within a small radius. Since the timescales of the radiative cooling are much longer than those for protons channeled into the black hole, only electrons have enough time to radiate but they carry only a very small fraction of the energy. The low radiative efficiency naturally explains the low luminosity of Sgr A*. However, ignoring the angular momentum of the accreting gas seems to be an oversimplification. Advection-dominated accretion flows (ADAF) put more importance onto the angular momentum and viscosity of the plasma. They provide a natural explanation for the low luminosity of Sgr A* because most of the viscously dissipated energy is stored in the gas and carried into the black hole. This is due to the fact that viscous energy heats ions only and coupling between ions and electrons is very weak at low accretion rates. In other words, electron heating is inefficient.

Further investigations of radiatively inefficient models made additional assumptions of a hybrid of electron population consisting of both thermal and non-thermal electrons (Özel et al. 2000; Yuan et al. 2003). A small fraction of non-thermal electrons can explain the low-frequency radio spectrum, which was under-predicted by ADAF models (Narayan et al. 1998). The structure of RIAFs is also rather different from original ADAF predictions with most of the mass available at large radii lost to a flow or convective circular motions. The resulting low gas density close to the black hole therefore satisfies the low accretion rate required by linear polarization detections at high radio frequencies. Concerning emission mechanisms, the low frequency radio and IR emission is due to synchrotron emission from non-thermal electrons, while synchrotron emission from thermal electrons, as stated above, accounts for the submillimeter bump. Furthermore, the addition of bremsstrahlung emission at outer radii ($\sim$ 1$''$) explains the extended X-ray quiescent emission (see also Quataert 2002).

Falcke & Markoff (2000) showed that jet models also fit the quiescent spectrum of Sgr A* very well. Of particular importance in this model is the "nozzle component", which accelerates and collimates the plasma. Synchrotron emission and inverse Compton emission from the nozzle component dominate the sub-mm bump, as well as the high energy part of the spectral energy distribution (SED). To satisfy the limits imposed on the SED by IR observations, the electron energy distribution has to be narrow to suppress the optically thin emission. However, the non-thermal origin of quiescent X-ray emission is different from that in RIAF models, and seems to be inconsistent with the observed extended emission.

After the discovery of flare emission in X-rays and NIR from Sgr A*, there are many recent theoretical papers shedding light on flare models. The high degree of linear polarization of the IR flares points towards a synchrotron origin. The mechanism responsible for X-ray flares is less certain due to the high intensity variability of flares and their undetermined spectrum (section 2.2.4 and 2.2.5). Flares are probably caused by local events rather than a global increase in the accretion rate (Markoff et al. 2001).

Current flare models involving IC scattering processes have been favored (Eckart et al. 2004, 2006b; Liu et al. 2006a). Generally speaking, synchrotron models for the X-ray flares need harsh conditions. They require a continuous injection of very high energy electrons since the cooling time is much shorter than the duration of typical X-ray flares, but see also Dodds-Eden et al. (2009). Yuan et al. (2003, 2004) considered both scenarios for the IR and X-ray flares, i.e., a synchrotron + synchrotron self-Compton (SSC) model and a pure synchrotron model. In the former case, synchrotron emission from a single power law distribution of accelerated electrons produces the IR flare, while the X-ray flare is due to self-Comptonization of the IR photons. In the latter case, some electrons are heated into high temperatures, giving rise to IR flare through synchrotron emission, while some electrons are accelerated into a hard power law distribution, being responsible for X-ray flare emissions. The enhancement of electron heating/acceleration may be due to processes such as magnetic reconnection, shocks and stochastic acceleration. Eckart et al. (2004, 2006b) explained the IR and X-ray flares through the SSC emission of a compact source component emitting at sub-millimeter wavelengths. The X-ray emission is from IC scattering of the THz-peaked flare spectrum by the relativistic electrons and the emission at IR wavelengths possibly due to a combination of synchrotron and SSC emission. In contrast Yusef-Zadeh et al. (2006b) attribute the X-ray emission to IC scattering of submillimeter and IR photons.

In addition, there are alternative models which can explain the flaring activity of Sgr A* at a single frequency, such as the hot spot model (Broderick & Loeb 2006; Meyer et al. 2006a; Eckart et al. 2006a; Trippe et al. 2007; Eckart et al. 2008b). The success of this model lies in explaining the quasi-periodic oscillation (e.g., Genzel et al. 2003), which has been interpreted as the result of the orbital motion of matter in the inner parts of the accretion disk. The correlation between the flux variation and changes in the polarization properties in NIR also supports this scenario (Zamaninasab et al. 2010; Nishiyama et al. 2009).

2.4 Context and Aim of the Thesis

The evidence for the link between NIR/X-ray variability and the variability at radio through sub-millimeter wavelengths of Sgr A* has been increasing. Several observations have already shown the existence of a time delay of ~ 100 minutes of the low energy emission with respect to NIR/X-ray flares. Very often, however, the exact correspondence between individual NIR/X-ray and mm/sub-mm flares remains uncertain (Meyer et al. 2008). The frequency dependence of the variability and the observed time lags between various frequencies has been interpreted via a synchrotron self-absorbed blob which cools down via adiabatic expansion (Eckart et al. 2006b; Yusef-Zadeh et al. 2006b; Eckart et al. 2008c; Marrone et al. 2008; Yusef-Zadeh et al. 2008, 2009), although synchrotron cooling may also be non-negligible (Li et al. 2009).

From the time delays of emission peaks between various frequencies and the decay of the flares (van der Laan 1966), one derives the sub-relativistic expansion speed and source size of the flare emission region. Recently, Kunneriath et al. (2010) obtained an expansion speed of $V_{\mathrm{exp}} \sim 0.005$–$0.017\,c$ and a source size of about one R_{Sch}. However, the direct detection of such transient structure component(s), which could be directly related to flaring events, is still pending. At mm/sub-mm wavelengths, the source sizes of the flare emission is commensurate with the intrinsic size of Sgr A*, and therefore could be detected by VLBI observations. Millimeter-VLBI observations of Sgr A*, as being part of a coordinated multi-wavelength observing campaigns, are therefore important, as they allow to detect and relate possible structural variability on AU-scales to the flux activity observed at shorter wavelengths. The change in source structure (e.g., increase of source size, deviation of source structure from Gaussian distribution) could possibly be detected with VLBI at 3 mm (86 GHz) and perhaps even at 7 mm (43 GHz).

One goal of this thesis is to measure the source size, detect its variations, and search for possible deviations from point-like structure (via investigation of closure phase) on a time scale of ~ 10 days. In addition, since the radio variability is probably linked to the NIR/X-ray flare events, our aim is also to directly observe the plasma expansion and relate it to the flare activity. In order to achieve these goals, a monitoring program of Sgr A* at 13, 7, and 3 mm with the VLBA on 10 consecutive days during a global observing campaign was performed in May 2007 and this thesis presents the results of the analysis of these VLBI observations.

3 VLBI Observations at Millimeter Wavelength

VLBI can achieve the highest angular resolution of all astronomical instruments (Figure 3.1, Kellermann & Moran 2001). The resolution (θ) is related to the observing wavelength (λ) and the baseline length (D) by:

$$\theta \,(\text{in radians}) \propto \frac{\lambda}{D}. \tag{3.1}$$

Obviously, the angular resolution of ground-based centimeter-VLBI can be further increased, either by increasing the distance between the radio telescopes (e.g., VLBI Space Observatory Programme, Hirabayashi et al. 1998), or by observing at shorter wavelengths (Millimeter VLBI, e.g., The Global mm-VLBI Array, Krichbaum et al. 2008), or by a combination of both in the near future (e.g., Tsuboi 2008). Both approaches have their merits (Kellermann & Moran 2001). Besides holding the promise of delivering high resolution, mm-VLBI offers other advantages as well:

- The innermost region of AGNs is invisible at centimeter wavelengths due to intrinsic self-absorption, while the cores become increasingly optically thin at mm/sub-mm bands.

- Faraday depolarization becomes weak with decreasing wavelength (scales as λ^2).

- Scattering effects in the ionized ISM decrease with a λ^2 dependence.

Despite the scientific merit, there have always been some obstacles in the way towards mm-VLBI. At high frequencies (22 GHz and higher), VLBI observations suffer considerably from atmospheric effects, which affect both the phases - basically making the coherence times short and variable, and the amplitudes - making the antenna gains a strong function of elevation and time[4]. At the same time, mm/sub-mm-VLBI is demanding on both the antennas and the electronics. As a result, the sensitivity

---

[4]Elevation dependent gains are caused not only by the atmosphere, but also by the design of the antenna, which is often optimized for observations at longer wavelength
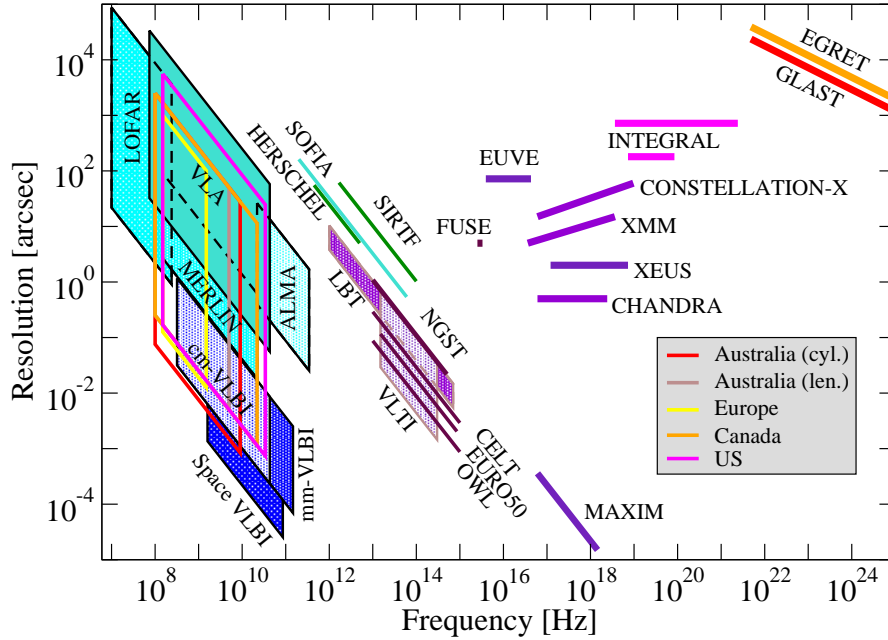
Figure 3.1: A plot of resolution versus frequency for astronomical instruments (taken from Lobanov 2007).

and image fidelity is still relatively low. However, regular 3 mm-VLBI observing is performed successfully and striking progress has been made during the past several years toward much higher frequencies (e.g., Krichbaum et al. 1998c; Doeleman et al. 2008). In the foreseeable future, sub-mm VLBI, even space mm/submm-VLBI, will be feasible with dedicated mm/sub-mm telescopes/arrays, like ALMA, APEX, SMA, CARMA (see Table 6.1 for a list of present and future mm-VLBI antennas).

In this chapter, we first review shortly the basics of radio interferometry and then describe the data calibration procedures mostly concentrating on the treatment of total intensity. Finally, some issues that arise at high frequencies are discussed. The historical development of high resolution radio imaging was reviewed by Kellermann & Moran (2001). More thorough and comprehensive discussions on the radio interferometry were presented in the book of Thompson et al. (2001) and in the proceedings of NRAO summer schools, e.g., Zensus et al. (1995).

3.1 Fundamentals of VLBI

3.1.1 Basic Relations

Here we start with an equation fundamental for interferometry, i.e, the *spatial coherence function* of the electromagnetic field radiated from a very distant celestial object:

$$V_\nu(u, v) = \iint I_\nu(x, y)e^{-2\pi i(ux+vy)}dx\,dy, \tag{3.2}$$

where $V_\nu(u, v)$ is the spatial coherence function relative to the direction of the phase tracking center measured in the so-called *uv* plane and $I_\nu(x, y)$ is the sky brightness distribution in the sky plane. Equation 3.2 tells us that the spatial coherence function and the sky brightness distribution are related by a Fourier transform. Thus the interferometer acts as a spatial filter and each pair measures one Fourier component of the brightness distribution. The sky brightness distribution can therefore be derived by an inverse Fourier transform:

$$I_\nu(x, y) = \iint V_\nu(u, v)e^{2\pi i(ux+vy)}du\,dv. \tag{3.3}$$

In practice, however, an array of antennas measures only certain values of the coherence function in the *uv* plane. The sampling effect can be described by a *sampling function $S(u, v)$*, which is zero where no data are sampled. Thus, an array of antennas actually provides the sampled spatial coherence function $S(u, v)V(u, v)$, instead of $V(u, v)$. By performing the inverse Fourier transform of the sampled spatial coherence function, one obtains the "dirty image" $I_\nu^D(x, y)$, given by:

$$I_\nu^D(x, y) = \iint V_\nu(u, v)S(u, v)e^{2\pi i(ux+vy)}du\,dv. \tag{3.4}$$

According to the convolution theorem, the dirty image is the convolution of the true brightness distribution $I_\nu(x,y)$ with the Fourier transform of the sampling function $S(u, v)$, $B(x, y)$, defined as:

$$B(x, y) = \iint S(u, v)e^{2\pi i(ux+vy)}du\,dv. \tag{3.5}$$

$B(x, y)$ is often referred to as the *synthesized beam*, *dirty beam*, or *point spread function*. Therefore, one needs an additional deconvolution step to obtain the true brightness distribution of the source.

3.1.2 Calibration

3.1.2.1 Fringe-Fitting

The complex visibilities from the post-observation correlation still suffer from errors in the atmospheric, geometric and clock models used by the correlator. These residuals should be removed to allow coherent data averaging, in time and frequency, in order to improve the signal to noise ratio (S/N) and reduce the volume of the data. The process of finding these residuals is known as fringe fitting.

It can be shown (Cotton 1995) that the interferometer phase ($\phi_{\nu,t}$) is related to the interferometer delay (τ_t) by:

$$\phi_{t,\nu} = 2\pi\nu\tau_t, \tag{3.6}$$

where ν is the observing frequency and the subscript "t" indicates the time dependence of the quantities. Based on equation 3.6, the correlator can estimate and remove the interferometer phase from the data. Correspondingly, the phase and delay errors are related by differentiating the above equation:

$$d\phi_{t,\nu} = 2\pi\nu d\tau_t. \tag{3.7}$$

The first order expansion of the interferometer phase error is:

$$\Delta\phi_{t,\nu} = \phi_0 + (\frac{\partial\phi}{\partial\nu}\Delta\nu + \frac{\partial\phi}{\partial t}\Delta t) \tag{3.8}$$

where $\Delta\phi_0$ is the phase error (in cycles) at the reference time and frequency, $\frac{\partial\phi}{\partial\nu}$ is the well known *delay*, or *delay residual*, and $\frac{\partial\phi}{\partial t}$ is known as the *rate* or *delay rate*. Thus, the delay and delay rate are the residual phase slope in frequency and time, and fringe fitting is an operation to flatten the visibility phases. Several fringe fitting algorithms were developed, including baseline-based methods, baseline-based with closure constrains, and antenna-based methods (global fringe fitting, similar to self-calibration, see section 3.1.2.3). In the case of a global fringe fitting, as used in the data reduction presented in this thesis, the sources of delay error can be decomposed to contributions from each antenna. The baseline dependent errors can then be expressed in terms of the differences of antenna specific errors. We refer the reader to Cotton (1995, and references therein) for a detailed discussion.

3.1.2.2 Amplitude Calibration

The basic relation between the amplitude of the correlation coefficient ρ_{12}, measured on baseline involving antennas 1 and 2, to the correlated flux density S_c (in Jy), is

given by:

$$S_c = \rho_{12} b \sqrt{\frac{T_{sys}^1 T_{sys}^2}{g_1 g_2}}, \tag{3.9}$$

where b compensates digitization and sampling loss, T_{sys}^1 and T_{sys}^2 are the off-source system temperatures (in K). g_1 and g_2 are antenna gains, defined as $g = \frac{T_a}{S} = \frac{\eta_a A}{2k}$ (in K/Jy), in which T_a is the antenna temperature, S is the flux density, η_a the antenna efficiency, A is the collecting area, and k the Boltzmann constant. The antenna gain is a function of antenna elevation and it is usually described by a polynomial function (POLY, the normalized gain curve) with the coefficient known as DPFU (Degrees Per Flux Unit). A useful quantity for describing the performance of an antenna is the system equivalent flux density (SEFD) given by $\frac{T_{sys}}{g}$.

The standard way of amplitude calibration in AIPS (Bridle & Greisen 1994) is to use the system temperatures and antenna gains/antenna temperatures. In principle, antenna temperatures offer a superior calibration since the measurements take into account the atmospheric as well as other effects (e.g., pointing errors or position-dependent gains) that affect the instantaneous gain of an antenna. However, there are some practical limitations, such as infrequent measurements, relatively large errors, and the inadequate sensitivity to measure the antenna temperature of a VLBI source with a small antenna like that of the VLBA. This leaves the *a priori* gain information and system temperature measurements as the principal way.

Opacity correction becomes necessary at high frequencies (Moran & Dhawan 1995). In most cases, the atmosphere can be assumed to be a parallel layer of absorbing gas, which has an effective physical temperature T_{atm}, and zenith opacity τ_0. Since the path length through the atmosphere is approximately proportional to $\sec z$ where z is the zenith angle, the total opacity τ is $\tau_0 \sec z$. The system noise temperature T_{sys} is then the sum of the attenuated signal from the source T_{src}, (usually can be ignored with the exception of some maser sources), the sky temperature, a contribution from the atmosphere, $T_{sky} = T_{atm}(1 - e^{-\tau})$, the receiver system temperature T_{rec}, and the "spill-over" from the ground T_{spill}:

$$T_{sys} = T_{src} e^{-\tau} + T_{atm}(1 - e^{-\tau}) + T_{rec} + T_{spill} \tag{3.10}$$

Since T_{sys} is frequently measured at different elevation angles, if the receiver temperature (and also the ground pickup due to spill over) can be accurately determined, the atmospheric attenuation e^{τ} can be calculated from the sky temperature T_{sky} (which is $T_{sys} - T_{rec} - T_{spill}(z)$) and T_{atm} (which can be estimated from ground temperature

measurements, for details, see Leppänen 1993, and reference therein):

$$e^\tau = \frac{T_{\text{atm}}}{T_{\text{atm}} - T_{\text{sky}}}. \tag{3.11}$$

Such opacity corrections can be done in AIPS with the task APCAL.

The so-called effective system noise temperature T_{eff}, the scaled T_{sys} (by multiplying e^τ) to a point outside of the atmosphere, then is:

$$T_{\text{eff}} = T_{\text{src}} + [T_{\text{atm}}(1 - e^{-\tau}) + T_{\text{rec}} + T_{\text{spill}}]e^\tau \tag{3.12}$$

3.1.2.3 Self-calibration

For the reconstruction of the source brightness distribution, two problems remain unresolved after fringe fitting and *a priori* amplitude calibration. The first one is the sparse *uv* sampling. As stated earlier, the spatial coherence function is only sampled at certain points of the *uv* plane. In order to remove the effect of missing spacings, one has to deconvolve the dirty beam from the image (see equation 3.5). Several methods of deconvolution have been developed using the CLEAN algorithm (Högbom 1974), which is a widely used method in radio astronomy. The algorithm is an iterative process, identifying and subtracting point sources (delta functions) from the dirty image until a desired noise level is achieved in the residual image. The other problem left is the residual errors in the amplitude and phase of the complex visibilities, which limit the image quality. Phase errors are more severe. In the early days of VLBI, the visibility phases were corrupted so that the hope of measuring the phase was low. The frequency standard was not stable enough to determine their phases. Nowadays, however, the limitations are mainly imposed by the atmosphere (see also section 3.2.1).

Fortunately, people realized that even uncalibrated phases and amplitudes carry information of the source structure based on the fact that most errors are antenna-based. This can be described by the following equation:

$$V'_{\text{i,j}} = G_{\text{i}} G_{\text{j}}^* V_{\text{i,j}}, \tag{3.13}$$

where $V'_{\text{i,j}}$ and $V_{\text{i,j}}$ are measured and true visibilities between antenna i and antenna j, and G_{i} and G_{j} are the complex gain factors of the antenna. The phase and amplitude component of the complex gain factors represent the amplitude and phase errors induced by the interferometer and during the propagation of the signal from the source to the observer.

Phase and Amplitude Closure

Closure phase

Realizing that the phase errors are mostly antenna-based, Jennison (1958) introduced the idea of closure phase to compensate for poor phase stability. The closure phase is the sum of the visibility phases around a closed loop of 3 baselines and it is free of any antenna-based phase errors. This can be illustrated by the following consideration. Let us assume that the instrumental phase errors are ϕ_1, ϕ_2 and ϕ_3 at 3 stations. Correspondingly, they contribute gain factors of $e^{i\phi_1}$, $e^{i\phi_1}$, and $e^{i\phi_1}$. The visibility phases on the three baselines will be:

$$\phi_{12} = \vec{b}_{12} \cdot \vec{s} + \psi_{12} + \phi_1 - \phi_2 \tag{3.14a}$$

$$\phi_{23} = \vec{b}_{23} \cdot \vec{s} + \psi_{23} + \phi_2 - \phi_3 \tag{3.14b}$$

$$\phi_{31} = \vec{b}_{31} \cdot \vec{s} + \psi_{31} + \phi_3 - \phi_1, \tag{3.14c}$$

where $\vec{b}_{ij}$ is the baseline vector, $\vec{s}$ the unit vector point to the source, and ψ_{ij} the true visibility phase caused by the source structure. The sum of the phases around this triangle yields:

$$\phi_{123} = \phi_{12} + \phi_{23} + \phi_{31} = \psi_{12} + \psi_{23} + \psi_{31}. \tag{3.15}$$

Therefore, closure phases can be used to derive source structure and for sources with point-symmetry, the closure phases are always $0°$ or $180°$ (Monnier 2007). The number of independent closure phases for N stations can be worked out by forming all triangles between one station and the rest of them, i.e., "N−1 choose 2", $\frac{(N-1)(N-2)}{2}$ (Thompson et al. 2001).

Closure Amplitude

For four antennas, it is possible to form visibility amplitude ratios that are independent of antenna gain factors. These ratios are called closure amplitudes and are defined as:

$$A_{1234} = \frac{|V'_{12}||V'_{34}|}{|V'_{13}||V'_{24}|} = \frac{g_1 g_2 |V_{12}| g_3 g_4 |V_{34}|}{g_1 g_3 |V_{13}| g_2 g_4 |V_{24}|} = \frac{|V_{12}||V_{34}|}{|V_{13}||V_{24}|}. \tag{3.16}$$

If all six visibilities are formed by the four stations, three different closure amplitudes can be calculated (A_{1234}, A_{1243}, A_{1432}) with only two of them being independent. With an array of N antennas, there are $\frac{N(N-3)}{2}$ independent closure amplitudes, which is equal to the number of baselines between all antennas minus the number of antennas (Doeleman et al. 2001).

Self-calibration is the method to calculate antenna gains using of both phase and amplitude closure relations to obtain the information about the error-free fringe visibility. Readhead et al. (1980) applied image deconvolution and self-calibration together

in an iterative process known as hybrid mapping (Cornwell 1995). One problem about this technique is that the independent closure phase and closure amplitude relations are not enough to uniquely solve for the true visibilities. With N antennas, the fraction of total visibility information contained in the closure relations is $\frac{N-2}{N}$ in the closure phases and $\frac{N-3}{N-1}$ in the closure amplitudes. With large arrays, such as the VLBA (10 antennas), a large fraction (80 %) of the phase and amplitude information is available. It has been shown that in most cases self-calibration does converge to a unique solution, however, no proof has ever been given and concerns about this uniqueness persist. More discussions on this topic can be found in Pearson & Readhead (1984); Cornwell & Fomalont (1999).

3.2 Unique Issues of mm-VLBI

The effect of the troposphere at millimeter wavelength makes the most important difference between mm-VLBI and cm-VLBI. Besides this, both the antennas and the electronics are demanding at millimeter wavelength for those build mainly for cm-VLBI. Consequently, the sensitivity of mm-VLBI observations is reduced and as a result the number of observable sources is still limited (Lee et al. 2008). Here we summarize some issues which arise at higher frequencies so that the difficulties and the room for improvement can be easily understood.

3.2.1 Troposphere

The troposphere is the lowest portion of the Earth's atmosphere, extending from the ground to the stratosphere at an elevation of 7–10 km. The principal components of the opacity τ, (or absorption, see section 3.1.2.2) are due to the pressure broadened wings of the resonance lines of water vapor (22 and 183 GHz) and oxygen (near 60 and 118 GHz). Opacity decreases a source flux S to $S e^{-\tau_a \sec z}$. At the same time, the atmosphere's emission contributes to the system noise as $T_{\mathrm{am}}(1 - e^{-\tau_a \sec z})$ (see section 3.1.2.2).

The water vapor contribution to the opacity can be time variable due to the fluctuation of the column density (normally quantified as precipitable water vapor, PWV, which is the depth of water vapor in liquid state). Changes in the PWV lead to changes in the refractive index, namely the change of the additional path length of the signal, and therefore cause phase noise. Except in the vicinity of the strong water lines, this effect increases linearly with frequency (see e.g., Carilli et al. 1999, for details). Although the bulk delay, caused by the additional path length of the atmosphere, has been

taken into account by the correlator, the remaining residuals of the delay cause phase fluctuations which severely limit the coherence time for the high-frequency VLBI detection. At 3 mm wavelength, for example, the coherence time under average conditions and at sites of moderate altitude is limited to $\sim 10\,s$ (Rogers et al. 1984).

To mitigate the effects introduced by the troposphere phase fluctuations, several methods have been developed. *Self-calibration* (section 3.1.2.3) allows to reduce the phase errors where the target source itself is used as a phase calibrator. However, it requires a sufficiently strong source to be detected within a coherence time. *Phase referencing* aims at canceling the atmospheric effects by applying the phase correction derived from an apparently nearby calibrator. It therefore permits extension of the coherence time. At millimeter wavelengths, this has been limited to only very few exceptional cases as the short coherence time does not allow an antenna switching pointing between sources (Porcas & Rioja 2002). Similarly, one may reference the phase at higher frequencies to lower frequencies (fast frequency switching, Middelberg et al. 2005) because the troposphere path delay is non-dispersive over a wide range of frequencies (frequency independent). In addition, the limited coherence time could also be lengthened if attempts to measure the path-length fluctuations in the atmosphere with Water Vapor Radiometers (WVR) are successful (e.g., Roy et al. 2007).

3.2.2 Antennas and Electronics

3.2.2.1 Antennas

The efficiency of a radio antenna has several components, e.g., efficiencies due to the surface accuracy, blockage, spillover, illumination, etc. (Moran & Dhawan 1995). The surface efficiency (η_{sf}) of an antenna is related to the rms of the random surface errors (ϵ) by the Ruze formula:

$$\eta_{\mathrm{sf}} = e^{-(\frac{4\pi\epsilon}{\lambda})^2}. \tag{3.17}$$

For a normal tolerance $\epsilon = \lambda/20$, η_{sf} is 67 %. At 3.5 mm, one has to achieve $175\,\mu\mathrm{m}$ accuracy over the antenna surface. This is often demanding for large antennas.

Pointing errors are often significant for mm-VLBI, as antennas are operated at off-design frequencies. These can be considerably large because the sources are not detectable in total power mode by small antennas and consequently pointing corrections can not be done during the observations. Moran & Dhawan (1995) showed that the fractional gain/effective collecting area loss can be expressed as:

$$\frac{\sigma_A}{<A>} = \frac{r^2}{\sqrt{1 + 2r^2}}. \tag{3.18}$$

Here we assume that the collecting area of an antenna is a Gaussian function ($< A >$ and σ_A are the expectation and rms of the effective collecting area) and that r is related to the full width at half maximum w and the pointing error σ_p by $r = \sqrt{8\ln 2}\frac{\sigma_p}{w}$. Since w is approximately $1.2\lambda/d$, it is easy to understand that pointing errors are more severe at short wavelengths.

3.2.2.2 System Noise Temperature

It can readily be seen from equation 3.12 that the system temperature depends largely on the emission from the atmosphere ($T_{am}(1 - e^{-\tau_a \sec z})$), and the receiver noise temperature. Consider a series of amplifiers of gain G_i and noise temperature T_i. The noise temperature of their combination is given by (each additional amplifier acts on the input signal and noise):

$$T = T_1 + \frac{T_2}{G_1} + \frac{T_3}{G_1 G_2} + ..., \tag{3.19}$$

where the gain G_i is the numerical gain, not the dB gain.

In centimeter wavelength receivers, astronomical signals are first amplified by the low noise transistor amplifiers (LNAs), which usually use a low noise high electron mobility transistor (HEMT) as the amplifying element, and down-convert the signal with a planar Schottky mixer at ambient temperature. The noise temperature of the receiver is dominated by the LAN itself, with a typical receiver temperature of about 10 K and a gain of about 30 dB (Carilli et al. 1999). Comparatively speaking, it is not possible to built LNAs above 115 GHz, which leads the first element in the receiver to necessarily be a mixer. At high frequencies, conventional Schottky barrier diode mixers can attenuate the incoming signal before amplification with significant losses (e.g., $G \sim 0.2$ at 230 GHz) (Carilli et al. 1999). According to equation 3.19, the receiver noise temperature would be $T_{re} = T_{mix} + 5 \times T_{IF}$, where T_{IF} is the intermediate frequency (IF) amplifier noise temperature. The loss in the mixer increases the effective amplifier noise by a factor of five, even though the noise from the mixer is low. At frequencies above 115 GHz, superconductor-insulator-superconductor (SIS) mixers, operating at low temperatures, are generally used. The high gains (~ 1) consequently relax the requirement for low noise temperature of the first IF amplifier. One firm constrain on the receiver noise temperature is the quantum limit, $h\nu/k$, which makes the receiver system noise $\propto \nu$.

3.2.2.3 Recording

Although frequency independent, data recording rate remains a factor to be improved for mm-VLBI. It limits the observing bandwidth, and in turn reduces the detection sensitivity. The current maximum recording rate at the VLBA is 512 Mbps. However both VLBA[5] and EVN[6] are expected to implement a wideband recording system, up to 4 Gbps, in the very near future. Increases in recording rates to 16 Gbps are foreseen over the next 10 years.

3.2.3 Present Sensitivity

Since the first ad-hoc VLBI observations at 3 mm in the early 1980s (Readhead et al. 1983), the Coordinated Millimeter-VLBI Array (CMVA, Rogers et al. 1995b) and the Global Millimeter VLBI Array (GMVA)[7] were sequentially put into service, which made VLBI at 3 mm more accessible to worldwide users. As a successor to the CMVA, GMVA consists of 8 VLBA antennas equipped with 3 mm receivers and 5 European radio telescopes (see the GMVA website for details), achieving an angular resolution of typically 50–70 μas. The participation of large, and therefore sensitive, European antennas (IRAM 30 m at Pico Veleta (Spain), the phased 6-element PdBI (France), and the 100 m telescope in Effelsberg (Germany)) provides 3–4 times more sensitivity than the stand-alone VLBA and offers a single baseline sensitivity of up to ~ 0.1 Jy (7σ) and array sensitivity of a few mJy.

Until recently, achievable detection thresholds with existing global arrays has been restricted 3 mm VLBI observations to the brightest AGN. The present situation and future prospects of mm-VLBI are easily explained in terms of the sensitivity formula for a two-element VLBI interferometer with diameters of D_i and D_j in meters for each element (Krichbaum 1996):

$$\sigma_{ij} = 2.458 \cdot 10^6 \cdot \frac{1}{C_1} \cdot \frac{1}{D_i \cdot D_j} \cdot \frac{\sqrt{\frac{T_{sys}^i}{\eta_i} \cdot \frac{T_{sys}^j}{\eta_j}}}{\sqrt{\triangle\nu \cdot \triangle t}}. \tag{3.20}$$

Here C_1 is an efficiency factor taking into account the quantization and correlator losses (0.64 and 0.88 for 1-bit and 2-bit sampling), η is the aperture efficiency, $\triangle\nu$ is the bandwidth in MHz, and $\triangle t$ is the integration time in seconds.

---

[5] www.vlba.nrao.edu/astro/obstatus/current/node24.html

[6] www.mpifr − bonn.mpg.de/div/vlbicor/tog_chair/tog.html

[7] www.mpifr − bonn.mpg.de/div/vlbi/globalmm/index.html

Coherence time is mainly limited to a few up to a few tens of seconds by the atmosphere and local oscillator phase noise. Incoherent averaging of coherent segments can extend the effective integration time in the initial fringe search, but the SNR improves more slowly ($\sqrt[4]{t}$) than $\sqrt{t}$ (Rogers et al. 1995a). Limitations on the antenna size, aperture efficiency, and system temperature do not allow a considerable improvement of the detection sensitivity. It follows from equation 3.20 that high bandwidth VLBI recording systems coupled with large mm/sub-mm apertures are the only way for drastic enhancement of future mm-VLBI experiment (Krichbaum 1996).

4 High Frequency VLBI observations of Sgr A*

In this chapter, results from a multi-frequency inter-day Very Long Baseline Array (VLBA[8]) monitoring of Sgr A* are presented and discussed. As explained in Chapter 2, Sgr A* is the compact radio, NIR, and X-ray source associated with the SMBH at the center of the Galaxy. It has been studied with VLBI observations performed on consecutive days and at mm wavelengths. We monitor Sgr A* with VLBI, aiming at the detection of correlated variations in the sub-milliarcsecond structure, flux density and polarization. We searched for jet-like emission occurring after NIR-flares and on sub-milliarcsecond scales. We observed Sgr A* with the VLBA at 3 frequencies (22, 43, and 86 GHz) on 10 consecutive days in May 2007 during a global multi-waveband campaign (see section 4.1). From this we obtained accurate flux densities and sizes of the, at mm-wavelengths partially resolved, VLBI structure.

The coordinated (sub-)mm/NIR observing campaign on Sgr A* was performed between 15–24 of May 2007, using world wide observing facilities including the VLBA, the CARMA, the ATCA, both IRAM telescopes (30 m Pico Veleta, 6× 15m Plateau de Bure), the Effelsberg 100 m telescope, and the VLT. The main goal was to investigate the variable emission from Sgr A* in order to obtain a better understanding of the underlying physical processes in the accretion flow and a possible outflow. High resolution VLBA observations are able to detect variations in the structure and flux density of Sgr A* on AU-sized scale, and can be used to further understand the flare characteristics together with the studies in the NIR. Some results from this campaign have already been reported (e.g., Eckart et al. 2008a,b; Kunneriath et al. 2010; Lu et al. 2008; Zamaninasab et al. 2010).

---

[8]The National Radio Astronomy Observatory is a facility of the National Science Foundation operated under cooperative agreement by Associated Universities, Inc.

4.1 Observations and Data Analysis

During the coordinated observing campaign, Sgr A* was observed with the VLBA[9] for 8 hours per day, spending about one third of the time on each of the three observing frequencies. Each VLBI station recorded dual circular polarization at a recording rate of 512 Mbps (8 IF channels, 16 MHz per IF, and 2 bits per sample). The target source (Sgr A*) and the calibrators (VX Sgr, NRAO 530, PKS 1749+096, 3C 279, 3C 446) were observed in frequency switch mode, cycling between 86, 43 and 22 GHz in a duty cycle of 11–13 minutes between all 3 frequencies. At 22 GHz, the individual VLBI scans had a duration of 3 minutes, and at 43 & 86 GHz of 4 minutes, respectively. The bright quasars PKS 1749+096, 3C 279, 3C 446 were observed as fringe tracers for total intensity and cross-polarization in the beginning and at the end of each VLBI experiment on each day. The quasar NRAO 530 was observed more regularly, serving as a fringe tracer and in order to provide consistency checks for the amplitude calibration. The SiO maser in VX Sgr (transitions $v = 1$, $J = 1 \rightarrow 0$ and $J = 2 \rightarrow 1$) was observed in interleaved short VLBI scans of 1 minutes duration, and only at 43 and 86 GHz. These spectral line measurements were made to complement the regular system temperature measurements and for an improved amplitude calibration via their auto-correlation functions. All data were correlated at the VLBA correlator in Socorro, NM, USA with 1 s integration time.

The data were analyzed in AIPS using the standard algorithms including phase and delay calibration and fringe fitting. The amplitude calibration was performed using the measurements of the antenna system temperatures and *a priori* gain-elevation curves for each station. Atmospheric opacity corrections were applied using the AIPS task "APCAL" from fits of the variation of the system temperature when plotted against air mass. Images of Sgr A* were finally produced using the standard hybrid mapping methods in AIPS and with *difmap* (Shepherd 1997) at all three frequencies. During the imaging process and the step-wise iterative amplitude self-calibration, the correctness of the station gain solutions was monitored and controlled via a comparison with independent solutions obtained on the calibrator continuum sources NRAO 530, PKS 1749+096 and from the auto-correlations on the spectral line emission of VX Sgr.

VLBI observations at millimeter wavelengths have a number of limitations mainly induced by the variable weather and higher atmospheric opacity, and limitations of the telescopes (e.g. steeper gain curves, larger residual pointing and focus errors),

---

[9]The VLBA consists of ten 25-meter antennas, i.e., Brewster (BR), Fort Davis (FD), Hancock (HN), Kitt Peak (KP), Los Alamos (LA), Mauna Kea (MK), N. Liberty (NL), Owens Valley (OV), Pie Town (PT), and Saint Croix (SC).
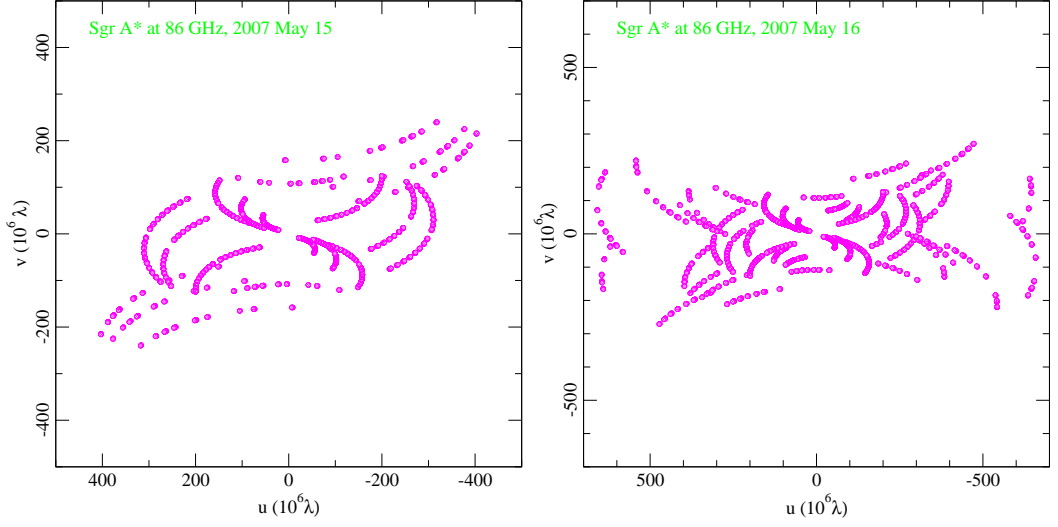
Figure 4.1: *uv* coverage plots of 86 GHz VLBA observations of Sgr A* on May 15, 2007 (left) and May 16, 2007 (right). Note the different scales. The difference is due to missing fringes for the FD and NL antennas at the first epoch.

which were mainly built for observations at the longer centimeter wavelengths. For telescopes in the northern hemisphere, the relatively low culmination elevation of Sgr A* at the VLBA antennas requires a careful observing and calibration strategy. Despite our best efforts, mm-VLBI observations of Sgr A* are still subject to residual calibration inaccuracies, which are larger than for sources of higher declination. Owing to the low declination of Sgr A*, the *uv* coverage is elliptical, resulting in a lower angular resolution in the north-south than in the east-west direction. This can be seen from the two examples (one good, one not-so-good) in Figure 4.1, where we show the *uv* coverages at 86 GHz for the first two epochs.

The *uv* coverage leads to an elliptical observing beam and hence lower positional accuracy for structural components, oriented along the major beam axis (see Table 8.1 in Appendix B). However, since the source structure of Sgr A* is very symmetric and almost point-like (zero closure phase, see section 4.2.6), the source size can be reliably estimated by fitting Gaussian components to the visibilities and by comparing that size with the size and orientation of the actual observing beam.

4.1.1 Accuracy of Amplitude Calibration

To measure the structure of Sgr A*, amplitude calibration is not trivial and a lot of effort was put to more accurate amplitude calibration. We modeled the left- and right-handed parallel polarization correlated visibilities (LL and RR) separately for both

Table 4.1: Flux density ratios between LL and RR for NRAO 530 and Sgr A* at 22, 43, and 86 GHz.

Epoch	NRAO 530	Sgr A*	NRAO 530	Sgr A*	NRAO 530	Sgr A*
	22 GHz		43 GHz		86 GHz	
May 15	1.013	1.013	1.031	1.010	1.007	1.025
16	1.031	1.017	1.010	1.060	1.044	1.010
17	1.032	1.048	1.045	1.026	1.000	0.980
18	0.978	1.000	1.010	1.006	1.108	0.966
19	1.013	1.053	1.010	1.011	1.059	0.992
20	1.009	1.018	1.005	1.006	1.074	1.048
21	1.009	1.052	1.010	1.036	1.063	1.045
22	1.000	1.038	1.010	1.022	1.121	1.008
23	1.022	1.015	1.020	1.027	1.045	1.022
24	1.027	1.015	0.990	1.017	1.056	0.993
mean	1.013	1.027	1.014	1.022	1.058	1.009
σ ($\times 10^{-2}$)	1.628	1.902	1.499	1.661	3.813	2.683

NRAO 530 and Sgr A* at 22, 43, and 86 GHz. In Table 4.1 we compare the flux density derived from LL and RR for both Sgr A* and NRAO 530. The closeness to unity of the ratio (LL/RR) for both sources provides an additional check for the reliability of the amplitude calibration. We see from Table 4.1 that for both sources the LL flux is slightly larger than the RR flux, indicating a small uncorrected instrumental polarization offset, consistent with zero circular polarization of either source.

At 22 and 43 GHz, we imaged and self-calibrated the data of Sgr A* following standard procedures. The overall antenna gain corrections are verified by those derived from self-calibration of NRAO 530 and PKS 1749+096. The agreement between corresponding gain correction factors is better than 10 %. At these two frequencies, the total flux densities of NRAO 530 are well reproduced, with rms fluctuations between epochs at a level of 1 %, and 2 %, respectively. PKS 1749+096 reproduces its flux slightly worse mainly owing to the more limited *uv* coverage. At 22 and 43 GHz, we determine the overall accuracy of the amplitude calibration to be $\sim 3-5$ %.

At 86 GHz, the flux densities of Sgr A* were determined mainly on the basis of the short *uv* spacing data (between 20 and 100 $M\lambda$), and after careful data editing. Owing to Sgr A*'s lower elevation, the amplitude scaling factors applied are in general somewhat larger than those applied to NRAO 530, but they show the same trend. The differences are in the range of the expected atmospheric opacity fluctuations, since

Sgr A* is $\sim 16°$ further south in declination than NRAO 530. They also incorporate weather dependent residual gain errors, which appear from the time interpolation of gain-solutions using nearby calibrator scans. The amplitude correction factors obtained from Sgr A* and NRAO 530 agree within less than 20 %, resulting in an upper limit for the calibration error of the total flux density, which is consistent with the scatter of the visibilities within $100\,M\lambda$ at 86 GHz. We therefore conclude that the accuracy of the overall amplitude calibration at 86 GHz is ~ 20 %. The flux densities of NRAO 530 reproduce at a level of ~ 6 % (see Table 4.3) which defines the repeatability of the system at this level and allows the investigation of flux density variations of Sgr A* at 86 GHz (section 4.2.2).

The parameterization of the VLBI source structure was done by Gaussian model fits to the visibilities. Formal errors for the individual fit parameters were determined using the approach described in Krichbaum et al. (1998a). Briefly, we took as a measure of uncertainty for each parameter the scatter from "best fit" models, which were obtained from slightly different calibrated and edited datasets. A more detailed description of the error analysis of the individual structure parameters is given in the corresponding sections of this chapter.

4.2   Results and Discussion

4.2.1   Clean Images and Model-fitting Results

In Figure 8.1 of the Appendix B, we show the resulting hybrid images at 22, 43 and 86 GHz for the 10-day campaign. For a better visualization, we also convolved the images with circular restoring beams as shown in the inset of each image. In Table 8.1 the parameters of these images are summarized. All the images show emission east-west oriented along a P.A. of $\sim 80°$. For Sgr A* we measured the total flux density by fitting a circular Gaussian component to the edited and fully self-calibrated visibilities of each VLBI observation after having made CLEAN maps for each epoch using the *difmap* software. The results of the individual model fits are shown in Table 8.2 in Appendix B. The first column gives the observing epoch, column 2 lists the observing frequency in GHz. The modeled flux density is shown in column 3. The last 3 columns contain the source structure parameters, i.e., the angular size along the major axis (column 4), the ratio between the major and minor axis (column 5), and the P.A. of the major axis (column 6).

In Figure 4.2 we show an example of correlated flux density versus *uv* distance for the second epoch at 43 GHz. The short *uv* spacing data ($\lesssim 250\,M\lambda$) are well fitted by

an elliptical Gaussian model (see Table 8.2). At *uv* distance longer than $\sim 250\,M\lambda$, the amplitude gradually shows slightly slow fall off over that expected from the model. Being always positive, however, the amplitude suffers from a positive noise bias against very low SNR visibilities. The discrepancy of about 0.1 Jy at the longest *uv* distance is consistent with this noise bias (Bower & Backer 1998).
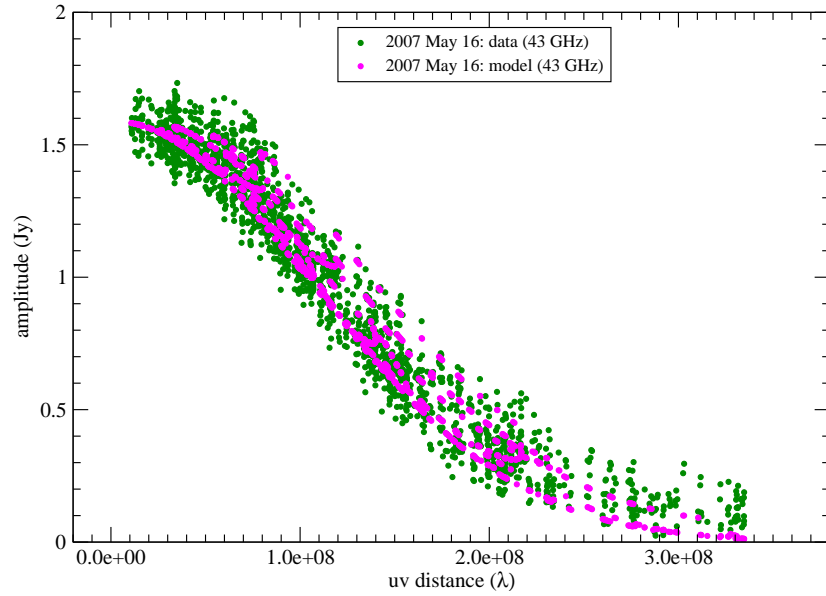
Figure 4.2: A plot of correlated flux density vs. *uv* distance at 43 GHz for the second epoch (May 16, 2007). An elliptical Gaussian model (see Table 8.2) is also displayed (magenta filled circles).

4.2.2 Flux Density Variations and the Spectrum

Figure 4.3 shows the flux density of Sgr A* (and of NRAO530 used as a secondary calibrator) obtained from each VLBI experiment on a daily basis at 22, 43, and 86 GHz. The 10-day average flux density is 1.33 ± 0.04 Jy at 22 GHz, 1.79 ± 0.05 Jy at 43 GHz, and 3.35 ± 0.16 Jy at 86 GHz (Table 4.2). The flux density variations of Sgr A* appear more pronounced at the beginning of the campaign, during a time which coincides with the two detected NIR flares on May 15 and May 17, 2007 (Eckart et al. 2008b; Kunneriath et al. 2010, see section 4.2.7). We defer the discussion of a possible relation of the two (variabilities) to section 4.2.7. The flux density variations seen at 22, 43 and 86 GHz appear highly correlated (indicated by the similar shape of the light curves), being progressively more pronounced towards the higher frequencies.

The average flux density at 22 GHz is comparable to measurements conducted dur-
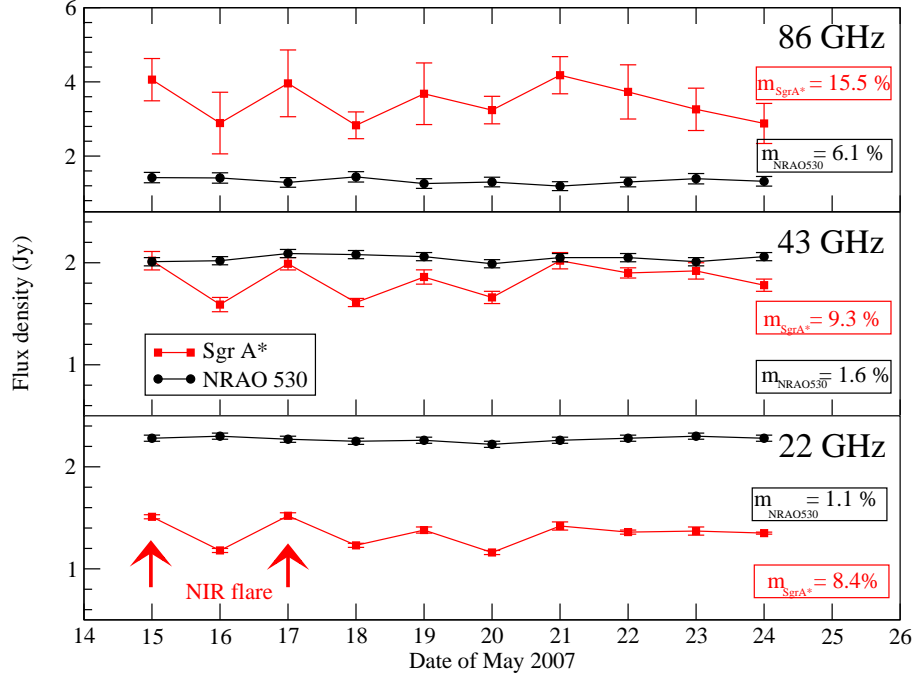
Figure 4.3: Light curves for Sgr A* and nearby quasar NRAO 530 at 22, 43, and 86 GHz. Two arrows indicate the NIR flares detected on May 15 (Eckart et al. 2008b) and 17, and there is another possible mm flare on May 19 (Kunneriath et al. 2010). In boxes, the variability index m is given for Sgr A* and NRAO 530 at each frequency.

ing 1990–1993 (Zhao et al. 2001). However, during our observations, Sgr A* appears brighter than in previous Very Large Array (VLA) observations at 22 and 43 GHz during 2000–2003 (Herrnstein et al. 2004). A "high" flux density state of Sgr A* is also seen at 86 GHz, where the present flux is much higher than previous flux densities observed in 1996–2005 with the Nobeyama Millimeter Array (NMA) (mean value 1.1 ± 0.2 Jy, Miyazaki et al. 2005), and is comparable with the highest fluxes seen in October 2007 with the ATCA (~ 4 Jy, Li et al. 2008).

In the following we discuss the significance of a possible day-to-day variability seen in the light curves of Figure 4.3. For comparison, we also plot the total VLBI fluxes of the nearby quasar NRAO 530, as measured in the same manner as for Sgr A* by Gaussian model fits. In Table 4.3 we compare the variability indices m (defined as the ratio between the standard deviation and the mean; $m = \frac{\sigma}{<S>}$) between Sgr A* and NRAO 530 at the 3 frequencies. In all cases, Sgr A* shows higher values of m, and therefore variations with larger amplitudes than NRAO 530 (see Figure 4.3).

We performed χ^2-tests to characterize the significance of the variability, following e.g., Kraus et al. (2003, see also Appendix 7). For the reduced χ^2_ν we obtain values

Table 4.2: Average source model parameters of Sgr A*.

ν [GHz]	S [Jy]	θ_{major} [mas]	θ_{minor} [mas]	P.A. [deg]
22.2	1.33±0.04	2.56±0.01	1.44±0.03	79.5±0.4
43.1	1.79±0.05	0.71±0.01	0.40±0.01	82.0±0.6
86.2	3.35±0.16	0.21±0.01	0.13±0.01	83.2±1.5

Note: Listed are the observing frequency in [GHz], weighted mean of the total flux density in [Jy], the major axis of the elliptical Gaussian in [mas], the minor axis in [mas], and of the position angle of the major axis. Note that the minor axes and position angles at 86 GHz are averaged over epochs where elliptical Gaussian is available

Table 4.3: Flux density variability characteristics of Sgr A*.

ν [GHz]	$m_{\text{Sgr A*}}/m_{\text{NRAO530}}$ [%]	Y [%]
22.2	8.4/1.1	25.0
43.1	9.3/1.6	27.5
86.2	15.5/6.1	42.7

Note: Listed are the observing frequency in [GHz], the modulation index, and the variability amplitude.

of 32.2 at 22 GHz, 7.5 at 43 GHz, and 0.9 at 86 GHz. The corresponding probabilities for the source being non-variable are far less than 0.01 % at both 22 and 43 GHz. At 86 GHz, however, the probability for Sgr A* being non-variable is only 48.8 % due to the larger measurement errors. Despite being formally insignificant, the variations at 86 GHz appear to correlate with the variations seen at the two lower frequencies. To describe the strength of the variability, the modulation index m and the variability amplitude Y (defined as $3 \times \sqrt{m^2 - m_0^2}$, where m_0 is the modulation index of the calibrator NRAO 530) are summarized in Table 4.3. Y corresponds to a 3σ variability amplitude, from which systematic variations m_0, which are still seen in the calibrator, are subtracted (Heeschen et al. 1987). For Sgr A* the Y values range between 25 % and 43 %.

The observed day-to-day variations compare well with similar variations seen by other authors at other times. Using the VLA, Yusef-Zadeh et al. (2006a) found an increase in the flux density at a level of 4.5 % at 22 GHz and 7 % at 43 GHz on time scales of 1.5–2 hours. At 94 GHz, Li et al. (2008) observed intra-day variability (IDV) with amplitude variations of 22 % within 2 hours in August 2006, which confirmed previously reported IDV by Mauerhan et al. (2005).

Since, for Sgr A*, each VLBI track lasted about 6–7 hours, we are not able to detect flux density variations on time scales shorter than this. A splitting of the VLBI coverage in shorter intervals, e.g. in two or three coverages of equal duration, does not allow total source flux measurements with sufficient accuracy (main limitation: *uv* coverage and lack of secondary calibrator scans) and therefore prevents the significant detection of variability on time scales shorter than 6 hours. A non-stationary source, which would vary with a large amplitude during the time of the VLBI experiment, however, would cause significant image degradation, leading to a reduced dynamical range in the CLEAN maps and the emergence of side lobes. Since this is not observed, we can exclude variations which are much larger than our typical amplitude calibration errors of 10–30 %, on timescales shorter than the duration of the VLBI experiments.

From the measured total flux densities, we calculated a 3-frequency spectral index between 22 and 86 GHz (defined as $S_\nu \propto \nu^\alpha$). We obtain an inverted spectrum, with spectral indices ranging between 0.44 ± 0.04 and 0.64 ± 0.05. For Sgr A*, a frequency break in the spectrum was suggested between ~ 20–100 GHz (Falcke et al. 1998; Zhao et al. 2003; An et al. 2005). Below this break frequency, the spectral slope is much shallower than that at higher frequencies, where the so called sub-mm excess causes an increase of the inverted spectral index (Serabyn et al. 1997; Krichbaum et al. 2006). Our observing frequencies are just in the transition region between cm- and sub-mm range. Therefore the measured spectral indices are slightly higher than pre-

viously reported spectra, resulting from VLBI at cm-wavelengths. An et al. (2005) made simultaneous multi-wavelength observations of Sgr A* in 2003. They described the spectrum from short centimeter (3.6 cm) to millimeter (0.89 mm) wavelengths as $S \propto \nu^{0.43}$. Falcke et al. (1998) measured a spectral index of 0.52 between 7 mm and 2 mm wavelength. The determined spectral indices reported here are fully consistent with these previous studies, and confirm the onset of the sub-mm excess.

In Figure 4.4 we show spectra measured during a "quiescent" (May 18) and a "flare" (May 21) state. A quasi-simultaneous spectrum from a multi-wavelength campaign taken roughly one month before our observations is also presented for reference (filled circles). Both spectra from May 2007 show clear evidence of spectral curvature, in the sense that the 43 to 86 GHz spectral index is more inverted that the spectral index between 22 and 43 GHz. If we use the mean flux density (see Table 4.2) obtained during our 10-day observations, we find that the spectral index increases from 0.43 between 22 and 43 GHz to 0.90 between 43 and 86 GHz. This indicates that the sub-mm excess becomes clearly visible above $\nu \geq 43$ GHz.
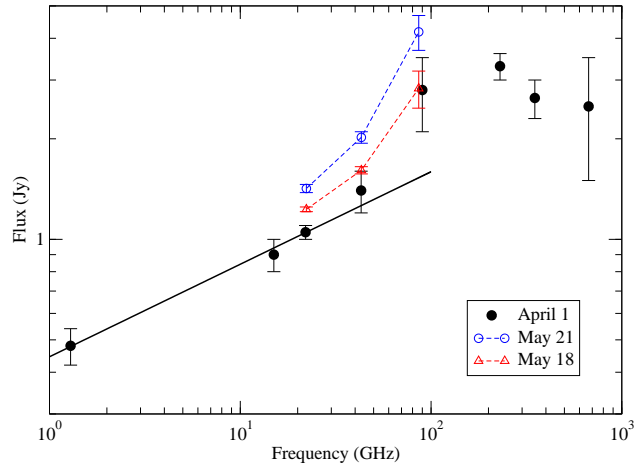
Figure 4.4: Spectrum of Sgr *A. Shown with filled circles is a quasi-simultaneous spectrum estimated from data obtained in time near to April 1, 2007 from another multi-wavelength campaign (Yusef-Zadeh et al. 2009). The error bars on the data indicate the variability of Sgr A*. A power law fit to radio data up to 43 GHz is shown by the solid line. Above 43 GHz, there is a flux density excess over this line. Open symbols connected by dashed lines are our measured flux densities on May 18 and 21, from which the minimum and maximum values of the spectral indices were derived.

Following Herrnstein et al. (2004), we plot the spectral indices as a function of flux density at 86 GHz in Figure 4.5. The obvious correlation between 86 GHz flux ($S_{86\,GHz}$) and spectral index (α) can be described by the following linear relation using

a regression analysis:

$$\alpha = 0.12(\pm 0.15) + 0.12(\pm 0.05) \times S_{86\,\mathrm{GHz}}. \qquad (4.1)$$

We note an earlier determination of the spectral index during a particular low flux density state reported by Falcke et al. (1998), which we have added to Figure 4.5[10] (open circle). It is in very good agreement with the linear relation from above and suggests that the correlation holds also for lower flux densities of $< 2\,\mathrm{Jy}$ (Serabyn et al. 1997).
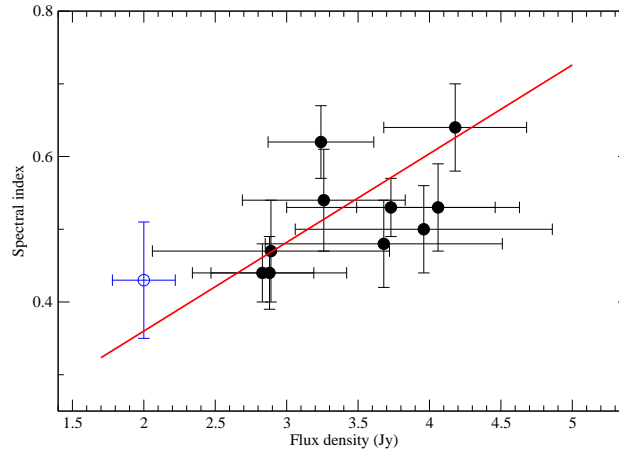
Figure 4.5: Spectral index α (defined as $S_\nu \propto \nu^\alpha$) as a function of flux density at 86 GHz (filled circles). The lower-leftmost point (open circle) is calculated from Falcke et al. (1998). The solid line denotes the best linear fit. See text for details.

A correlation between spectral index and flux density at 86 GHz is strongly in favor of source intrinsic flux density variability, similar to what is seen in AGNs, where the (radio) spectrum hardens when the source is flaring. It seems very unlikely that interstellar scattering effects can account for this correlation (Herrnstein et al. 2004). The fast flux variability of the source, the high brightness temperature, and the correlation of the spectral index with the total source flux supports the idea of a non-thermal synchrotron self-absorbed emission process with a spectral turnover frequency ν_m at or above 86 GHz (Eckart et al. 2008c).

We are convinced that the observed variations of the total flux density in Sgr A* are intrinsic to the source because of several reasons:

1. The variations are larger than the typical variations seen in the nearby calibrators and are not correlated between different sources.

---

[10]The original flux density measurement was performed at 95 GHz and was scaled by us to 86 GHz, adopting a mean spectral index of 0.52

2. The variations are not systematic, nor can they be related to time of bad weather (high opacity), high system temperature or residual uncorrected gain-elevation effects.

3. The variations of the total VLBI flux density correlate well with similar variations of the total flux density seen between 90–230 GHz at three other telescopes (Kunneriath et al. 2010).

4. During the first 5 days, the total VLBI fluxes vary at all 3 frequencies in a similar way, being however more pronounced at the higher frequencies.

5. The rapid flux variations almost vanish during the last 4 VLBI runs (May 21–24), demonstrating the internal consistency and repeatability of the overall flux density calibration of the individual VLBI experiments.

4.2.3 Source Size Measurements and Its Possible Variability

At 22, 43 and 86 GHz, the calibrated visibilities can be very well fitted by a single elliptical Gaussian component. On May 16, and May 19, the elliptical fit to the 86 GHz data diverged. In these two experiments we fitted a circular Gaussian, and used the measured size for the size along the major axis. In Figure 4.6 we plot the variability of major, minor axis and position angle for the 10 individual VLBI experiments versus time. The top panel of the Figure shows the major axis, the middle panel the size of the minor axis, and the bottom panel the orientation (position angle) of the major axis. The different symbols denote the three different observing frequencies. In Table 8.2 we summarize the results of the Gaussian model fitting. The observed mean values for sizes and position angles are also consistent with previous size measurements, which used closure amplitudes in a different way (Bower et al. 2004; Shen et al. 2005).

The weighted mean and standard deviation of the average source parameters are summarized in Table 4.2. The size of the major axis formally varies by (rms/mean) of $m = 0.7$ % at 22 GHz, 1.8 % at 43 GHz, and 10.8 % at 86 GHz. Correspondingly the minor axis changes by 6.5 % at 22 GHz, 11.3 % at 43 GHz, and 18.4 % at 86 GHz. The position angles at the three frequencies are all consistent with an east-west oriented source structure aligned along a position angle of $\sim 80.4 \pm 0.9°$ (see Table 4.4).

For the major axis, our data formally show no variability at 22 and 43 GHz. A χ^2 test gives 79.5 % probability that the major axis at 22 GHz is constant. At 43 GHz we obtained a 11.9 % probability for a constant size. However, at 86 GHz we detect some marginal variability with 0.09 % probability for constant value of the major axis (with

53
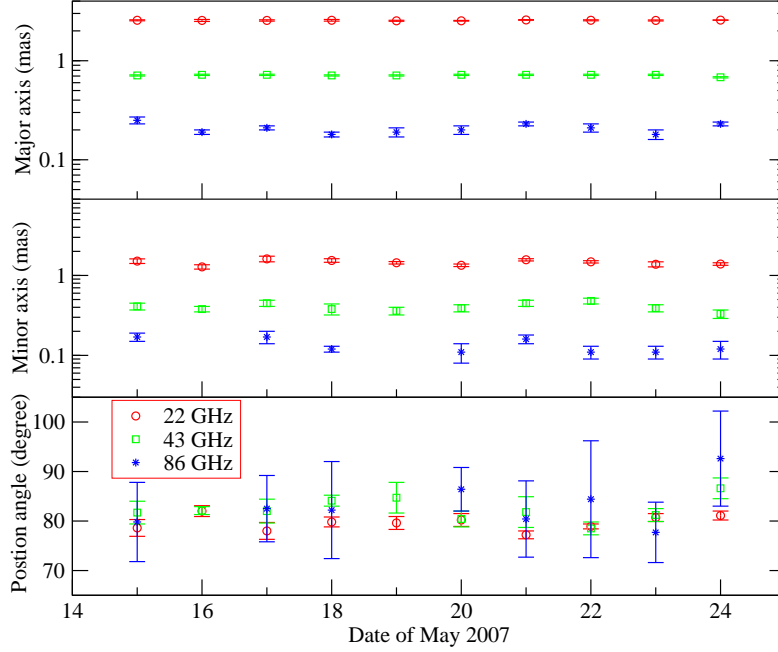
Figure 4.6: Measured apparent structure of Sgr A* at 22 (circle), 43 (square), and 86 GHz (diamond) between 15 and 24, May 2007. The source structure can be well described by a single and, in most cases, elliptically shaped Gaussian component, i.e., the major axis (top panel), the minor axis (middle panel), and the position angle of the major axis (bottom panel). Note that on May 16 and 19 of May 2007, the data at 86 GHz do not allow a model more complex than a circular Gaussian. And thus, no minor axis and position angle is available.

$m \sim 11\%$). For comparison, we also measured the size of the VLBI core component of NRAO 530 at 86 GHz. Owing to the less dense *uv* coverage and a more complex (core-jet) source structure, a fit of a single circular Gaussian component yields slightly larger variations of $m \sim 17.9\%$, which has to be corrected by a factor of $\sim \sqrt{\frac{N_{\mathrm{scan}}(SgrA*)}{N_{\mathrm{scan}}(NRAO530)}} \approx 2$. The corrected fractional rms variation is slightly smaller than the value obtained for Sgr A*, and is an upper limit to the systematic errors in the repeatability of the size measurements for Sgr A*, which then would be less than 9%.

We therefore conclude that within the accuracy of our measurements, we did not detect significant variations in the source size of the source structure at 22 and 43 GHz. At 86 GHz, however, the situation is less clear. The lower SNR of the visibilities, the larger uncertainties of the amplitude calibration, being more strongly affected by low source elevation and higher and variable atmospheric opacities make it difficult to judge the significance of the larger scatter seen at this frequency.

The existence of flux variability at millimeter wavelengths naturally leads to the

Table 4.4: Structure variability characteristics of Sgr A*.

ν	Major axis			Minor axis			P.A.		
	m	χ^2_ν	p	m	χ^2_ν	p	m	χ^2_ν	p
[GHz]	[%]		[%]	[%]		[%]	[%]		[%]
22.2	0.7	0.6	79.5	6.5	2.3	1.5	1.8	2.4	1.0
43.1	1.8	1.6	11.9	11.3	1.3	21.8	2.5	2.0	3.7
86.2	10.8	3.1	0.9	18.4	1.6	11.5	5.2	0.4	91.6

Note: Listed are the observing frequency in [GHz], the modulation index, reduced χ^2_ν, probability for the observable being constant for the major axis, minor axis, and position angle of the major axis, respectively.

question of whether or not flux density variations are associated with changes of size. As we have already noticed, the light curves (Figure 4.3) show strong variability at all three frequencies. We now show in Figure 4.7 the measured source size vs. flux density at each frequency, along with a linear fit. For the major axis size versus flux relation at 86 GHz, the Spearman rank correlation coefficient, r_S, is 0.59. The probability of getting this by chance is less than 10 %, giving strong evidence for a correlation. For the minor axis, a similar behavior is visible at all three frequencies. At 22 GHz, there is 3 % probability for random data leading to r_S of 0.72. The probability at 43 GHz for the correlation arising by chance is 5 % for $r_S = 0.64$. At 86 GHz, r_S is 0.54, with 16 % probability rejecting the non-correlation hypothesis.

The correlated variations of source size and flux density seen at 86 GHz, and even lower frequencies along the minor axis suggest that they may be source intrinsic. The correlation seen along the minor axis could not be attributed simply to sparse *uv* coverage along the north-south because it is roughly the same across the epochs at each frequency. In addition, we note that for interstellar scattering the minimum time scale for the scattered size to change is roughly 10 months at 22 GHz, 3 months at 43 GHz, and 3 weeks at 86 GHz (Bower et al. 2004). These time scales are all larger than the duration of our 10-day observing campaign. Thus the observed variations of the size of the minor axis could be interpreted as a consequence of a blending effect between interstellar scattering and source intrinsic size variation.

For the position angle, we obtained 1.0 %, 3.7 % and 91.6 % probability for the source to be constant at 22, 43, and 86 GHz from a formal χ^2 test (Table 4.4). In Figure 4.8 we plot the position angle of the major axis versus flux density for our 10 days data. Because of the inverted spectrum at our observing frequencies, the data concentrate into 3 distinct groups. The weighted average for each frequency is also shown
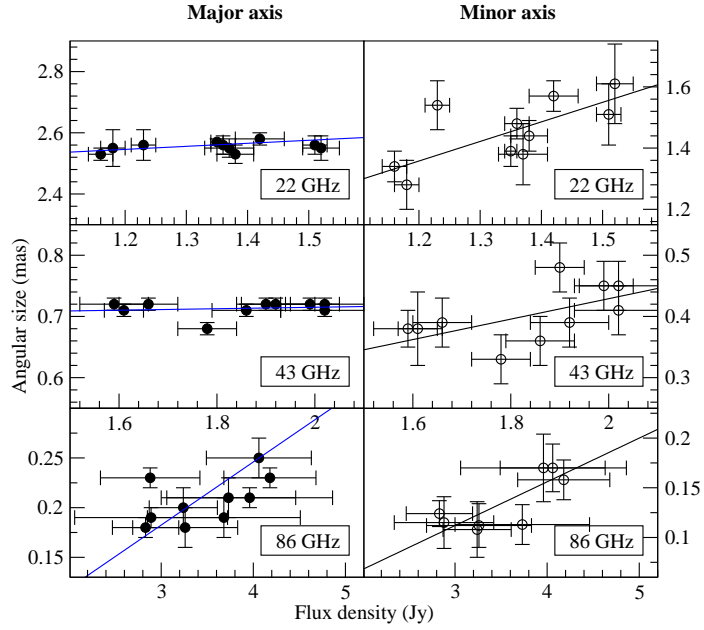
Figure 4.7: Measured angular size as a function of flux density at 22 (top), 43 (middle), and 86 GHz (bottom). Both the major axis (left) and minor axis (right) sizes are shown. The solid lines delineate the best linear fit.

by a red filled circle. Compared with the average position angle obtained from literature data taken at lower frequencies ($< 22\,$GHz), the position angles show a tendency to increase towards higher frequencies (and because of the inverted spectrum towards higher flux densities). The change of position angle appears more significant ($\sim 4.2\,\sigma$, see Table 4.2) between 22 and 43 GHz, where the internal scatter of the data is lower than at 86 GHz. A possible interpretation of this increase is that the source intrinsic structure of Sgr A* begins to dominate over the scattering at these high frequencies.

4.2.4 Variations of the Source Size

4.2.4.1 Time Dependence

Recently, it was claimed (Bower et al. 2004; Shen 2006; Krichbaum et al. 2006) that Sgr A* shows variations in its size. Bower et al. (2004) claim an increase in its intrinsic size of $\sim 60\,\%$ in 2001 at 43 GHz. Shen (2006) reported a size variations at 43 GHz for observations taken in 1999, where an increment of 25 % in its intrinsic size along the major axis has been detected. 86 GHz VLBI observations performed in October 2005 between Effelsberg and IRAM suggest a size increase, which correlates with an increase in total flux density (Krichbaum et al. 2006).
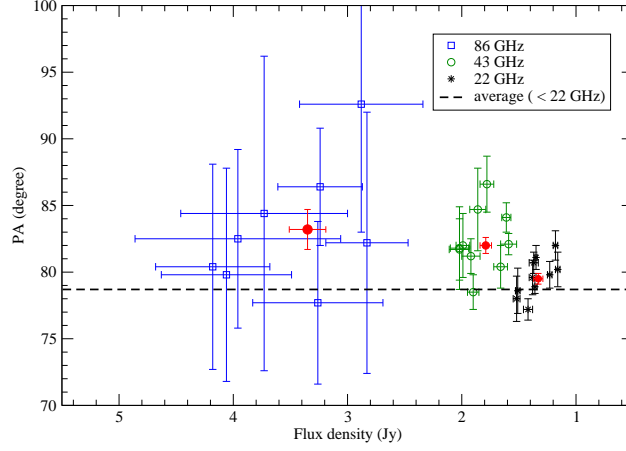
Figure 4.8: Position angle of the major axis of Sgr A* plotted as a function of flux density for our 10-day VLBI observations at 22 (star), 43 (open circle), and 86 GHz (open square). Also shown are average values (filled circles) at each frequency. The dashed line represents the mean position angle (78.8 ± 1.7°) at frequencies lower than 22 GHz, calculated from literature data (i.e., those with position angle available in Figure 4.11 at frequencies < 22 GHz). Notice the inverted order of the abscissa.

To study this further, we plot existing size measurements along the major and minor axes at 43 GHz as shown in Figure 4.9 (top). The mean value of these literature sizes is 0.72 ± 0.01 and 0.40 ± 0.01 mas for major and minor axis, respectively. The variability indices for the major and minor axes are 0.8 % and 8.2 %, consistent with the new data presented here. The corresponding probabilities for being variable are 75 % and 23 %, with reduced χ^2_ν of 17.1 and 9.9 for the major and minor axis, respectively. At the same time, we also show in Figure 4.9 (bottom) the flux density and measured sizes along the major axis at 86 GHz from our data and the data from the literature. The average flux density from the 10 days of VLBA data (3.35 ± 0.16 Jy) is close to the measurement obtained in 2005.79, and is higher than the mean value of all previous data (1.48 ± 0.14 Jy). For the size, the average value from the ten VLBA observations is very close to the average value of all previous data (0.19 ± 0.01 mas). However all these observations suffer from limitations in the data quality (SNR), *uv* coverage, and independent near in time measurements of the total flux density. Therefore it is still difficult to reliably establish a correlation between flux density and source size.

Although our data suggest mild variability of the source size on the 10–20 % level at 43 and 86 GHz, the formal statistical analysis does not unambiguously support significant variability of the size at any of the 3 observing frequencies. This prevents a more thorough correlation analysis between VLBI sizes and the variability of the total
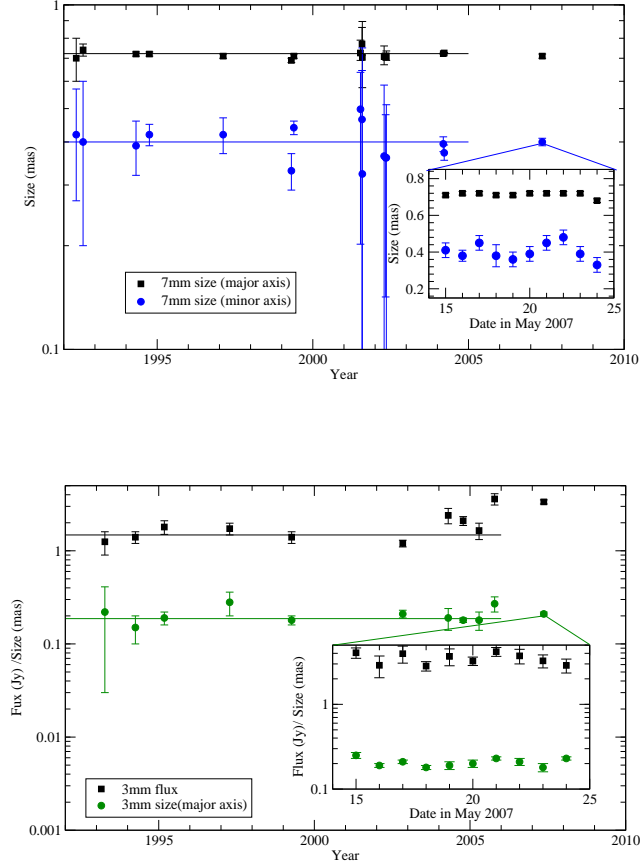
Figure 4.9: Top: The major and minor axis size plotted versus time at 43 GHz. Bottom: Flux density of Sgr A* and measured source size along the major axis plotted versus time at 86 GHz. In each panel, the solid line delineates the average of all previous measurements. The inset shows an enlargement on the data obtained during the 10 days campaign, while others are based on data from literature (as part of those in Figure 4.11).

flux density. However, we note that the amplitude of the observed flux density changes are relatively small, so that possible variations of the source size may become apparent when better data with higher SNR become available in the future, or when a radio flare of considerable larger amplitude will be detected.
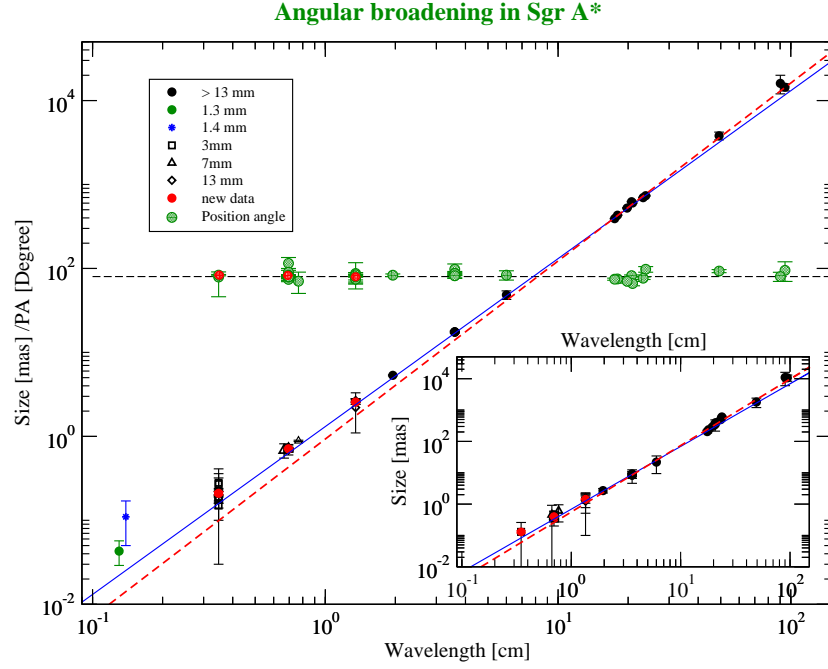
Figure 4.10: Angular size of Sgr A* plot as a function of wavelength for the major and minor (inset) axis. New data are from the observations described in this thesis and literature data are taken from An et al. (2005); Nord et al. (2004); Roy & Pramesh Rao (2003); Davies et al. (1976); Yusef-Zadeh et al. (1994); Bower et al. (2006, 2004); Jauncey et al. (1989); Lo et al. (1985, 1993); Alberdi et al. (1993); Marcaide et al. (1999); Krichbaum et al. (1993); Backer et al. (1993); Shen et al. (2005); Krichbaum et al. (1994); Rogers et al. (1994); Krichbaum et al. (1998b, 2006); Doeleman et al. (2001, 2008). Elliptical source models were preferentially chosen. The dashed lines delineate the scattering law from Bower et al. (2006), i.e., $1.309\lambda_{cm}^2$ mas and $0.64\lambda_{cm}^2$ mas for the major and minor axes, respectively. The solid lines are for a steeper ($\lambda^{2.12}$) law obtained by fitting scattering size at wavelengths longer than 17 cm. The shaded circles indicate the position angle of the major axis.

4.2.4.2 Frequency Dependence

Using our data and data from the literature, we show in Figure 4.10 the major axis size, minor axis size (inset), and the position angle as a function of the wavelength. One can see the apparent source size follows approximately a λ^2 law (blue lines in Figure 4.10). The intrinsic source size normally can be estimated from the measured size by subtracting the scattering size in quadrature (equation 2.2). The scattering deconvolved intrinsic size, therefore, depends tightly on the exact form of the assumed scattering law ($\theta_{scat} = a \times \lambda^\zeta$). Recent revisions of the scattering law have assumed a

λ^2 dependence of the scattering size (Shen et al. 2005; Bower et al. 2006; Falcke et al. 2009).

We show in Figure 4.11 the ratio of the apparent major and minor axis size of Sgr A* to the λ^2-scattering model (blue lines in Figure 4.10) determined by Bower et al. (2006). Due to the poor constrain of the apparent size along the minor axis, it is still hard, at this stage, to find a difference in the broadening effect for the major and minor axis. We notice, however, that both the major and minor axes sizes deviate from this scattering law at longer cm-wavelength. This discrepancy could be due to difficulties in measuring the size in the presence of confusing extended emission around Sgr A* and in the Sgr A complex at long wavelengths. But on the other hand, a power law index steeper than 2 for the λ dependence of the scattering size could also resolve this discrepancy completely. If this was the case, the intrinsic structure would begin to shine through already at somewhat longer wavelengths than currently estimated (starting from 3.6 cm, Bower et al. 2006). A power law fit to the major axis size at wavelengths longer than 17 cm yields for the wavelength dependence of the size the following power-law:

$$\theta_{\text{meas}} = (0.93 \pm 0.32)\lambda_{\text{cm}}^{2.12 \pm 0.12}\text{mas}. \tag{4.2}$$

For the minor axis, the sizes are less well determined. A direct power law fit, which leaves both the index and coefficient unconstrained, does not yield a reasonable result. We therefore assume the same power index for the minor axis as for the major axis. With this fixed power law index, we determine a normalization constant of 0.56 ± 0.03 for the minor axis. Figure 4.12 shows the apparent size normalized by this scattering law. In comparison to Figure 4.11, a systematic overshooting of the data over the model above 10 cm wavelength is avoided.

The angular broadening of the size of Sgr A* is caused by the electron density fluctuations in the interstellar medium. The wavenumber (k) power spectrum of the density fluctuations usually is written in the form of a power law $\propto k^\beta$ with cutoffs at the largest ("outer scale", on which the fluctuations occur) and smallest ("inner scale", on which the fluctuations dissipate) spatial scales and power law index β. The λ dependence of the scattering size follows $\theta_{\text{scat}} \propto \lambda^{\frac{\beta}{\beta-2}}$, namely, $\zeta = \frac{\beta}{\beta-2}$ (Lo et al. 1998, and references therein). The angular broadening scales as $\lambda^{2.2}$ if the electron density spectrum is a power law with a Kolmogorov spectral index, $\beta = \frac{11}{3}$. When the VLBI baseline length becomes comparable to the inner scale, the scattering law changes and has the following form: $\theta_{\text{scat}} \propto \lambda^2$ (e.g., Lazio 2004).

The power law index of $\zeta = 2.12 \pm 0.12$ determined at longer wavelengths (see above) corresponds to $\beta = 3.8 \pm 0.2$, which is close to the Kolmogorov value of 3.67.
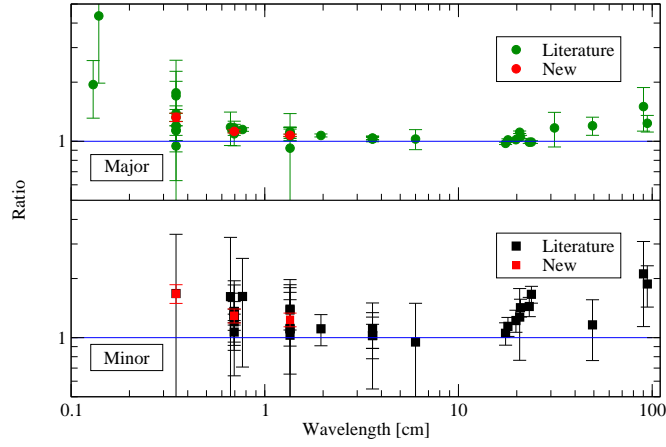
Figure 4.11: The ratio between the apparent size of Sgr A* and the scattering size plotted as a function of wavelength for the major and minor axis. The scattering size is derived from the best fit of the scattering law in Bower et al. (2006), i.e., $(1.309^{+0.015}_{-0.015})\lambda^2_{cm}$ mas and $(0.64^{+0.04}_{-0.05})\lambda^2_{cm}$ mas for the major and minor axes, respectively. Data are from An et al. (2005); Nord et al. (2004); Roy & Pramesh Rao (2003); Davies et al. (1976); Yusef-Zadeh et al. (1994); Bower et al. (2006, 2004); Jauncey et al. (1989); Lo et al. (1985, 1993); Alberdi et al. (1993); Marcaide et al. (1999); Krichbaum et al. (1993); Backer et al. (1993); Shen et al. (2005); Krichbaum et al. (1994); Rogers et al. (1994); Krichbaum et al. (1998c, 2006); Doeleman et al. (2001, 2008).
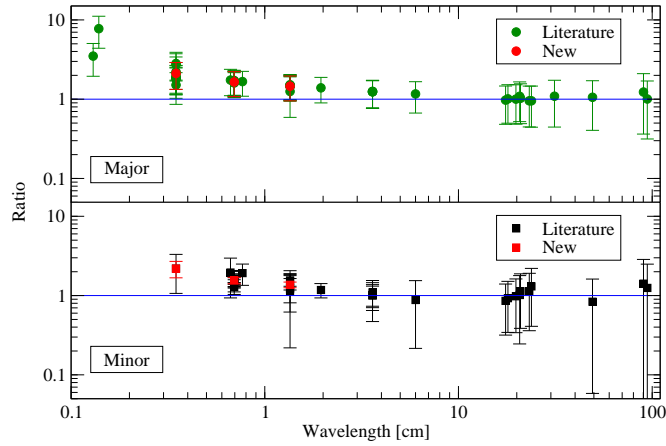
Figure 4.12: Similar to Figure 4.11 except that the scattering size is derived from a slightly steeper power law of $(0.93 \pm 0.32)\lambda^{2.12\pm0.12}_{cm}$ mas for the major axis and $(0.56 \pm 0.03)\lambda^{2.12\pm0.12}_{cm}$ mas for the minor axis, respectively.

On the other hand, this could also be consistent with a broken power law if we stick to a λ^2 scattering law at intermediate wavelengths (cf. Figure 4.11) as it is claimed in

the literature. As Wilkinson et al. (1994) pointed out, the wavelength dependence of the scattering size can have a break, depending on the size of the inner scale for the scattering medium (see also Lazio & Fey 2001). Towards B1849+005, Lazio (2004) found a break in β (his α) between 0.33 and 5 GHz with $\beta = 3.68$ (i.e., $\zeta = 2.19$) at 0.33 GHz and $\beta > 3.8$ (i.e., $\zeta < 2.11$) above 5 GHz. He interpreted this break as the detection of the inner scale on a scale of a few hundred kilometers. In other words, such a break indicates the existence of an inner scale within the covered range of baselines from a few ten (VLA) to thousand (VLBA) kilometers in their observations. Figure 4.12 indicates that if we fit the scattering size also at longer wavelength, we find $\zeta > 2$. If mainly data between 2 and 24 cm, are used, ζ would be close to 2.

4.2.5 Intrinsic Source Size

On the basis of the currently available VLBI data for the major axis, we fitted a power law ($\sim \lambda^\kappa$) to the intrinsic source size from 13 to 1.3 mm (Figure 4.13, left). The intrinsic sizes were derived using the scattering model from Bower et al. (2006) and equation 2.2. For the intrinsic size, we obtain a power law index of $\kappa = 1.34 \pm 0.01$. This is in agreement with the intrinsic size used by Falcke et al. (2009), who give 1.3 ± 0.1. As a check of consistency, we also show the wavelength dependence of the intrinsic size for the minor axis in Figure 4.13 (lower panels). Similarly, we obtained $\kappa = 1.30 \pm 0.06$ for the minor axis, indicating the same λ dependence as for the major axis within errors. Shown in Figure 4.13 (right) is the intrinsic size derived from the steeper scattering law (equation 4.2), which fits better the wavelength dependence of all size measurements. This leads to a steeper λ dependence of the intrinsic size, with $\kappa = 1.5$ and 1.4 for the major and minor axis size, respectively.

The spatial distribution of the emission provides the most important constrains on theoretical models. A detailed inhomogeneous jet model predicts $\kappa \sim 1$ (Falcke & Markoff 2000). However, the dependence of the magnetic field strength, electron number density and energy density on the distance to the jet origin may change and relax the constrains on κ. Interestingly, VLBI observations of M 81* revealed that the length of the jet also shows a similar frequency dependence ($\lambda^{0.8}$) (Bietenholz et al. 1996, 2004). Based on the radiatively inefficient accretion flow (RIAF) model (Yuan et al. 2003), Yuan et al. (2006) reproduced sizes which are consistent with a $\lambda^{\sim 1}$ scaling. Liu et al. (2004) showed that acceleration of electrons by plasma wave turbulence in hot gas near the event horizon and subsequent diffusion of high energy electrons to spatially large scales (outflow), can in principle explain the size-wavelength dependence.
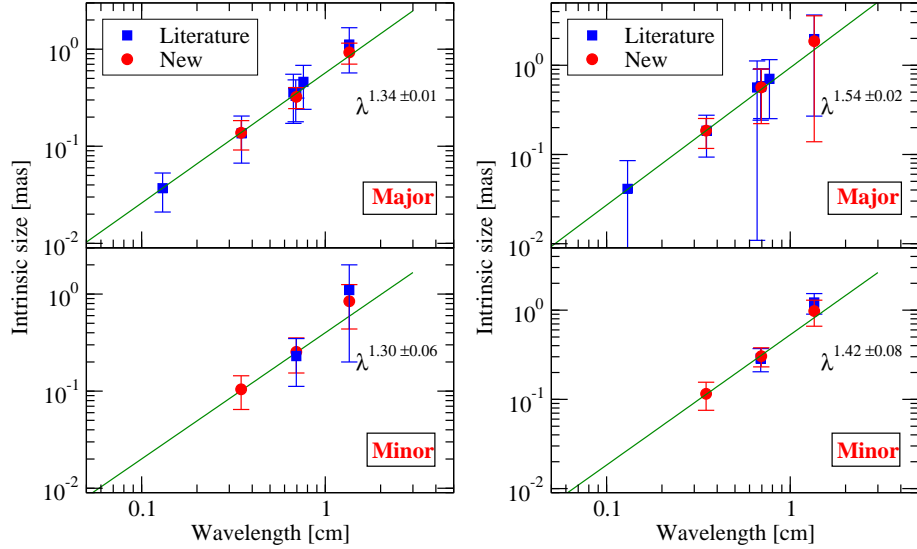
Figure 4.13: Wavelength dependence of the source intrinsic size for the major axis and minor axis. Left: Intrinsic size deconvolved with the λ^2 law from Bower et al. (2006). Right: The intrinsic size is derived from the steeper scattering law as used in Figure 4.12. Literature data are taken from Bower et al. (2004); Shen et al. (2005); Bower et al. (2006); Doeleman et al. (2008).

4.2.6 Closure Quantities

4.2.6.1 Closure Phase

Although still under debate, a periodicity in NIR and X-ray flares has been claimed by several authors (e.g., Genzel et al. 2003; Aschenbach et al. 2004; Eckart et al. 2006a). The orbiting spot model is very successful in describing these flare properties and their propagation through the spectrum. Supposing that part of the emission comes from material orbiting around the SMBH, short-timescale asymmetric structures would be expected (Broderick & Loeb 2006). Thus, quasi-periodic deviations of the closure phase from zero could be expected on similar time scales, if the interferometer provides a high enough angular resolution (Fish et al. 2008). The closure phase, the sum of three baseline phases in a closed triangle of stations, is a phase quantity of the complex visibilities that is independent of all antenna-based phase errors. The closure phase for any point-symmetric brightness distribution must be zero. In the context of the hot spot model, the degree and time scale of a deviation of the closure phase from zero is a function of the diameter of the hot spot orbit and the flux ratio between emission from the accretion disk and the hot spot embedded in it.

Through phase-referenced VLBI monitoring observations of the Sgr A* centroid position against stationary back-ground quasars, Reid et al. (2008) ruled out hot spots with orbital periods exceeding 120 minutes to be contributing > 30 % of the total 7 mm flux density. Structural variations at smaller radii or fainter hot spots however remain unconstrained.

In an idealized and simplistic orbiting hot spot scenario, in which the hot spot remains visible for several orbiting periods, periodic non-zero deviations of the closure phase could be expected during the time of a VLBI track. This might be directly observable with future mm/sub-mm VLBI arrays (Doeleman et al. 2009b). In this context, it could be useful, as a first step, to search for deviations of the closure phase from zero in the VLBI data presented here. Owing to the smaller beam size and lower source-intrinsic opacity, such variations would be more prominent and easier to detect at higher frequencies. We therefore use the closure phases at 86 GHz for a more detailed analysis. We extracted the closure phases from 10-second averaged *uv* data for several representative station triangles, flagging discrepant phase data points before, and then coherently averaging the closure phases to the full scan length of about 4 minutes. Figure 4.14 shows two typical examples of the closure phase.
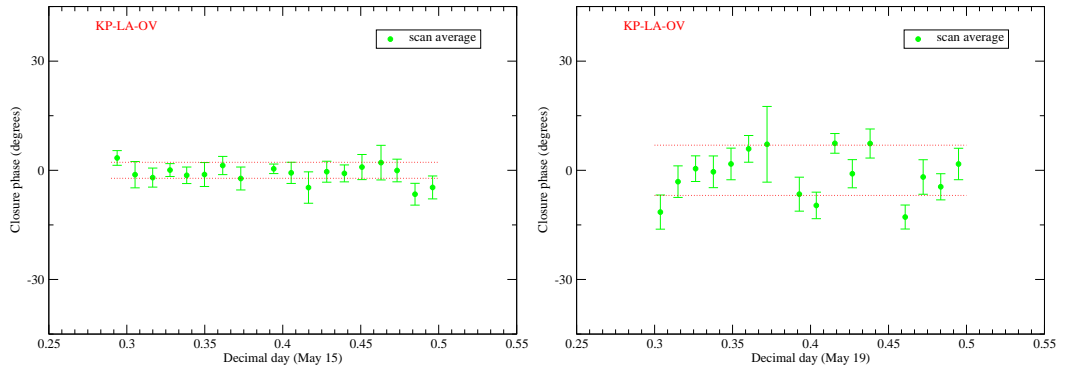
Figure 4.14: Plot of a typical closure phase as function of time for the KP-LA-OV triangle from the 86 GHz experiment on May 15 (left) and 19 (right), 2007. Dotted lines indicate 1 σ range for the closure phase averaged over a whole experiment.

Within a single VLBI run, the χ^2-tests show that the closure phase for most studied triangles remains constant with a high probability. For several cases where we saw low probability (i.e. evidence for variability), a visual inspection of the data revealed a higher level of phase noise. Therefore we conclude that the closure phases do not vary on a scan by scan basis and within a single VLBI run for our data.

We finally averaged the closure phases in time and over all the studied triangles for each epoch, to obtain characteristic closure phase values for each triangle and given

day. In Table 4.5 we summarize the results of this averaging for some representative baseline triangles of the VLBA at 86 GHz. For each individual triangle and observing epoch, the average closure phase is zero within errors for all studied cases, suggesting that the source structure is indeed point like and not variable within a given day and on time scale of days. At 22, and 43 GHz, the closure phases show smaller scatter and are all consistent with zero within the errors. We find no evidence for the closure phase deviating from zero and being variable. The stationarity of the closure phase can be understood in terms of the large VLBI observing beam size. At the highest frequency of 86 GHz in our observations, the beam size of ~ 0.3 mas is a factor of ~ 5–10 larger than the expected size of the last stable orbit (1 Schwarzschild radius corresponds to about 0.01 mas).

One of the main limitations of our analysis is the sensitivity at 86 GHz, at which any non-zero and variable closure phases would be easier to detect than at 22 and 43 GHz. Future analysis with improved sensitivity, like the VLBA at data recording rate of 4 Gbps, would be a logical further step. Additionally, since the source is heavily resolved on the VLBA long baselines, experiments at even higher frequencies (230, 345 GHz) are the only way to improve the resolution for Sgr A* and therefore bear the potential of detecting flaring structures (Doeleman et al. 2009b).

Table 4.5: Averaged closure phases for some representative triangles at 86 GHz. We use the standard deviation as error for the mean. The three lines at the bottom of the table summarize the mean closure phase over all observing epochs, the reduced χ^2_ν, and the probability for being variable. The last three columns contain the mean closure phase for a given epoch, the reduced χ^2_ν, and the probability for being variable.

Date	KP-LA-OV	FD-LA-PT	FD-LA-OV	FD-KP-PT	LA-OV-PT	FD-KP-OV	mean	χ^2_ν	Probability (%)
15 May, 2007	−0.5±2.2	...	...	...	−1.2 ± 3.1	...	...	...	...
16	−1.8 ± 4.5	−3.2 ± 5.9	−0.5 ± 7.8	−1.4 ± 6.9	0.0±8.2	2.2±7.0	−1.2 ± 0.7	0.08	0.5
17	4.2±7.0	−1.1 ± 6.0	1.3±12.4	−0.2 ± 4.6	1.4±3.6	−5.4 ± 10.0	0.6±0.9	0.16	2.2
18	−1.4 ± 4.0	2.0±5.3	−2.1 ± 4.2	0.7±6.8	−2.7 ± 5.6	3.4±9.6	−0.8 ± 0.8	0.15	2.0
19	−1.2 ± 6.9	1.9±4.8	2.8±7.3	2.8±4.7	−2.9 ± 4.5	3.7±6.6	0.9±1.1	0.25	6.1
20	2.6±4.9	1.1±1.6	−2.2 ± 4.7	−0.2 ± 4.0	−1.3 ± 3.5	−4.2 ± 8.5	0.4±0.6	0.25	6.0
21	4.1±6.5	−0.5 ± 2.8	−5.4 ± 8.1	0.4±4.8	−0.5 ± 5.0	1.0±5.2	−0.1 ± 0.8	0.19	3.2
22	0.2±3.2	0.9±2.0	0.2±5.6	−0.4 ± 3.3	−1.3 ± 4.3	−0.7 ± 4.2	0.2±0.3	0.06	0.3
23	0.7±5.3	0.5±3.4	3.6±4.0	1.8±5.8	1.8±4.9	1.8±6.9	1.7±0.5	0.08	0.4
24	...	−1.1 ± 3.2	...	−1.1 ± 4.1	...	...	...	...	...
mean	0.0±0.6	0.5±0.4	−0.1 ± 1.0	0.1 ± 0.4	−0.7 ± 0.5	0.5±0.9			
χ^2_ν	0.18	0.15	0.27	0.07	0.13	1.2			
Probability(%)	0.6	0.3	3.4	0.02	0.2	0.8			

4.2.6.2 Closure Amplitude

Similarly to the closure phase, the closure amplitude is an observable free of antenna-based errors. To obtain closure amplitudes, we performed, for each scan, an incoherent average for the 10-second (coherently) averaged visibility amplitude, during which a noise bias was corrected (see, e.g., Thompson et al. 2001; Shen et al. 2003, for details). Closure amplitudes were then formed for the incoherently averaged amplitudes. Only independent closure amplitudes are formed. In the case of low SNR of involved visibilities, Trotter et al. (1998) showed that it becomes difficult to determine closure amplitude bias and the formal errors. We therefore limit ourselves to high SNR visibilities with a SNR cutoff of 5. We fitted the closure amplitudes with a single elliptical Gaussian component via a thorough search of the 3-dimensional parameter space (angular size along the major and minor axis, and P.A. of the major axis). In Figure 4.15 we show the Gaussian model fitting to the closure amplitudes at 43 GHz for the epoch on May 16, 2007. For the source structure we obtained the following parameters: $\theta_{\mathrm{major}} = 0.70^{+0.01}_{-0.01}$ mas, $\theta_{\mathrm{minor}} = 0.37^{+0.06}_{-0.07}$ mas, and P.A. $= 82.6^{+3.0}_{-3.2}$ degree with a $\chi^2_\nu = 1.74$. The errors are at 3σ level and are derived from the projection of the χ^2 confidence contours onto the parameter axis for the case of 3 parameters (Bevington & Robinson 2003, section 11.5). This result is in good agreement with what we obtained through modeling of the self-calibrated visibilities and demonstrates the equivalence of self-calibration and modeling of closure quantities (Cornwell 1995). For the fitting, we ignored visibilities whose radial distance in the uv plane exceeds 250 $M\lambda$. This uv distance limit removes most of the low SNR data which could bias the closure amplitudes. At 22 and 43 GHz, we find this procedure to be quite successful in modeling the source structure of Sgr A*. At 86 GHz, however, a direct fitting of the closure amplitudes does not converge. We notice that the closure amplitudes are formed mainly on the basis of the inner 5 VLBA antennas (FD, KP, LA, OV, PT), and in this case only 5 independent closure amplitudes are available. Furthermore, the large scatter of the data indicates that a single Gaussian component is only a first order approximation. As an example we show the FD-KP-LA-PT quadrangle at 86 GHz for the three experiments on May 19, 20, and 21, 2007 along with the average source structure model (Table 4.2) in Figure 4.16. Reduced chi-square (χ^2_ν) values of 3.3 (May 19), 3.8 (May 20), 4.1 (May 21) indicate a poor fit of a single Gaussian model.
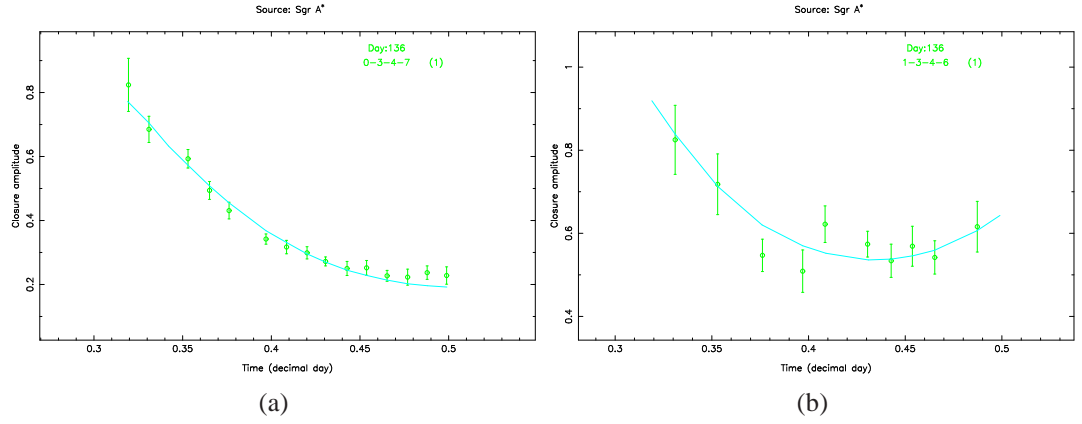
Figure 4.15: Closure amplitudes of two quadrilaterals (Left: BR-KP-LA-OV; Right: FD-KP-LA-NL) at 43 GHz for the observations on May 16, 2007. The solid line delineates a best-fit singe Gaussian model, i.e., $\theta_{major} = 0.70$ mas, $\theta_{minor} = 0.37$ mas, and P.A. = 82.6°.
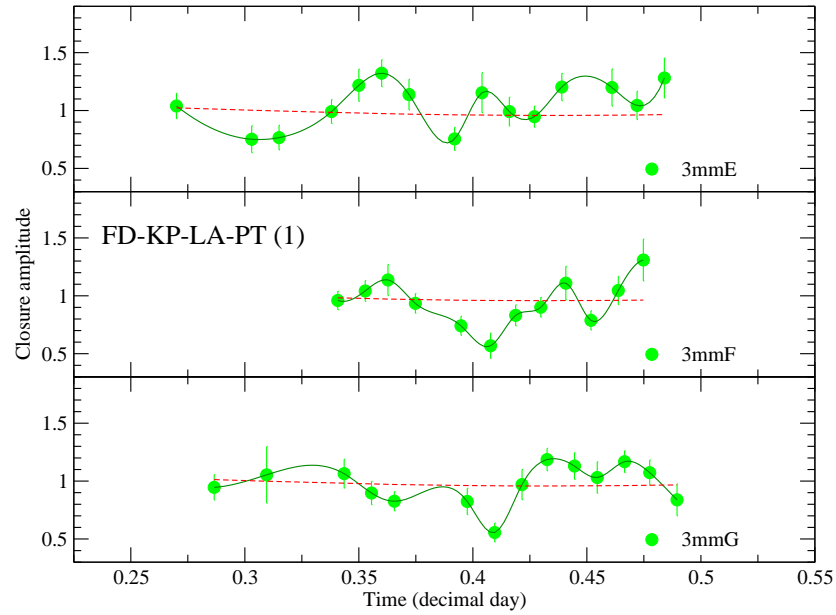
Figure 4.16: Closure amplitudes for the FD, KP, LA, and PT quadrangle of the VLBA antennas on 3 consecutive days (May 19, 20, 21, 2007, from top to bottom). The abscissa is UT in decimal day on May 19, and for the two subsequent epochs, a 4-minute backward shift is applied in order. Spline interpolations are shown as solid lines and the dashed lines are for a source model with $\theta_{major} = 0.21$ mas, $\theta_{minor} = 0.13$ mas, and P.A. = 83.2° (see also Table 4.2).

4.2.7 Variability of VLBI Source Flux and NIR Variability

Our understanding of the relation between the variability characteristics at radio and sub-millimeter wavelengths to the variability at NIR and X-ray wavelengths has improved. Early evidence for the existence of a broad-band relation comes from correlated flare activities of Sgr A* in the radio and X-ray bands (Zhao et al. 2004). Recently, Eckart et al. (2008c) and Yusef-Zadeh et al. (2009) detected simultaneous flare emission in the near-infrared and sub-millimeter domains. Eckart et al. (2008c) showed that a strong flare activity in the 0.87 mm (345 GHz) sub-mm wavelength band took place, following a NIR flare with a delay of 1.5 ± 0.5 hours. Generally, the flares seen in the NIR and X-ray regime (NIR and X-ray flares appear to happen almost synchronously, see, e.g., Eckart et al. 2008b) are thought to be related to flares in the mm/sub-mm regime with a reported delay of ~ 100 minutes of the low energy emission (Meyer et al. 2008; Marrone et al. 2008; Yusef-Zadeh et al. 2008). At radio wavelengths, Yusef-Zadeh et al. (2006a) showed that the time delay between 22 and 43 GHz peak emission is of the order of ~ 20–40 minutes.
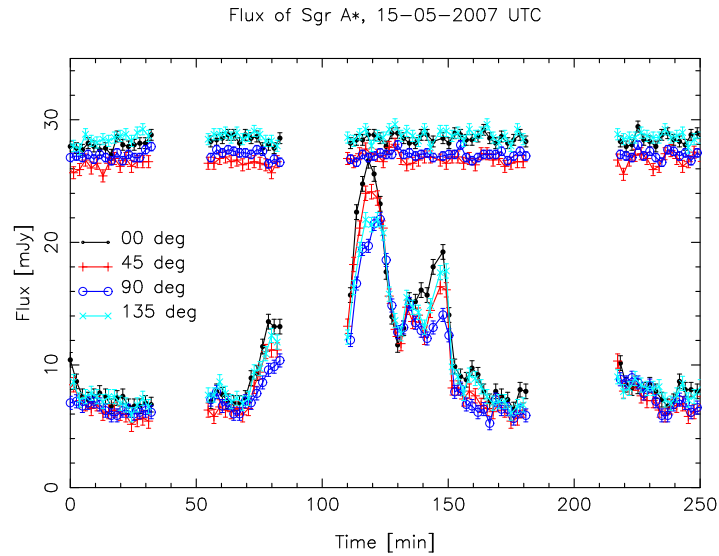
Figure 4.17: NIR (K-band) light curve of the May 15, 2007 flare. Different colors denote different channels. A star, S2 is also shown for comparison and shifted by a few mJy for clarity. See Eckart et al. (2008b) for details.

In Figure 4.18 we show the combined light curve from the May 2007 campaign. It can be seen that the combined light curve from CARMA/ATCA/IRAM-30 m show the same trend as the VLBA data. The NIR observations of Sgr A* on May 15, 2007 started at UT 5^h29^m and lasted for 250 minutes. During that time, a NIR flare occurred

at ~ UT 6^h40^m with two sub-flares centered at about UT 7^h30^m and UT 7^h50^m (Eckart et al. 2008b). The VLBI observations started between UT 6^h10–6^h20^m at the three frequencies, and lasted for 6 hours. Therefore, the VLBI observations covered ~ 4.3 hours (UT 7^h50^m–UT 12^h10^m) after the peak time of the NIR flares. During this time we did not detect any significant change in the visibilities. Under the assumption that the flare emission in the NIR leads to a change in size at millimeter wavelengths, we can use this 4.3-hour interval as an upper limit to constrain the expansion speed for a putative expanding plasmon. With a beam size of 0.34 mas (0.1 mas $\simeq$ 1 AU) at 86 GHz, the expansion speed would be limited to < 0.1 c. In other words, any significant change of the source structure with speed larger than this limit would have been detected.
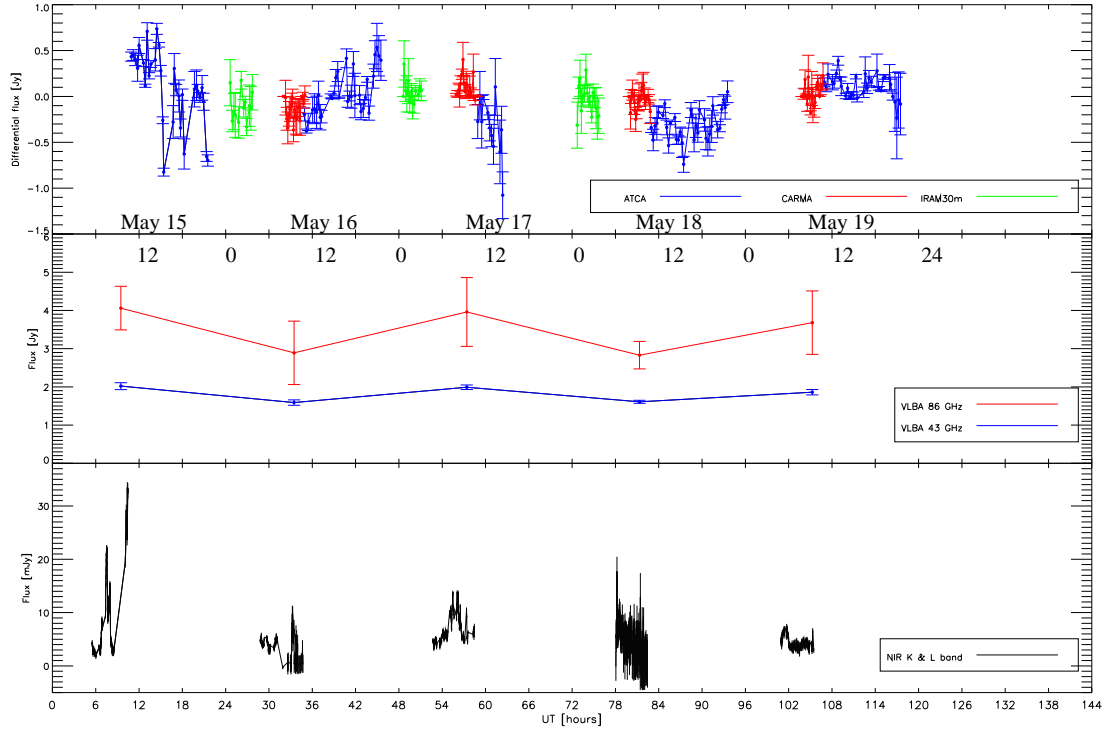
Figure 4.18: Combined light curve of Sgr A* from the May 2007 campaign. Upper panel: combined differential light curve of Sgr A* in the mm/sub-mm domain obtained with the ATCA (86 GHz), CARMA (100 GHz), and IRAM 30m-telescope (250 GHz). Middle panel: flux density of Sgr A* measured with VLBA at 43 and 86 GHz for the first five epochs (Table 8.2). Upper panel: the combined light curve obtained with the VLT at K-band (2.18 μm) and L'-band (3.8 μm). See Kunneriath et al. (2010) for details.

Modeling of radio, sub-millimeter, and NIR flares yields expansion speed of 0.003–0.1 c (Yusef-Zadeh et al. 2008; Eckart et al. 2008c). This agrees well with the above

expansion velocity, although the accuracy of the derived expansion speed from VLBI is still relatively poor.

4.3 Conclusion

We presented the first multi-epoch multi-frequency high resolution VLBA inter-day monitoring of the compact radio source in the Galactic center. Sgr A* showed flux density variations on daily time scales with higher variability amplitudes observed at higher frequencies. A positive correlation was found between the spectral index and the flux density at 86 GHz (harder spectrum when brighter). The major axis size of Sgr A* appears to be stationary (non-variable) at 22 and 43 GHz. Marginal variations seen at 86 GHz are hidden in measurement uncertainties and need further confirmation. In contrast to this stationarity of the major axis, we find evidence for variability of the minor axis with time and flux density. This time variation of the size of the minor axis points towards a source intrinsic origin, but also needs further confirmation. Our data indicate that the position angle slightly increased towards higher flux and higher frequency. This may suggest that the intrinsic structure becomes visible and begins to dominate over the anisotropic interstellar scattering.

The commonly assumed λ^2 scattering law for the interstellar image broadening underestimates the observed angular size of Sgr A* at longer wavelengths for both, the major axis and minor axis. A steeper power law index of 2.12 ± 0.12 for the λ-dependence of the scattering size can remove this discrepancy. This may suggest that the inner turbulence scale become important, which makes scattering towards the Galactic center similar to several other scatter broadened radio sources. In the case of the steeper scattering law, the critical wavelength at which the intrinsic size begins to dominate over the scattering size would become longer than currently estimated. Consequently, the λ-dependence of the intrinsic size becomes steeper ($\propto \lambda^{1.4-1.5}$).

The analysis of the closure phases at the highest frequency available in this observations (86 GHz) confirmed that the apparent VLBI source structure is indeed symmetric. We did not detect significant variations of the closure phase with time, not on a intra- not on a inter-day time scale. Modeling the closure amplitude at 22 and 43 GHz verified its equivalence to self-calibration. At 86 GHz, the available data, although sparse for a direct fitting, indicate a poor agreement with a single Gaussian component model. This maybe regarded as a signature of more complex than pointlike Gaussian VLBI structure and has to be addressed in future VLBI experiments. The lack of any visible structural variation or component ejection after a NIR flare points to an upper velocity limit of $0.1\,c$ for a putative plasma ejection.

5 The NRAO 530

5.1 Introduction

During our VLBA monitoring program of Sgr A*, NRAO 530 was being observed as a fringe tracer and was used to provide consistency checks for the amplitude calibration of Sgr A*. NRAO 530 was observed shortly before, during, and after the time of visibility of the target source, Sgr A*. Following a brief explanation of the observations and data reduction in section 5.2, in section 5.3 we present the results from these VLBA observations at three high frequencies (22, 43 and 86 GHz). The structure of the inner jet was found to have changed significantly when compared with previous VLBI studies. In order to probe the jet kinematics, we have made use of VLBA data at 2 cm, from the MOJAVE program, which allows us to conduct a detailed study of structural variations with good time coverage. A summary of the results is presented in section 5.4

At a redshift of 0.902 (Junkkarinen 1984), NRAO 530 (also known as 1730-130) is a well known blazar, which is classified as an Optically Violently Variable object. Strong and erratic broadband variability has been observed in the radio (Bower et al. 1997), optical (Webb et al. 1988), and through to the γ-ray regime (Mukherjee et al. 1997). In γ-rays, it was found to be exceptionally bright during the EGRET observations, but recently is relatively quiescent (Abdo et al. 2009). Interestingly, Foschini et al. (2006) serendipitously detected a short hard X-ray flare on 17 February 2004 with the INTEGRAL satellite. The short timescale (< 1 hour) of the flare is considered exceptional for a flat-spectrum radio quasar (FSRQ) and therefore casts some doubts on the association with NRAO 530.

On kpc scales, NRAO 530 exhibits two-sided lobes in the east-west direction. The western lobe is stronger than the eastern one and is connected to the core with weak arch-structured emission (Hong et al. 2008). Centimeter VLBI images showed a core-jet structure on pc scales with an oscillating trajectory extending to the North from the assumed core (e.g., Shen et al. 1997). The morphology of NRAO 530 from pc to kpc scales is shown in Figure 5.1. Space VLBI observations revealed brightness tem-

peratures of NRAO 530 significantly in excess of both, the inverse Compton and the equipartition limit (Bower & Backer 1998). Superluminal motions of several components were detected with the apparent velocities in the range of 10–40 c (Bower et al. 1997; Jorstad et al. 2001; Feng et al. 2006; Hong et al. 2008).
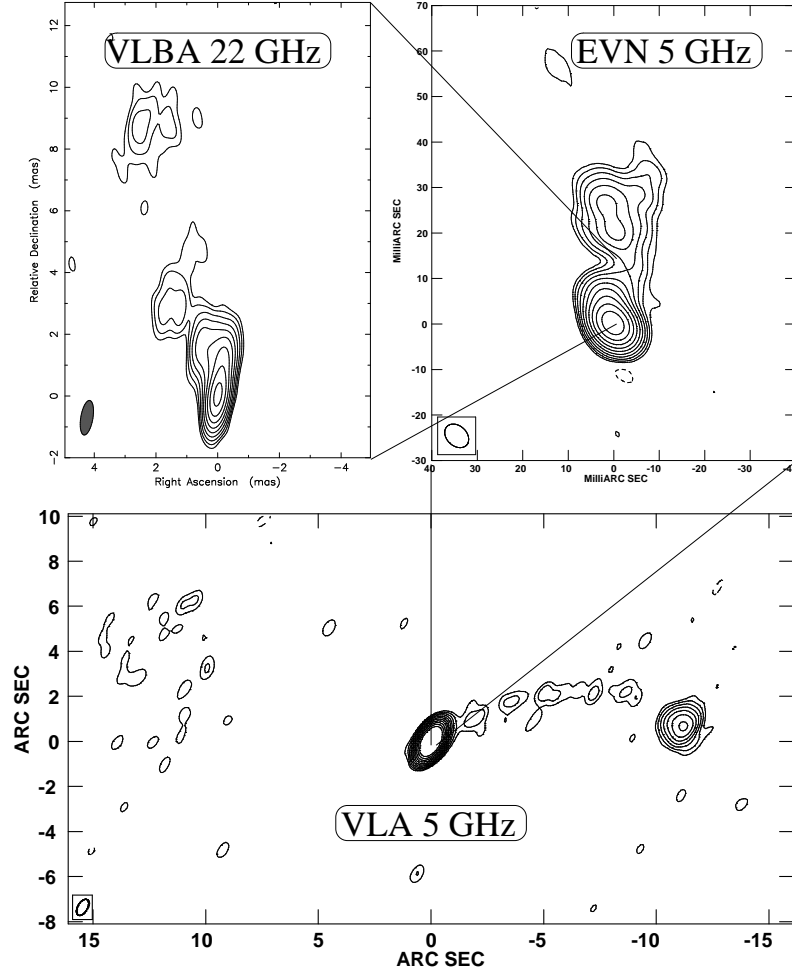
Figure 5.1: Morphology of NRAO 530 from pc to kpc scales. VLBA image at 22 GHz is obtained from observations performed on May 15, 2007 (see section 5.2). VLA and EVN images at 5 GHz are from Hong et al. (2004). At a redshift of $z = 0.902$, 1 mas corresponds to 7.8 pc.

Morphologies of compact radio sources on pc scales are typically characterized by kinks and bends of the jet ridge lines. The curvature is usually more pronounced towards the innermost region of the core (Zensus 1997). NRAO 530 is a typical example in this sense (Figure 9.1).

In many sources, it is well established that individual jet components show appar-

ent superluminal motion, moving outward from the core. Although non-radial, non-ballistic trajectories are not uncommon (e.g., Homan et al. 2009), component speeds in many cases are found to be constant, based only on core separation with time, due to the limitation of the data quality. In a number of sources alternative scenarios exist for the kinematics in the pc-scale jets. In these cases, jet components predominantly move along the direction perpendicular to the jet axis, while radial motion is subluminal (Britzen et al. 2006).

Images of NRAO 530 obtained at 5 GHz in the early 1990s indicated that the position angle of the jet components changed significantly (Hong et al. 1999). Our new images reveal a jet structure for the inner region very different from those previously reported (e.g., in Feng et al. 2006). NRAO 530 has undergone 2 moderate flares (Jenness et al. 2009, Figure 5.2) since the dramatic flare around 1997 (Bower et al. 1997; Feng et al. 2006). This stimulates us to also investigate the pc-scale jet kinematics and its possible relation to the long term radio flux variations in NRAO 530.

Throughout this chapter, we adopt the luminosity distance to NRAO 530 D_L = 5.8 Gpc, 1 mas of angular separation corresponds to 7.8 pc, and a proper motion of 1 mas yr^{-1} corresponds to a speed of β_{app} = 48.5 c (H_0 = 71 km s^{-1} Mpc^{-1}, Ω_M = 0.27, Ω_Λ = 0.73).

5.2 Observations and Data Analysis

During the global campaign on Sgr A* in May 2007 (see Chapter 4), NRAO 530 was monitored as a calibrator by the VLBA from 14th to 24th May 2007 at 22, 43, and 86 GHz every day. The individual VLBI scans had a duration of 3 minutes at 22 GHz and 4 minutes at 43 & 86 GHz respectively. The reduction of the data was performed within the AIPS software in the usual manner (see also Chapter 4). Opacity corrections were introduced at these 3 frequencies by solving for receiver temperature and zenith opacity at each antenna. In addition, we have also used the VLBA observations at 15 GHz from the 2 cm survey and the follow up MOJAVE[11] program between 1999 and 2009, spanning 10 years. These data were provided as automatically self-calibrated *uv* FITS file, which we recalibrated and remapped in *difmap* before model-fitting. The clean images are shown in Figure 9.1 and Figure 9.2 in Appendix C. Table 9.1 summarizes the map parameters.

In all cases of the model fitting, circular Gaussian components have been chosen in order to simplify and unify the comparison. The final fitting of jet components was

---

[11] http://www.physics.purdue.edu/MOJAVE/
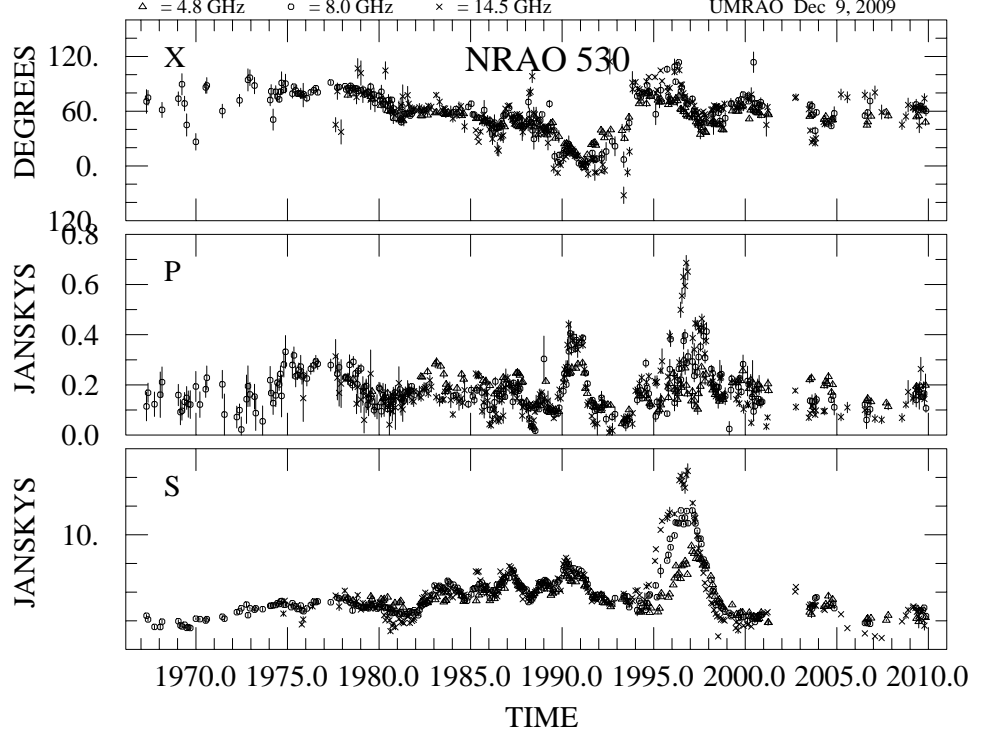
Figure 5.2: Long term monthly averages of the total flux density (bottom), polarized flux (middle), and electric vector position angle (top) in NRAO 530 (taken from Aller et al. 2009).

stopped when no significant improvement of the reduced χ^2_ν values was obtained. The formal errors of the fit parameters were estimated by using the formulae from Fomalont (1999). The position errors were estimated by $\sigma_r = \frac{\sigma_{rms}\, d}{2\, I_{peak}}$, where σ_{rms} is the post-fit rms, and d and I_{peak} are the size and the peak intensity of the component. In case of very compact components, this tends to underestimate the error. We therefore included an additional minimum error according to the map grid size, which roughly matches 1/5 of the beamsize at each frequency and corresponds to 0.06 mas at 15 and 22 GHz, 0.03 mas at 43 GHz, and 0.02 mas at 86 GHz. For the weighted mean of parameters from the 10 consecutive epochs, we have chosen the max ($\sqrt{\frac{1}{\Sigma\frac{1}{\sigma_i^2}}}$, $\frac{\sigma}{\sqrt{N}}$) as the standard error for the few cases when the former is smaller than the latter. By doing so, we have assumed the stationarity of the corresponding parameter on daily time scales.

Our ten-day observations have revealed consistent jet structure at all three frequencies. Cross-identification of jet components is straightforward and therefore without misidentifications. We find no naming convention for the VLBI components in the

75

literature that we could follow for NRAO 530. We therefore labeled the modeled components in an alphabetical order with increasing core separation, starting from the core (*c*) to the outermost jet component (*j*). A very faint feature which faded away after 2002 is labeled as *x*. An inner jet component, which was not resolved at frequencies ≤ 22 GHz in May 2007, is named as *n* and the newly ejected components after 2008 is named as *n'*. The component cross-identification at 15 GHz is based on their flux density, core separation, position angle, and FWHM. We noted that although the archival data at 15 GHz have a good time resolution, large gaps in time sampling, particularly during 2000 and 2002, makes tracing weak jet components very difficult (see section 5.3.3).

5.3   Results and Discussion

Figure 9.1 shows the resulting clean maps at 22, 43, and 86 GHz for the 10 epochs in May 2007. We tabulate in Table 9.2 the epoch of observation, the identification of components, and the fitted parameters and their uncertainties. On 2007 May 15, the sparse *uv* coverage at 86 GHz did not permit us to model source structure more complex than a single Gaussian component, and we will not consider this data set for further analysis.

On VLBI scales, NRAO 530 is characterized by a one-sided jet following a curved trajectory of ~25 mas to the north (e.g., Romney et al. 1984; Bondi et al. 1996). In our analysis, we assume the southernmost component (component *c*) to be the stationary core of the radio emission because it exhibits the flattest spectrum (see section 5.3.1). This is in agreement with the core identification by Jorstad et al. (2001) and Feng et al. (2006).

As can be seen in Figure 9.1, our three-frequency datasets of 2007 revealed very consistent jet morphology within the central ~ 10 mas, with richer structure seen at lower frequencies. The innermost jet component (*n*) detected at 43 and 86 GHz was not seen at 22 GHz, which may be due to the insufficient resolution at this frequency and the relative weakness when compared with adjacent components. The inner jet extends slightly to the north-west direction (P.A. ~ −10°) out to a core separation of ~ 1.5 mas and then bends sharply by ~ 90° towards a P.A. of 25° at a core separation of 3.5 mas. From here, the jet bends gently northward following a curved path with underlying diffuse emission. Finally, it fades away at a core separation of ~ 9 mas with a P.A. of 10°. The jet component (*i*) located at ~25 mas north of the core was not seen at the three high frequencies but was visible at 15 GHz across all the epochs (Table 9.2). This is probably due to the higher resolution at the high frequencies and

the steep spectrum of this jet component.

5.3.1 Component Spectra and Spectral Reversal

In order to study the evolution of the spectra of the VLBI components, we also used 15 GHz data at 2007.44, taken close to our multi-frequency observations in May 2007 (epochs 2007.37–2007.39). The spectra of the components are shown in Figure 5.3 based on the flux densities obtained by model-fitting of Gaussian components to the visibility data. As can be seen in Figure 5.3 (a), component c displays an inverted spectrum and is located at the south end of the source structure (Figure 9.1). The optically thin spectral index for component c is -0.19 ± 0.03 between 43 and 86 GHz, which is the flattest among all the components. Therefore, we identify this component as the compact VLBI core.

To fit the convex spectrum of the core, we use both, the synchrotron self-absorption (SSA) model and the free-free absorption (FFA) model quantified by the following formulae:

$$S_\nu = S_0 \nu^{2.5}[1 - \exp(-\tau_s \nu^{\alpha - 2.5})] \tag{5.1}$$

for the SSA and

$$S_\nu = S_0 \nu^\alpha \exp(-\tau_f \nu^{-2.1}) \tag{5.2}$$

for the FFA, where ν is the observing frequency in GHz, S_0 the intrinsic flux density in Jy at 1 GHz, τ_s and τ_f are the SSA and FFA opacities at 1 GHz, and α is the optically thin spectral index.

For the SSA, the best-fit parameters are $\alpha = -0.22 \pm 0.01$, $S_0 = 2.2 \pm 0.1$ mJy, and $\tau_s = 1342.7 \pm 14.4$. In the case of FFA, we find $\alpha = -0.25 \pm 0.02$, $S_0 = 3.41 \pm 0.21$ Jy, and $\tau_f = 126.4 \pm 10.3$. The fitted spectra are shown in Figure 5.3 (a), and both of them fit the spectrum reasonably well. If we assume that the turnover is due to SSA, the magnetic field B of a homogeneous synchrotron component can be calculated via:

$$B^{\mathrm{syn}} = 10^{-5} b(\alpha) \nu_{\mathrm{max}}^5 \theta^4 S_{\mathrm{max}}^{-2} \delta / (1 + z), \tag{5.3}$$

where ν_{max} is the peak frequency in GHz, θ the source angular size in mas, S_{max} the peak flux density in Jy, and $b(\alpha)$ a tabulated parameter depending on the spectral index α (Marscher 1983). For the core, assuming $\delta = 14.1$ (see section 5.3.5), we obtain $B^{\mathrm{syn}} = 76.1$ mG with the following parameters: $b(\alpha) = 1.8$, $S_{\mathrm{max}} = 1.339$ Jy, $\nu_{\mathrm{max}} = 27.5$ GHz, $\theta = 0.09$ mas. This is not in agreement with the magnetic field estimation in Feng et al. (2006), who obtained 8 mG for the core component by assuming $\delta = 1$.

The spectra of the different jet components are shown in Figure 5.3 (b) along with their spectral fitting. For component n, there is most likely absorption at frequencies

below 43 GHz. From 43 and 86 GHz, the extrapolated flux density at 22 GHz is ∼ 0.9 Jy . Such a bright feature should have been detected/modelled at 22 GHz at a core distance of ∼ 0.4 mas (see also Figure 5.6). Other jet components (*d*, *e*, *f*, *g*, and *i*) displayed steep spectra in our observations except some indication of absorption for component *e* at 15 GHz. Further observations with wider frequency coverage for component *e* are needed to clarify this uncertainty. The corresponding optically thin spectral indices α ($S_\nu \propto \nu^\alpha$) are $\alpha_n = -1.90 \pm 0.19$, $\alpha_d = -0.93 \pm 0.09$, $\alpha_e = -0.51 \pm 0.21$, $\alpha_f = -0.71 \pm 0.03$, $\alpha_g = -1.89 \pm 0.92$, and $\alpha_i = -0.53 \pm 0.51$.
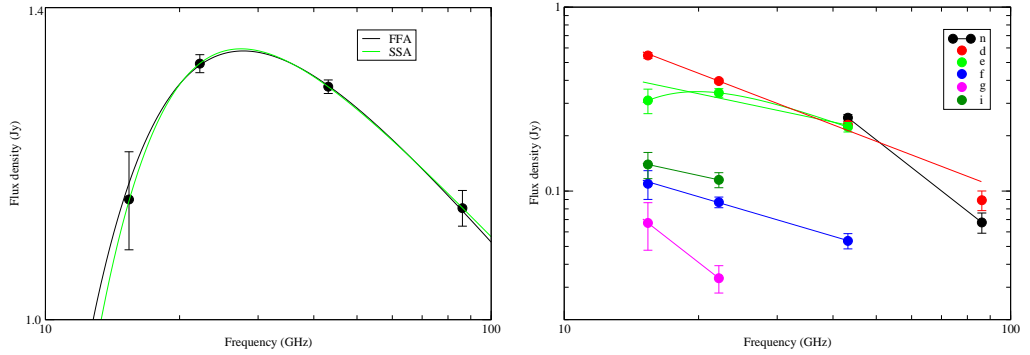
5.3 (a): Spectrum of the core. Both the SSA and FFA fits are shown.

5.3 (b): Spectra of the jet components. The spectrum of component *e* is fit with both the SSA and power law ($S_\nu \propto \nu^\alpha$).

Figure 5.3: Component spectra fit of NRAO 530 at 2007.4

We note that the obtained spectra of the jet components show significant evolution with increasing distance from the core. In Figure 5.4, the spectral index α is plotted against core separation. Along the jet, the spectrum steepens and flattens twice within a core distance of up to 9 mas. The oscillation of the spectral index indicates very different distribution of electrons at different core separations, and the spectral reversal may result from shocks/re-accelerations in the jet, or interaction between the jet and the surrounding medium.

A spectral index reversal along the jet was also observed in the FRII radio galaxy Cygnus-A (Krichbaum et al. 1998a) and in 3C 273 (Krichbaum et al. 2000). Interestingly, the spectral profile did not change for 3C 273 over a time period of two years, although different superluminal components occupied this region, suggesting that the observed properties of the jet are determined by the local physical environment or geometrical effects. In recognition of the correlation between the spectral flattening and the expansion of the jet (local maxima of the transverse jet width) in Cygnus-A and 3C 273, Qian et al. (2001) proposed that this phenomenon could be explained by transverse stratification of the jet. In their model, the physical parameters (e.g., jet flow
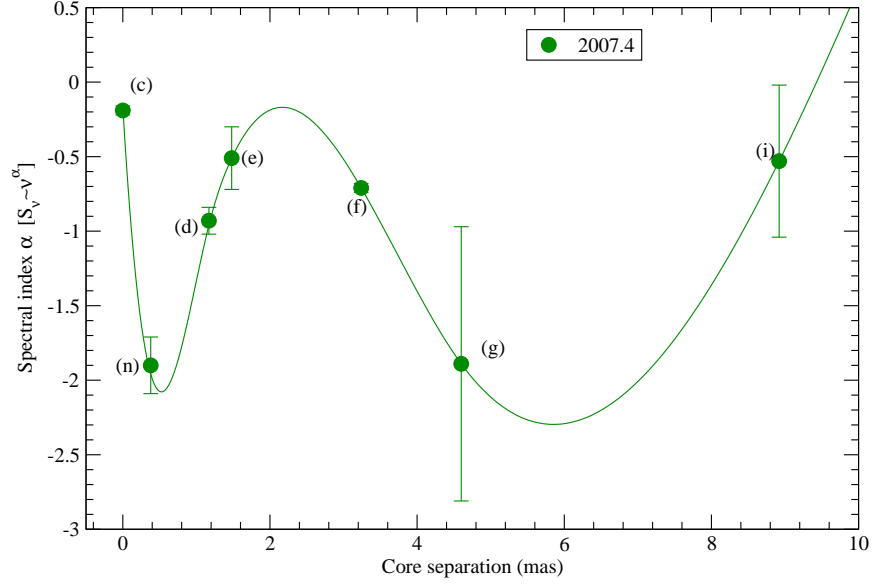
Figure 5.4: Optically thin spectral index α plotted as a function of core separation along with a cubic spline interpolation showing a quasi-sinusoidal pattern with increasing characteristic scale. In order of increasing core separation, the symbols are for the core component *c* and jet components *n*, *d*, *e*, *f*, *g*, and *i*. The relative larger uncertainties at core separation beyond 4 mas is due to the narrow range of frequency coverage (between 15 and 22 GHz) and the weakness of the jet components.

velocity, Doppler beaming, electron density, electron energy, electron acceleration, B-field strength, etc.) across the jet depend on the distance to the jet axis.

5.3.2 Frequency-dependence of Component Positions

The 10-day repeated measurements at 22, 43, and 86 GHz allow us to investigate the frequency-dependent position shift of the jet components. In Figure 5.5 we plot the core separation against position angle for the jet components detected at any two of these three frequencies. By using the additional data at 15 GHz (epoch 2007.44), the spectra of the core and components *d*, *e*, and *f* are also shown (see also Figure 5.3). The time averaged values of core separation and P.A. are summarized in Table 5.1.

As it can be clearly seen in Figure 5.5, the relative positions of three components (*d*, *e*, and *f*) shifted systematically between 22 and 43 GHz. These are components whose positions are most reliably measured in our experiments. For all three components, the core separation at 43 GHz is larger than that at 22 GHz, with a difference significance at $> 3\sigma$ level (see Table 5.1). For the components *d*, *e* and *f* the position

shift between 22 and 43 GHz is −0.17, −0.12, and −0.14 mas, respectively. For the P.A., however, only component *f* shows significant difference at > 4 σ level. The measured position of component *d* at 86 GHz is consistent with the low frequency data in the sense that the core distance at 86 GHz is larger than that at lower frequencies. For component *n*, we are unable to compare the position shift between 43 and 86 GHz limited mainly by the large position scatter at 86 GHz. At the same time, the observations at 15 GHz also provide consistency checks for the components *d*, *e*, and *f*. To further verify this position shift effect, we show in Figure 5.6 slices made along P.A. of −10° for the inner ~ 2 mas of the jet. One can clearly see that the peak of the component *d* is displaced between 22, 43 and 86 GHz. For the innermost jet component *n*, however, it is impossible to reliably model it at frequencies ≤ 22 GHz and the positions measured at 86 GHz suffer from large scatter.
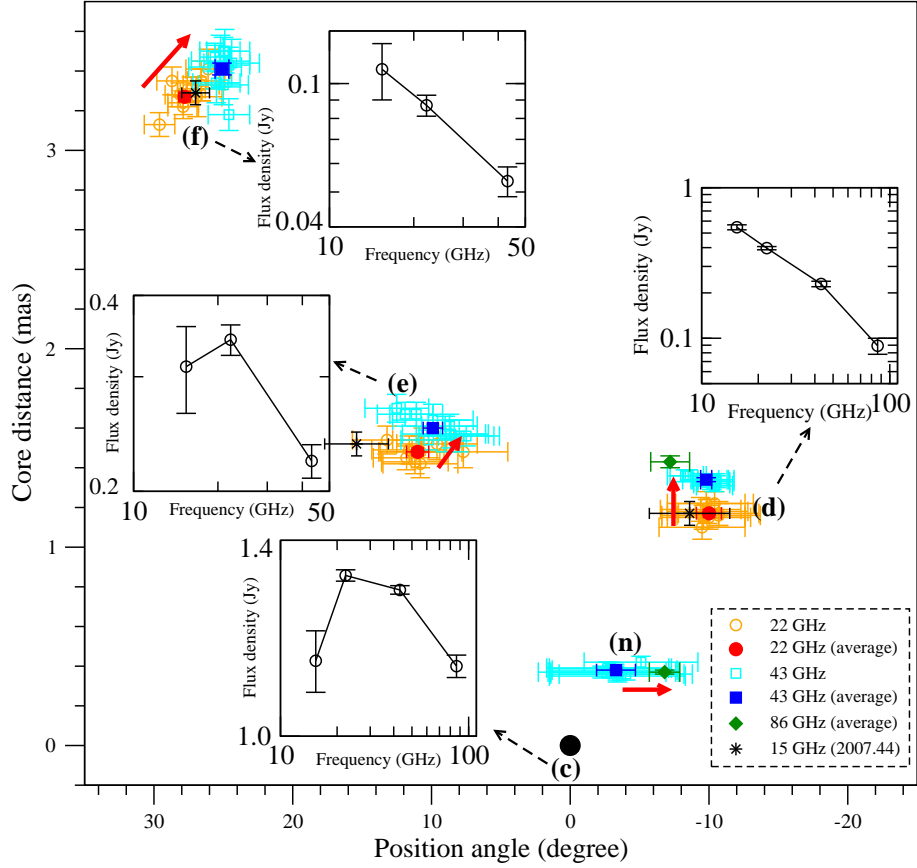
Figure 5.5: Core separation plotted against position angle for the inner jet components. Different symbols denote different frequencies with the filled symbols representing the average values at 22 (filled circles), 43 (filled squares) and 86 GHz (filled diamonds). To prevent confusion, only average values are shown at 86 GHz. A clear frequency-dependent displacement of the jet component positions can be seen and is indicated by red arrows. Spectra are shown for those components visible at more than 2 frequencies (insets).

Table 5.1: Position shift of jet components. Listed are the component Id., the time averaged value of ten days of components' core separation (r) and P.A.(θ) at 22, 43, and 86 GHz. The last two columns summarize the position shift between the two frequency pairs (22-43 GHz and 43-86 GHz) for each component.

Id.	22 GHz		43 GHz		86 GHz		$\triangle r_{22/43}$	$\triangle r_{43/86}$
	r	θ	r	θ	r	θ		
	[mas]	[degree]	[mas]	[degree]	[mas]	[degree]	[mas]	[mas]
n	...	...	0.38±0.01	−3.3 ± 1.4	0.37±0.01	−6.8 ± 1.1	...	0.01±0.01
d	1.17±0.02	−10.0 ± 0.9	1.34±0.01	−9.8 ± 0.4	1.43±0.03	−7.2 ± 1.4	−0.17 ± 0.02	−0.09 ± 0.03
e	1.48±0.02	11.0±0.8	1.60±0.02	9.9±0.7	...	...	−0.12 ± 0.03	...
f	3.27±0.02	27.8±0.4	3.41±0.03	25.1±0.5	...	...	−0.14 ± 0.04	...

A well known effect which causes the frequency dependence of jet component position is the opacity-induced position shift of the VLBI core ("core shift", Lobanov 1998) in a synchrotron-self absorbed jet (Blandford & Königl 1979). The VLBI core position which is defined by the $\tau = 1$ surface at the jet base depends on the frequency, with the distance to the central engine, $r_{core} \propto \nu^{-1/k_r}$, where k_r is related to the electron energy distribution, the magnetic field, and the particle number density (Konigl 1981). If the core is self-absorbed and in equipartition between the energy density of the particles and that of the magnetic field, one can show that $k_r = 1$ (Lobanov 1998). Recent measurements are consistent with $k_r = 1$ (e.g., O'Sullivan & Gabuzda 2009). Between two frequencies ($\nu_2 > \nu_1$), the core shift can be expressed as:

$$\triangle r_{core} = (r_{core}^{\nu_1} - r_{core}^{\nu_2}) \propto (\nu_1^{-1/k_r} - \nu_2^{-1/k_r}) \mid_{k_r=1} \propto \frac{\nu_2 - \nu_1}{\nu_2 \nu_1} \qquad (5.4)$$

Since the absolute position information for VLBI observations is lost due to the phase self-calibration, core shifts are normally measured by referencing the core to the optically thin jet components, whose positions are expected to be frequency-independent.

The number of extragalactic radio sources with reported core shift has been increasing (Cai et al. 2007; Kovalev et al. 2008; O'Sullivan & Gabuzda 2009, and references therein). Kovalev et al. (2008) studied a core shift sample of 29 AGN between 2.3 and 8.4 GHz. They found the magnitude of measured core shift between 2.3 and 8.4 GHz to range from −0.1 to 1.4 mas with a median value of 0.44 mas[12]. For higher frequency pairs, we would expect that the core shift decreases since opacity effects become less important (Equation 5.4). For a few sources where core shifts between high frequency pairs are available (O'Sullivan & Gabuzda 2009), the reported core shifts between 22 and 43 GHz (0.02–0.04 mas) are significantly smaller than those for d, e, and f component (0.12–0.17 mas) in NRAO 530. In addition, the displacement of jet components' position are not all in the same direction. In other words, there are non-radial shifts, which may indicate two dimensional gradients of the jet parameters (magnetic field, particle number density), an effect which is expected if a bent jet is observed at small viewing angles.

5.3.3 Flux Density and Structure Variability on Daily Timescales

Our data also permit us the study of flux density and structure variability in the VLBI jet of NRAO 530 on daily timescales. We show in Figure 5.7 the variations of the

---

[12]Positive values mean that the separation of the jet component measured at higher frequency is larger than the one measured at lower frequency in one frequency pair.
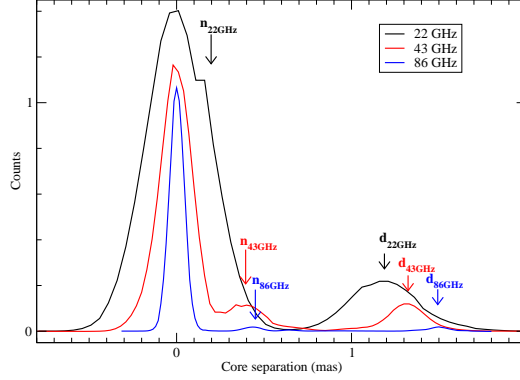
Figure 5.6: Slice along P.A. = −10° through the total intensity maps of the inner 2 mas of NRAO 530 at 22, and 43 GHz on May 15, 2007 and at 86 GHz on May 16, 2007. An increase of the core separation of components *n* and *d* with frequency can be interpreted as opacity shift of the core position (see text).

flux density of the model fit components with modulation indices summarized in Table 5.2. On daily timescales, the flux density of most model fit components shows no significant variations. Component *g* seems to be more variable ($m = 53\,\%$). However, it is the weakest component representing a diffuse region with flux density of only $\sim$ 30 mJy. This may in turn reflect our modeling uncertainties. Through a χ^2-test (see Table 5.2) we found the probability for variability for most of the components to be low. For component *c* and component *n*, the χ^2-test indicates the presence of inter-day variability with probability of 85 % at 22 GHz and 92 % at 43 GHz for component *c* and 99.9 % at 43 GHz for component *n*.

Similarly, the variations of the core separation and P.A. of the jet components are displayed in Figure 5.8. The modulation indices m, χ^2_ν, and the probability for the studied source parameters to be variable are tabulated in Table 5.3 and 5.4. For the core separation, the scatter in component *g* is again much larger than what we expected from statistical errors. In addition, the large scatter for the core separation of component *n* and *d* at 86 GHz also indicates there are additional errors that are not accounted for by the general accepted "rule of thumb", i.e. 1/5 beam size. This may be due to the sparse *uv* coverage at 86 GHz and the weakness of the components. For the P.A., all the components show stationarity except component *d* at 86 GHz, which shows similar large scatter to the core separation. We therefore conclude that we see indications of inter-day variability in the flux for the core and the inner jet component *n* at 22 and 43 GHz. There is also an indication of the variability of the core separation of component *n* and possibly *d* at 86 GHz. The limited *uv* coverage and calibration accuracy at 86 GHz however may cause such variability making it necessary to confirm this effect

84

Table 5.2: Flux variability characteristics of model fit components of NRAO 530.

Id.	22 GHz m [%]	χ^2_ν	p [%]	43 GHz m [%]	χ^2_ν	p [%]	86 GHz m [%]	χ^2_ν	p [%]
c	3.1	1.5	84.6	2.3	1.7	92.3	4.4	0.6	19.4
n	-	-	-	13.3	3.0	99.9	23.3	0.4	6.8
d	3.5	0.2	0.5	8.7	0.4	7.7	34.9	0.9	49.3
e	9.1	0.3	2.2	13.8	0.5	15.7	-	-	-
f	8.7	0.2	0.3	15.2	<0.1	< 0.1	-	-	-
g	53.2	1.1	67.6	-	-	-	-	-	-
i	15.5	0.3	1.9	-	-	-	-	-	-

Notes: Listed are the component Id., the modulation index, reduced χ^2_ν, probability for the observable being variable.

in future VLBI studies.

5.3.4 Morphology and Its Evolution

On pc scales, NRAO 530 shows a typical bending jet with the curvature being more pronounced close to the core. This can be clearly seen in Figure 5.9, where we show the core separation as a function of position angle for the jet components in 1997 and 2007. Since the jet axis is close to the observer's line of sight, as indicated by the observed apparent superluminal motion, it is certain that the apparently curved morphology is resulted from amplification effects by projection. However, the physical reason for the intrinsic jet bending is unclear. Several possible scenarios are still under discussion including, for instance, hydrodynamic Kelvin-Helmholtz (K-H) helical instabilities (Hardee 1987), helical shock model (Gomez et al. 1994), regular (precession) or erratic change of the jet-ejection angle (see Britzen et al. 2010, and references therein), and external causes e.g., interaction with surrounding medium. Although the mechanism which could induce the non-radial motion is still an open question, one of the widely discussed scenarios is the binary black hole model (e.g., Roland et al. 2008). In this scenario, the precession of the accretion disk(s) and the orbital motion of the two black holes around their common gravity center cause the perturbation of jet motion.

A comparison of the projected trajectory of jet components in 1997 and 2007 (Figure 5.9) indicated that the morphology of the jet changed significantly. It is obvious

Table 5.3: Variability characteristics of core separation for the jet components.

Id.	22 GHz m [%]	χ^2_ν	p [%]	43 GHz m [%]	χ^2_ν	p [%]	86 GHz m [%]	χ^2_ν	p [%]
n	-	-	-	5.3	0.4	9.2	11.3	3.5	> 99.9
d	3.0	0.4	4.3	1.2	0.3	1.8	6.0	2.5	98.8
e	2.9	0.4	6.9	3.6	0.8	42.5	-	-	-
f	2.4	1.3	74.6	3.2	1.4	82.0	-	-	-
g	8.8	3.3	> 99.9	-	-	-	-	-	-
i	0.8	0.1	< 0.1	-	-	-	-	-	-

Notes: Listed are the component Id., the modulation index, reduced χ^2_ν, probability for the observable being variable.

Table 5.4: P.A. variability characteristics of model fit components for NRAO 530.

Id.	22 GHz m [%]	χ^2_ν	p [%]	43 GHz m [%]	χ^2_ν	p [%]	86 GHz m [%]	χ^2_ν	p [%]
n	-	-	-	24.5	< 0.1	< 0.1	44.9	0.8	38.6
d	4.8	< 0.1	< 0.1	8.2	0.4	5.8	60.0	4.0	> 99.9
e	11.8	0.3	1.4	17.5	0.6	19.1	-	-	-
f	3.7	0.7	30.2	1.7	< 0.1	< 0.1	-	-	-
g	16.7	0.2	0.7	-	-	-	-	-	-
i	5.0	0.5	9.2	-	-	-	-	-	-

Notes: Listed are the component Id., the modulation index, reduced χ^2_ν, probability for the observable being variable.
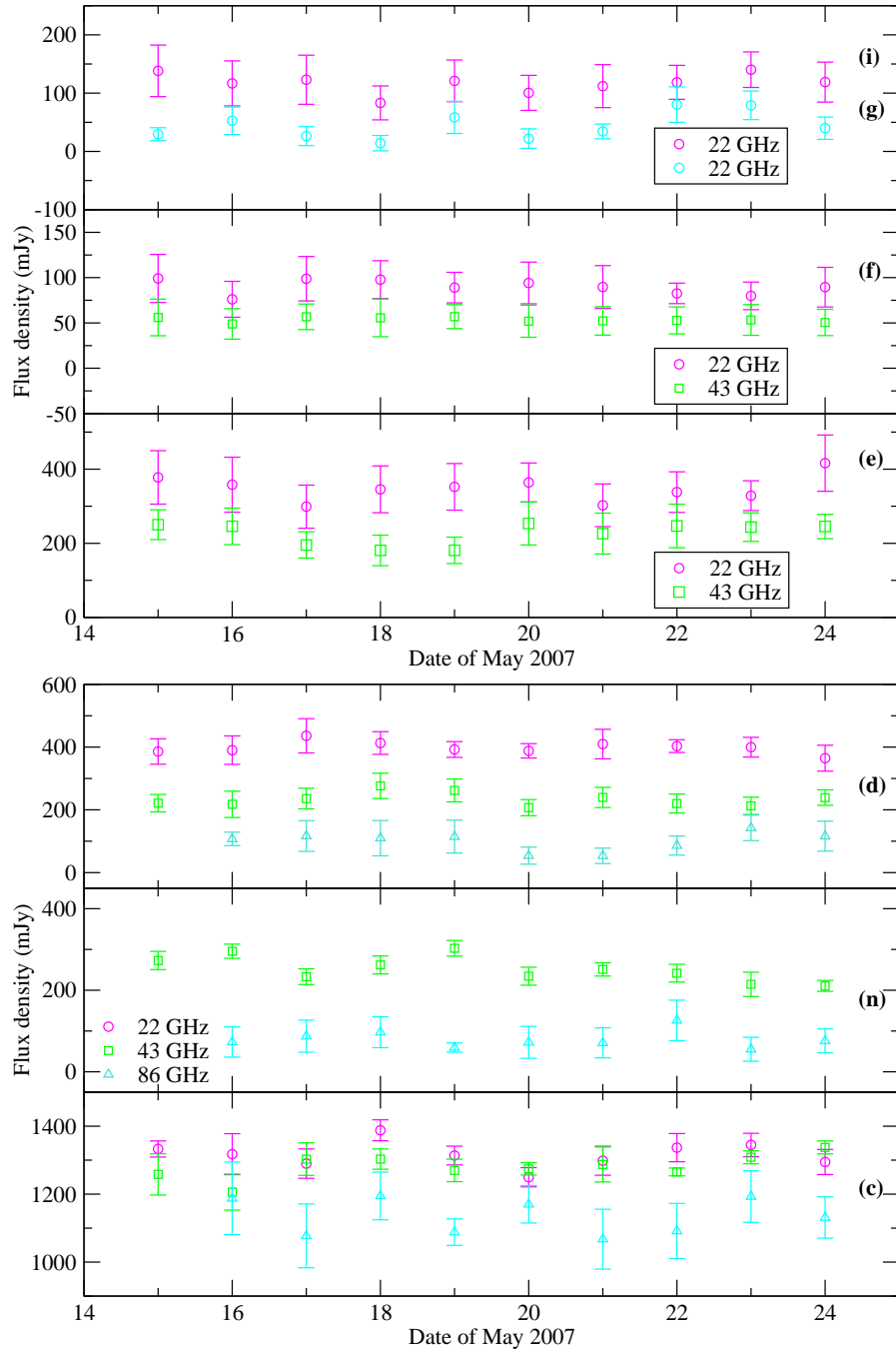
Figure 5.7: Variations of the flux density of model fit components on daily timescales. Top panel for outer jet components (*i*, *g*, *f*, and *e*), bottom panel for inner components (*d*, *n*, and *c*). Note that components *i* and *g* are only visible at 22 GHz.

that the major differences are in the regions close to the core, in contrast to the relative "position" stability of the outermost component. This can be attributed to the relatively fast motion of the inner jet components (see next section). Figure 5.10 (left) shows the
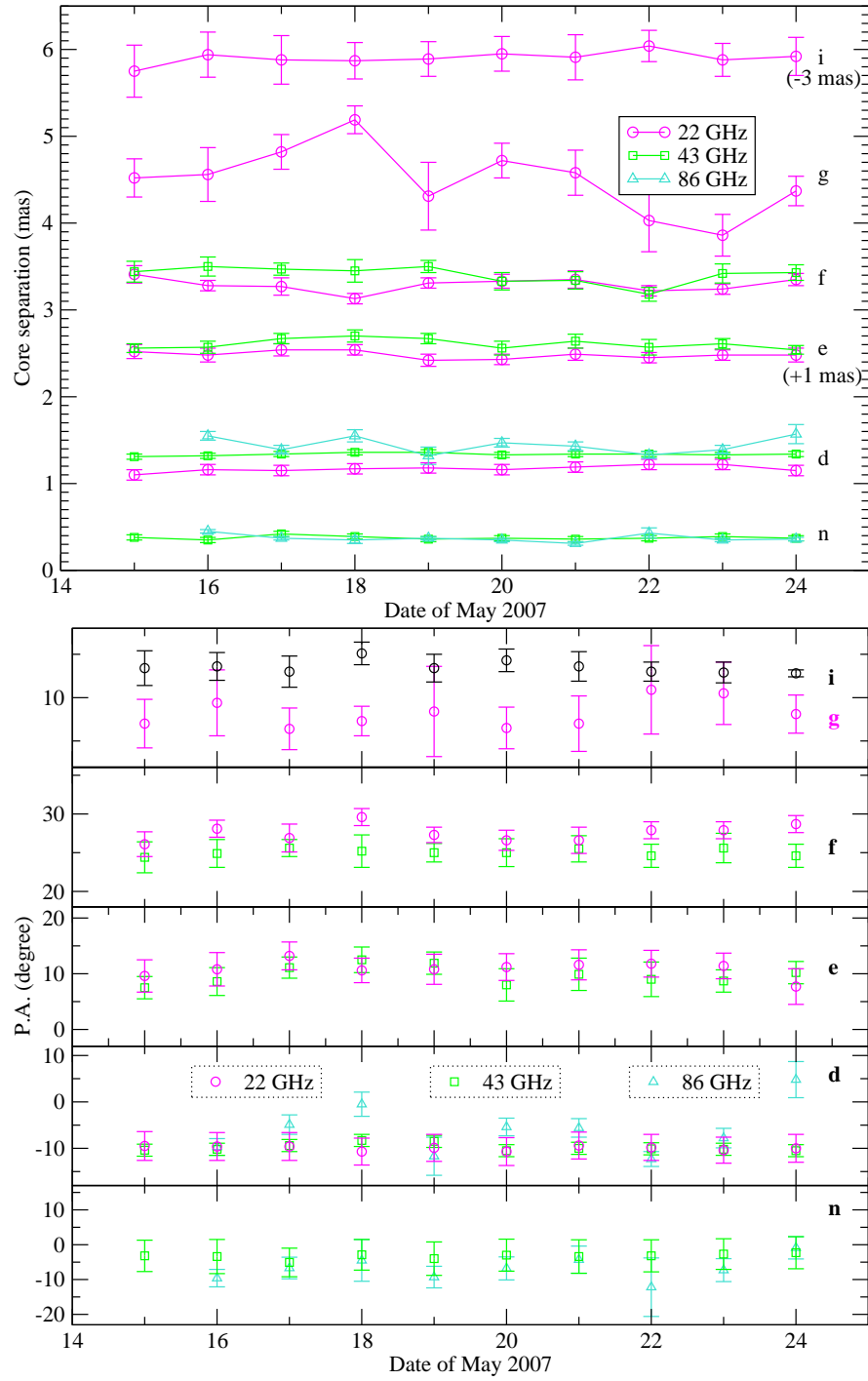
Figure 5.8: Variations of the core separation (upper panel) and P.A. (bottom panel) of model fit components on daily timescales. Different symbols denote different frequencies (circles: 22 GHz; squares: 43 GHz; triangles: 86 GHz). The core separation of component *i* and *e* has been shifted for display purposes.
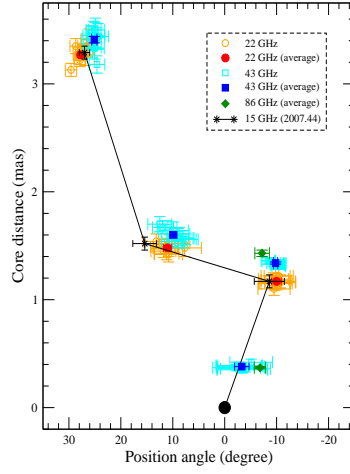
5.9 (a): within inner 3.75 mas.
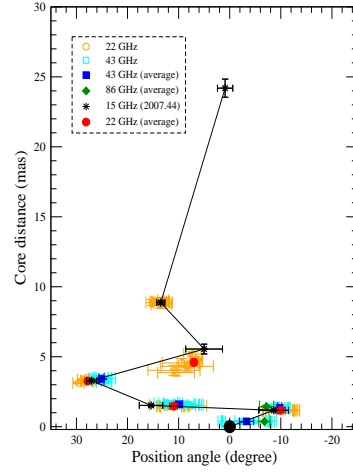
5.9 (b): within 30 mas.
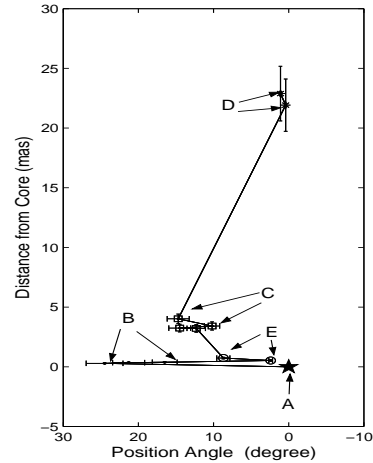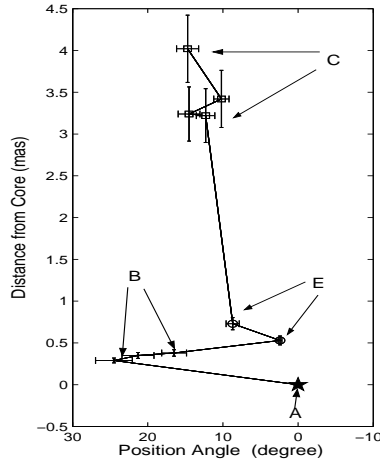
5.9 (c): Left: within inner 4.5 mas. Right: within 30 mas (Feng et al. 2006).

Figure 5.9: Comparison of projected trajectory of jet components between 2007 (upper panels) and 1997 (lower panels).

evolution of the jet ridge line over the last 10 years obtained by the 15 GHz data. This plot illustrates that the morphology of the jet changes from epoch to epoch due to the motion of the jet components. Shown in Figure 5.10 (right) is the evolution of the inner jet axis with the component *d* being the tracer. Both radial and non-radial motion is observed for this component and a jet position angle swing of ∼ 4°/yr can be estimated between 1999 and 2009. Taking advantage of the high resolution provided by mm-VLBI, Agudo et al. (2007) reported a jet position angle swing of ∼ 11°/yr associated with non-ballistic superluminal motion for NRAO 150. It is not clear whether the swing speed increases for jet components even closer to the core of NRAO 530. How-
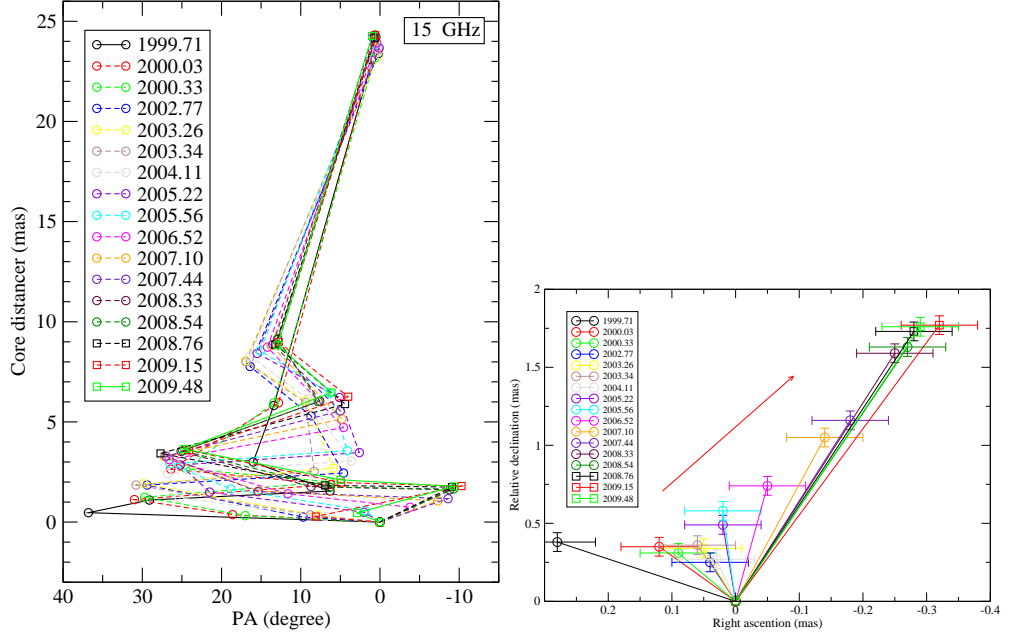
Figure 5.10: Left: The jet ridge line between 1999 and 2009. Right: Motion of inner jet component *d* in rectangular coordinates

ever, the data at 15 GHz do not allow us to investigate the evolution of the innermost jet components, like component *n*. Therefore, future VLBI monitoring observations at higher frequencies will be of great importance in this sense.

5.3.5   Jet Kinematics at 15 GHz

In this section, we investigate the kinematics of the jet components at 15 GHz. The plot of the core separation of jet components as a function of time, as shown in Figure 5.11, served as a tool for cross-identification across epochs. We note, however, that the identification of the innermost jet component *d* at epochs before 2001 may be subject to ambiguity due to the gaps during 2000 and 2002. The systematic change of flux and position angle (see next) supports however our identification scheme also for component *d*. Linear regression fits to the data after 2002 yielded the epoch of ejection coinciding with the time of a radio flare ($\sim$ 2002.6, Hong et al. 2008, see Figure 5.2) during the last 10 years. This may indicate that *d* is a component newly ejected during that flare. Component *e* appears to separate from component *f* after 2003. This scenario is supported by the sudden change in the flux of component *f* (whose flux density would be maintained after the separation by adding the flux density of component *e*), the similar position angles of *f* and *e* in 2004, and the lack of components between *d*

Table 5.5: Linear fit results on the core separation of the jet components at 15 GHz. Listed are the component Id., number of epochs for the fit, proper motion μ, apparent velocity β_{app}, and ejection time of each component t_0.

Id.	#	μ	β_{app}	t_0
		[mas/year]	[c]	[year]
n′	2	0.55±0.26	26.5±12.5	2008.6±0.4
d	14	0.26±0.02	12.4±1.0	2002.5±0.3
e	11	0.13±0.02	6.2±1.1	1994.4±2.4
f	17	0.29±0.01	14.1±0.5	1996.0±0.4
g	11	0.44±0.03	21.3±1.5	1996.4±0.5
h	9	0.05±0.05	2.3±2.5	1876.6±133.6[a]
i	14	0.19±0.01	9.2±0.5	1960.8±3.6
j	17	0.13±0.01	6.3±0.5	1823.1±14.7

[a]From formal back-extrapolation

and *f* in earlier epochs before 2004. The most reliable identification corresponds to outer components *f, g, h, i, j*, and the newly ejected component *n′*.

In order to derive estimates for the separation speeds of the individual components, we applied linear regression fits ($f(t) = a \cdot (t - t_0)$, where t_0 is the component ejection time) to the separation of the components from the core versus the epoch of observations. The fitting results are shown in Figure 5.11 as dashed lines with the fitted separation speeds, the time of ejection, as well as the apparent speeds given in Table 5.5.

Component *n′* seems to show the maximum apparent speed ($\beta_{app} = 26.5 \pm 12.5$). However, the speed had to be calculated on the basis of only 2 epochs and is therefore subject to large uncertainties. It was ejected around 2008.6, which coincides with the second moderate flare seen in late 2008 at millimeter wavelengths[13] and in early 2009 at centimeter wavelengths (Figure 5.2). Component *f* and *g* can be identified with components B and E seen by Feng et al. (2006). The derived apparent speeds (14 *c* and 21 *c*) are slightly faster than their findings (10 *c* and 14 *c*), based on data over a short time interval (~ 4 yr). The ejection time of both components lies in the range of the dramatic outburst phase between 1994 and 1998. However, due to the expansion effects, the uncertainty of core separation for component *g* gets systematically larger at later epochs and at the same time, it shows an acceleration indicating that a linear fit

[13]cf. http://sma1.sma.hawaii.edu/callist/callist.html?data=1733-130

to the component motion is only a rough approximation. Component *e* and the three outer components (*h*, *i*, and *j*) reveal relatively slow motions with β_{app} in the range of 2–9 *c*.
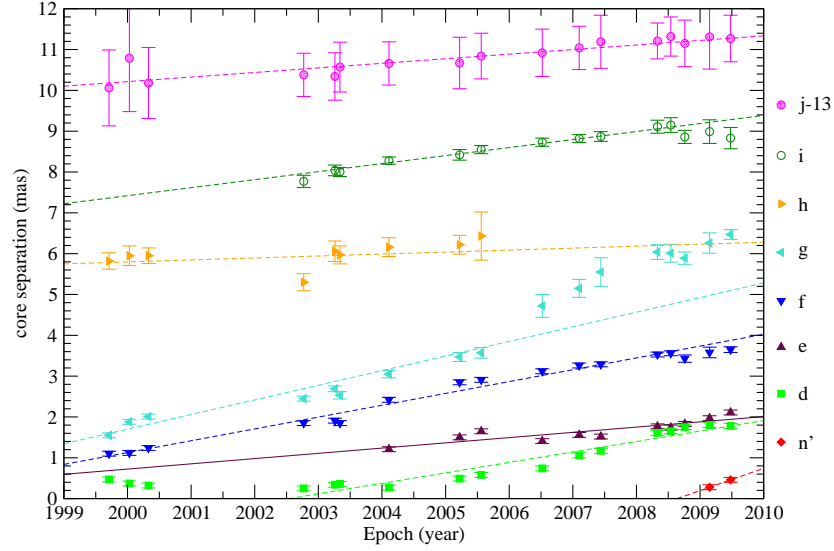
Figure 5.11: Separation from the core as a function of time for jet components in NRAO 530. The core separations of component *j* have been shifted 13 mas downwards for display purposes, and the component *x* is not shown. The dashed lines are linear regression fits to the data.

The measured apparent velocities can be used to estimate the parameters of the jet components according to the superluminal motion equation (Equation 1.7). Making use of the apparent speed of component *f* ($\beta_{\mathrm{app}} = 14.1\,c$), which is the most reliably determined fastest component, we can set a lower limit on the Lorentz factor Γ, $\Gamma_{\mathrm{min}} = \sqrt{1 + \beta_{\mathrm{app}}^2} = 14.1$, and derive maximum allowable viewing angle θ_{max} of 8.1°. The critical viewing angle, which maximizes the β_{app} for a given β, is $\theta_{\mathrm{cri}} = \arcsin(\frac{1}{\Gamma})$. For component *f*, θ_{cri} is 4.1°. Correspondingly, we can also derive a Doppler factor δ_{min} using the minimum Lorentz factor Γ_{min} and θ_{cri}. For component *f*, δ_{min} is 14.1. For even smaller angles ($\theta \to 0$), δ tends to the limit of $\sim 2\Gamma = 28.2$.

Figure 5.12 shows the relation between the apparent speed, the Doppler factor and the viewing angle. For a given Lorentz factor, the apparent speed first shows a shallow increase with decreasing viewing angle and then decreases sharply towards very small angles. Therefore, Equation 1.7 has for a given apparent speed, two solutions for the viewing angle. However, the Doppler factor, which has a strong influence on the observed flux density due to the beaming effects (Equation 1.9), shows a different orientation dependence and increases continuously with decreasing viewing angle.

Based on these signatures and how the apparent speed and flux density of the jet component evolves, we can estimate the jet geometry. For component *f*, we found both the flux density and apparent jet speed decrease at later epochs (see Figure 5.11 and 5.14 below), indicating that the viewing angle takes the small viewing angle solution and is increasing with time. For component *g*, however, our viewing angle may be approaching the critical value because of the increase of the apparent speed and the decrease of the flux density.
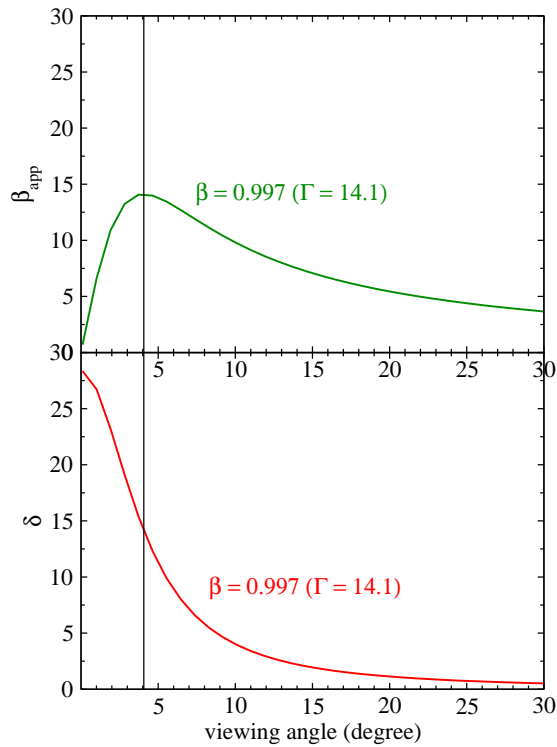
Figure 5.12: Apparent speed (upper panel) and Doppler factor (lower panel) as a function of viewing angle for component *f* with a Lorentz factor of 14.1. The vertical line indicates the critical angle (4.1°) at which the apparent speed is maximized.

In Figure 5.13 we present the evolution of the position angle of jet components with time. One can clearly see that the swing position angle of components *d*, *e*, *h*, and *i* is in contrast to the stationarity of the components *f*, *g*, and *j*. The newly ejected component *n′* also shows a similar position angle rotation (not shown). The changes of position angle with time clearly indicate a non-radial, non-ballistic motion of the jet components.

In Figure 5.14 the flux density evolution of the modeled components at 15 GHz is displayed. Interestingly, the flux density evolution of the modeled components is characterized by several distinct behaviors. For components *i* and *j*, the flux density
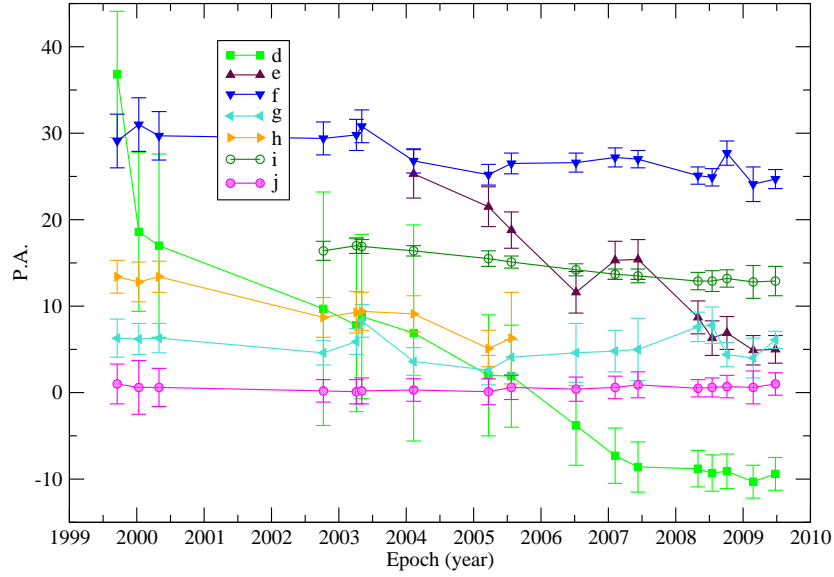
Figure 5.13: Evolution of jet P.A. for components *d–j*.

remains nearly constant, while for components *g* and *h*, the flux density continuously decreases with time. It seems that the drop in the light curve of component *f* around 2004 was due to the separation of *e* from it. Component *e*, however, shows a clearly increasing trend. Component *d* shows convolved behavior before the peak around 2004 and fades afterwards as it travels down the jet. The core component *c* shows two intermediate flares, which coincide with the ejection of component *n'* and probably also with the ejection of component *d*, if it was ejected around 2002 according to the straightforward back-extrapolation.

Based on the modeled flux density for each components, the total VLBI flux is calculated and is plotted against time as shown in Figure 5.15. In addition, the P.A. of component *d* is also displayed. The P.A. of component *d* flattens twice and it is notable that the variations of total VLBI flux is related to the change of P.A. of component *d*, suggesting a geometrical origin (i.e, projection effect) of the flux variations.

5.4 Conclusion

In this chapter, we studied the pc-scale jet properties of NRAO 530 by using high-resolution multi-epoch VLBI observations at 15, 22, 43, and 86 GHz. We identified component *c* as the core based on its flat spectrum and variability using the quasi-simultaneous VLBI data obtained in 2007. We find that the optically thin spectral indices of the components evolve with the core distance (spectral reversal) with an
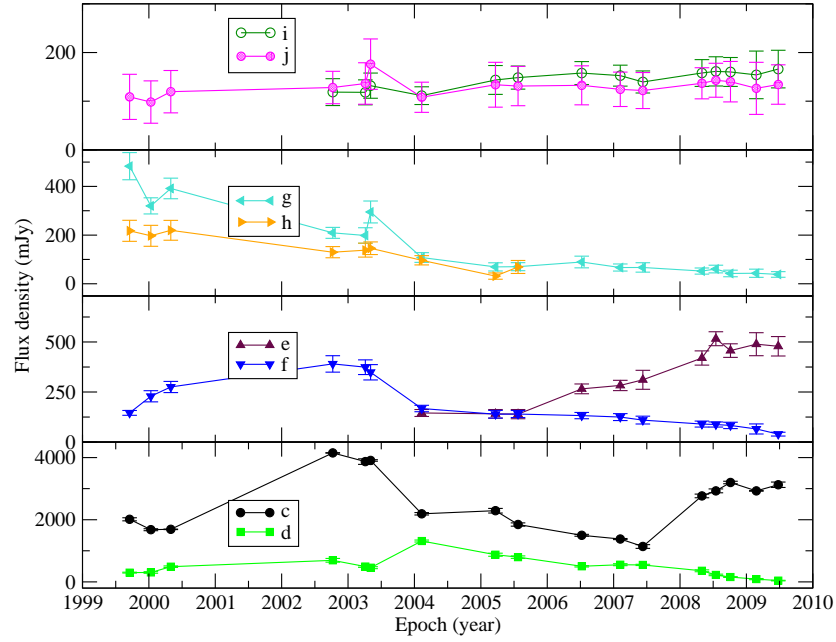
Figure 5.14: 15 GHz flux density of each model fit component plotted vs. time.
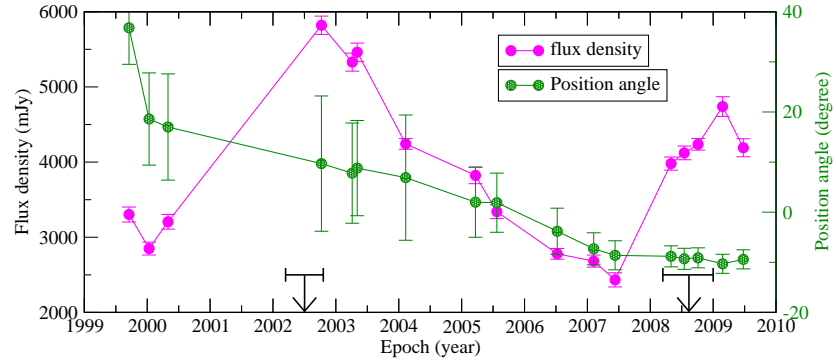
Figure 5.15: Total VLBI flux density of NRAO 530 at 15 GHz and position angle of the component *d* plotted versus time. The arrows mark the ejection time for components *d* and *n′* with the flat bar indicating the uncertainty in the ejection time.

increasing characteristic scale. The frequency-dependent position shifts are found to be significant for 3 components (component *d*, *e*, and *f*) with mean shift of 0.15 ± 0.02 mas between 22 and 43 GHz. The position shift can be interpreted as being due to a core shift effect in a synchrotron self-absorbed jet. Interestingly, we find, for the first time, that one component (*f*) shows a two-dimensional position shift, significant at > 4 σ level. This indicates that the variations of the optical depth, which induces the core-shift, have also a non-radial dependence. Our 10-day monitoring observations allow us to investigate the jet variability characteristics on daily timescales for NRAO 530.

We find inner jet being more variable than outer jet.

The morphology of NRAO 530 was found to have changed significantly over the past 10 years between 1997 and 2007. The variations are more pronounced near the core in contrast to the apparent "stationarity" of components further out. We studied the jet kinematics with individual components using the archival data at 15 GHz. We estimated superluminal motions for 8 components with apparent speeds β_{app} in the range of 2–26 c. From the back-extrapolation, the ejection of component n' can be associated with the moderate flare in the radio light curve around 2009. However, the identification of the ejection time of component d is subject to uncertainties, and so is the link between its ejection and the moderate flare around 2002. From the measured apparent jet speed, we can set limitations on the jet parameters. For the reliably measured fastest component, we obtained minimum Lorentz factor of 14 and Doppler factors in the range of 14 and 28. Using the variations of the apparent speed and flux density, we can put constrains on the variations of viewing angles for different jet component. We noticed that no common path exist for all the jet components. Moreover, we found significant variations of the jet position angle. For component d, we estimated a mean swing of ~ 4° per year between 1999 and 2009, which is partly responsible for the variations of the inner jet structure. Different components showed different kinematical behavior and flux density evolution. The related variations of total VLBI flux with the change of P.A. of component d is indicative of a geometrical origin.

To summarize, we conclude that the jet of NRAO 530 is far more complex that previously known. The observed non-ballistic motion and a pronounced change of the jet orientation with a rate of 4° per year suggests, that NRAO 530 is another example of a "swing" jet, similar to e.g., BL Lac (Stirling et al. 2003) and NRAO 150 (Agudo et al. 2007).

6 Summary and Future Outlook

6.1 Summary

In this thesis we have described high frequency VLBI studies of the compact radio source at the center of the Galaxy, Sgr A* and the OVV blazar, NRAO 530. High frequency VLBI observations provide unprecedented resolution (in astronomy) and allow the study of regions in AGNs which are inaccessible to VLBI at cm wavelengths (Chapter 3). For Sgr A* , high frequency VLBI is the only way to directly image its intrinsic structure due to the scatter-broadening effect of the interstellar medium, which prevents such studies at longer wavelengths.

In Chapter 4, we presented results from a high frequency intra-day VLBI monitoring of Sgr A* during a global multi-waveband campaign in May 2007. We obtained accurate flux densities and sizes of the, at mm-wavelength partially resolved, pointlike VLBI structure. We studied the variations of the total VLBI flux density of Sgr A* on daily time scales and we find that the variability is correlated at our 3 observing frequencies with higher variability amplitudes appearing at the higher frequencies. The radio spectrum is inverted between 22 and 86 GHz, suggesting inhomogeneous synchrotron self-absorption with a turnover frequency at or above 86 GHz. The radio spectral index correlates with the flux density, being harder (more inverted spectrum) when the source is brighter. The average source sizes appear to be non-variable over the 10-day observing interval. Detected marginal size variations at 86 GHz need further confirmation. However, we see a tendency that the sizes of the minor axis increase with increasing total flux, whereas the major axis remains constant. Towards higher frequencies, the position angle of the elliptical Gaussian increases, a consequence of intrinsic structure, which begins to dominate over the scatter broadening. At cm-wavelength, the source size varies with wavelength as $\lambda^{2.12\pm0.12}$, which is interpreted as being due to interstellar scatter broadening. After removal of this scatter broadening, the intrinsic source size varies as $\lambda^{1.4..1.5}$. The VLBI closure phases at 22, 43, and 86 GHz are zero within a few degrees, indicating a symmetric or point-like source structure. Analysis of the closure amplitudes demonstrates the equivalence of

self-calibration and modeling of closure quantities. At the highest frequency available to our observations, the poor agreement of a single Gaussian model with the data indicates that the Gaussian model is only a crude approximation to the source structure. In the context of an expanding plasmon model, we obtain an upper limit of the expansion velocity of about $0.1\,c$ from the non-variable VLBI structure. This is in agreement with the velocity range derived from the radiation transport modeling of the flares from the radio to NIR wavelengths.

In Chapter 5, we discussed results from multi-epoch high resolution VLBI studies of the quasar NRAO 530. From these observations, we investigate the spectral properties of the VLBI components. We identified the compact component located at the southern-end of the jet as the VLBI core, which is consistent with previous studies. The spectra of jet components display a pronounced evolution with increasing core distance. The ten-day monitoring data at the 3 high frequencies were shown to produce high quality and self-consistent measurements of the component positions, from which we detected a 2-dimensional position shift. In addition, the repeated measurements also permit us to investigate the inter-day flux density and structure variability of NRAO 530. We find that it is more variable for inner jet components than those further out from the core.

We studied the jet kinematics over a period of 10 years using the archival 15 GHz data. The changes in the morphology of NRAO 530 were related to the motion of separate jet components with the most pronounced changes occurring at the regions close to the core. We obtained apparent velocities of 8 components with β_{app} ranging from 2 to $26\,c$. Accordingly, we estimated jet physical parameters with the minimum Lorentz factor of 14 and Doppler factors in the range of 14 and 28 (component *f*). Non-radial motion seems not uncommon to jet components. For NRAO 530, we estimated a P.A. swing of 4° per year for component *d*. The flux density and kinematics show different behavior for different components. Finally, the flux density variations of NRAO 530 are found to be related to the change of the P.A. of the component very close to the core (*d*), indicating that the flux density variability is (partially) geometric in origin. The non-ballistic motion and change of jet orientation makes this source another prominent example of a helical and possibly "swing" jet.

6.2   Future Outlook

Direct imaging of the central regions of AGNs is indispensable for testing the gravitational effects in the vicinity of SMBHs. This requires these objects to be investigated with the highest possible angular resolution, and most importantly, at frequencies high

enough to overcome opacity (and scattering, in the case of Sgr A*) effects.

As mentioned in Chapter 3, 3 mm-VLBI is nowadays routinely carried out with GMVA at 86 GHz, achieving an angular resolution of ~ 65 μas corresponding to a spatial resolution of $\sim 9 R_{\mathrm{Sch}}$ for M 87 (see Table 2.1). Adding more sensitive new antennas, and increasing the recording bandwidth in the near future, will enhance the sensitivity of 3 mm-VLBI down to a level commensurate with that of the present day cm-VLBI. At even higher frequencies (e.g., 147, 230 GHz), however, observations were still limited to dedicated experiments(Krichbaum et al. 2008, and references therein). These pilot experiments explored the potential of mm-VLBI, demonstrated the feasibility of both the technique and the source (in terms of compactness). Recent experiment at 230 GHz has probed Sgr A* down to a few event-horizon scales (Doeleman et al. 2008). With the improved sensitivity and detection of Sgr A* on more than 3 baselines in the coming years, time-variable structures could be detected using closure quantities (Doeleman et al. 2009b). Table 6.1 lists some telescopes which could be used in a future 1 mm-VLBI array. With the addition of these more and more sensitive and millimeter-capable telescopes, direct imaging of the vicinity of the SMBH in the Galaxy Center and nearby galactic nuclei is realizable in the foreseeable future. With such imaging capabilities, we may expect to detect general relativity effects, which may manifest as time variable image distortions, e.g., for the case of Sgr A*, which is at present the best example of a nearby super massive black hole.

Table 6.1: Properties of existing and proposed radio telescopes suitable for VLBI at $\nu \geq 230$ GHz. Adapted and updated from (Krichbaum et al. 2008).

Station	Location	Country	Altitude [m]	Diameter [m]	Surface [μm]	Eff.	SEFD[a] [Jy]	H-maser
PdB-1	Plateau de Bure	France	2550	15	55	0.45	5182	yes
PdB	Plateau de Bure	France	2550	6×15	55	0.45	864	yes
PV	Pico Veleta	Spain	2900	30	67	0.39	1485	yes
APEX	Chajnantor	Chile	5100	12	18	0.58	6295	yes
HHT	Mt. Graham	AZ, USA	3100	10	15	0.59	8979	yes
KP	Kitt Peak	AZ, USA	2000	12	75	0.35	10322	no
JCMT	Mauna Kea	HI, USA	4100	15	25	0.57	4141	yes[b]
CSO	Mauna Kea	HI, USA	4100	10	25	0.57	8618	yes[b]
SMA	Mauna Kea	HI, USA	4100	8×6	12	0.59	3093	yes
Hawai-6	Mauna Kea	HI, USA	4100	-[c]	25	0.57	1696	yes[b]
CARMA-1	Cedar Flat	CA, USA	2200	10.4	60	0.43	11373	yes
CARMA	Cedar Flat	CA, USA	2200	-[d]	60	0.43	1142	yes
LMT	Sierra Negra	Mexico	4600	50	70	0.38	556	no
ALMA-1	Chajnantor	Chile	5000	12	25	0.57	6469	no
ALMA	Chajnantor	Chile	5000	50×12	25	0.57	129	no

[a] assuming $T_{\text{sys}} = 150$ K

[b] via fiber link to SMA

[c] the phased Hawaii array consists of the combination of SMA + CSO + JCMT

[d] 6×10.4 m + 9×6.1 m

Bibliography

Abdo, A. A., et al. 2009, ApJ, 700, 597

Agudo, I., et al. 2007, A&A, 476, L17

Aharonian, F., & Neronov, A. 2005, ApJ, 619, 306

Aharonian, F., et al. 2006a, Science, 314, 1424

—. 2006b, Physical Review Letters, 97, 221102

—. 2008, A&A, 492, L25

—. 2009, A&A, 503, 817

Aitken, D. K., Greaves, J., Chrysostomou, A., Jenness, T., Holland, W., Hough, J. H., Pierce-Price, D., & Richer, J. 2000, ApJ, 534, L173

Alberdi, A., et al. 1993, A&A, 277, L1

Aller, M. F., Aller, H. D., & Hughes, P. A. 2009, ArXiv e-prints

An, T., Goss, W. M., Zhao, J.-H., Hong, X. Y., Roy, S., Rao, A. P., & Shen, Z.-Q. 2005, ApJ, 634, L49

Antonucci, R. 1993, ARA&A, 31, 473

Antonucci, R. R. J., & Miller, J. S. 1985, ApJ, 297, 621

Armstrong, J. W., Rickett, B. J., & Spangler, S. R. 1995, ApJ, 443, 209

Aschenbach, B., Grosso, N., Porquet, D., & Predehl, P. 2004, A&A, 417, 71

Baade, W. 1956, ApJ, 123, 550

Baade, W., & Minkowski, R. 1954, ApJ, 119, 215

Backer, D. C., & Sramek, R. A. 1982, ApJ, 260, 512

—. 1999, ApJ, 524, 805

Backer, D. C., Zensus, J. A., Kellermann, K. I., Reid, M., Moran, J. M., & Lo, K. Y. 1993, Science, 262, 1414

Baganoff, F. K., et al. 2001, Nature, 413, 45

—. 2003, ApJ, 591, 891

Balick, B., & Brown, R. L. 1974, ApJ, 194, 265

Bevington, P. R., & Robinson, D. K. 2003, Data reduction and error analysis for the physical sciences (Boston, MA: McGraw-Hill: McGraw-Hill)

Bietenholz, M. F., Bartel, N., & Rupen, M. P. 2004, ApJ, 615, 173

Bietenholz, M. F., et al. 1996, ApJ, 457, 604

Blandford, R. D., & Königl, A. 1979, ApJ, 232, 34

Blandford, R. D., & Znajek, R. L. 1977, MNRAS, 179, 433

Bondi, M., et al. 1996, A&A, 308, 415

Bower, G. C., & Backer, D. C. 1998, ApJ, 507, L117

Bower, G. C., Backer, D. C., Wright, M., Forster, J. R., Aller, H. D., & Aller, M. F. 1997, ApJ, 484, 118

Bower, G. C., Backer, D. C., Zhao, J.-H., Goss, M., & Falcke, H. 1999a, ApJ, 521, 582

Bower, G. C., Falcke, H., & Backer, D. C. 1999b, ApJ, 523, L29

Bower, G. C., Falcke, H., Herrnstein, R. M., Zhao, J.-H., Goss, W. M., & Backer, D. C. 2004, Science, 304, 704

Bower, G. C., Falcke, H., Sault, R. J., & Backer, D. C. 2002, ApJ, 571, 843

Bower, G. C., Falcke, H., Wright, M. C., & Backer, D. C. 2005a, ApJ, 618, L29

Bower, G. C., Goss, W. M., Falcke, H., Backer, D. C., & Lithwick, Y. 2006, ApJ, 648, L127

Bower, G. C., Roberts, D. A., Yusef-Zadeh, F., Backer, D. C., Cotton, W. D., Goss, W. M., Lang, C. C., & Lithwick, Y. 2005b, ApJ, 633, 218

Bower, G. C., Wright, M. C. H., Backer, D. C., & Falcke, H. 1999c, ApJ, 527, 851

Bower, G. C., Wright, M. C. H., Falcke, H., & Backer, D. C. 2001, ApJ, 555, L103

—. 2003, ApJ, 588, 331

Bridle, A. H., & Greisen, E. W. 1994, VLBA Scientific Memorandum, 87

Britzen, S., Meyer, V., Witzel, A., Agudo, I., Aller, M. F., Aller, H. D., Eckart, A., & Zensus, J. A. 2006, in Proceedings of the 8th European VLBI Network Symposium

Britzen, S., et al. 2010, ArXiv e-prints

Broderick, A. E., & Loeb, A. 2006, MNRAS, 367, 905

Broderick, A. E., Loeb, A., & Narayan, R. 2009, ApJ, 701, 1357

Bromley, B. C., Melia, F., & Liu, S. 2001, ApJ, 555, L83

Brown, R. L. 1982, ApJ, 262, 110

Brown, R. L., Johnston, K. J., & Lo, K. Y. 1978, AJ, 83, 1594

Brown, R. L., & Lo, K. Y. 1982, ApJ, 253, 108

Brunthaler, A., Bower, G. C., & Falcke, H. 2006, A&A, 451, 845

Brunthaler, A., Bower, G. C., Falcke, H., & Mellon, R. R. 2001, ApJ, 560, L123

Burbidge, G. R. 1956, ApJ, 124, 416

Cai, H., et al. 2007, A&A, 468, 963

Carilli, C. L., Carlstrom, J. E., & Holdaway, M. A. 1999, in Astronomical Society of the Pacific Conference Series, Vol. 180, Synthesis Imaging in Radio Astronomy II, ed. G. B. Taylor, C. L. Carilli, & R. A. Perley, 565

Clegg, A. W., Fiedler, R. L., & Cordes, J. M. 1993, ApJ, 409, 691

Cohen, M. H., Cannon, W., Purcell, G. H., Shaffer, D. B., Broderick, J. J., Kellermann, K. I., & Jauncey, D. L. 1971, ApJ, 170, 207

Cornwell, T. 1995, in Astronomical Society of the Pacific Conference Series, Vol. 82, Very Long Baseline Interferometry and the VLBA, ed. J. A. Zensus, P. J. Diamond, & P. J. Napier, 39

Cornwell, T., & Fomalont, E. B. 1999, in Astronomical Society of the Pacific Conference Series, Vol. 180, Synthesis Imaging in Radio Astronomy II, ed. G. B. Taylor, C. L. Carilli, & R. A. Perley, 187

Cotton, W. D. 1995, in Astronomical Society of the Pacific Conference Series, Vol. 82, Very Long Baseline Interferometry and the VLBA, ed. J. A. Zensus, P. J. Diamond, & P. J. Napier, 189

Davies, R. D., Walsh, D., & Booth, R. S. 1976, MNRAS, 177, 319

Desai, K. M., & Fey, A. L. 2001, ApJS, 133, 395

Dexter, J., Agol, E., & Fragile, P. C. 2009, ApJ, 703, L142

Do, T., Ghez, A. M., Morris, M. R., Yelda, S., Meyer, L., Lu, J. R., Hornstein, S. D., & Matthews, K. 2009, ApJ, 691, 1021

Dodds-Eden, K., et al. 2009, ApJ, 698, 676

Doeleman, S., et al. 2009a, in ArXiv Astrophysics e-prints, Vol. 2010, AGB Stars and Related Phenomenastro2010: The Astronomy and Astrophysics Decadal Survey, 68

Doeleman, S. S., Fish, V. L., Broderick, A. E., Loeb, A., & Rogers, A. E. E. 2009b, ApJ, 695, 59

Doeleman, S. S., et al. 2001, AJ, 121, 2610

—. 2008, Nature, 455, 78

Duschl, W. J., & Lesch, H. 1994, A&A, 286, 431

Eckart, A., & Genzel, R. 1996, Nature, 383, 415

—. 1997, MNRAS, 284, 576

Eckart, A., Genzel, R., Krabbe, A., Hofmann, R., van der Werf, P. P., & Drapatz, S. 1992, Nature, 355, 526

Eckart, A., Genzel, R., Ott, T., & Schödel, R. 2002, MNRAS, 331, 917

Eckart, A., Schödel, R., Meyer, L., Trippe, S., Ott, T., & Genzel, R. 2006a, A&A, 455, 1

Eckart, A., et al. 2004, A&A, 427, 1

—. 2006b, A&A, 450, 535

—. 2008a, Journal of Physics Conference Series, 131, 012002

—. 2008b, A&A, 479, 625

—. 2008c, A&A, 492, 337

Eisenhauer, F., Schödel, R., Genzel, R., Ott, T., Tecza, M., Abuter, R., Eckart, A., & Alexander, T. 2003, ApJ, 597, L121

Eisenhauer, F., et al. 2005, ApJ, 628, 246

Falcke, H. 1999, in Astronomical Society of the Pacific Conference Series, Vol. 186, The Central Parsecs of the Galaxy, ed. H. Falcke, A. Cotera, W. J. Duschl, F. Melia, & M. J. Rieke, 113

Falcke, H., Goss, W. M., Matsuo, H., Teuben, P., Zhao, J., & Zylka, R. 1998, ApJ, 499, 731

Falcke, H., Mannheim, K., & Biermann, P. L. 1993, A&A, 278, L1

Falcke, H., & Markoff, S. 2000, A&A, 362, 113

Falcke, H., Markoff, S., & Bower, G. C. 2009, A&A, 496, 77

Fanaroff, B. L., & Riley, J. M. 1974, MNRAS, 167, 31P

Fender, R., Koerding, E., Belloni, T., Uttley, P., McHardy, I., & Tzioumis, T. 2007, ArXiv e-prints

Fender, R., Rayner, D., Norris, R., Sault, R. J., & Pooley, G. 2000, ApJ, 530, L29

Fender, R. P., Belloni, T. M., & Gallo, E. 2004, MNRAS, 355, 1105

Feng, S., Shen, Z., Cai, H., Chen, X., Lu, R., & Huang, L. 2006, A&A, 456, 97

Fish, V. L., Doeleman, S. S., Broderick, A. E., Loeb, A., & Rogers, A. E. E. 2008, ArXiv e-prints

—. 2009, ApJ, 706, 1353

Fomalont, E. B. 1999, in Astronomical Society of the Pacific Conference Series, Vol. 180, Synthesis Imaging in Radio Astronomy II, ed. G. B. Taylor, C. L. Carilli, & R. A. Perley, 301

Foschini, L., et al. 2006, A&A, 450, 77

Frail, D. A., Diamond, P. J., Cordes, J. M., & van Langevelde, H. J. 1994, ApJ, 427, L43

Gebhardt, K., & Thomas, J. 2009, ApJ, 700, 1690

Genzel, R. 2007, Highlights of Astronomy, 14, 63

Genzel, R., Schödel, R., Ott, T., Eckart, A., Alexander, T., Lacombe, F., Rouan, D., & Aschenbach, B. 2003, Nature, 425, 934

Genzel, R., & Townes, C. H. 1987, ARA&A, 25, 377

Ghez, A. M., Becklin, E., Duchjne, G., Hornstein, S., Morris, M., Salim, S., & Tanner, A. 2003a, Astronomische Nachrichten Supplement, 324, 527

Ghez, A. M., Klein, B. L., Morris, M., & Becklin, E. E. 1998, ApJ, 509, 678

Ghez, A. M., Morris, M., Becklin, E. E., Tanner, A., & Kremenek, T. 2000, Nature, 407, 349

Ghez, A. M., Salim, S., Hornstein, S. D., Tanner, A., Lu, J. R., Morris, M., Becklin, E. E., & Duchêne, G. 2005, ApJ, 620, 744

Ghez, A. M., et al. 2003b, ApJ, 586, L127

—. 2004, ApJ, 601, L159

—. 2008, ApJ, 689, 1044

Gillessen, S., Eisenhauer, F., Trippe, S., Alexander, T., Genzel, R., Martins, F., & Ott, T. 2009, ApJ, 692, 1075

Gillessen, S., et al. 2006, ApJ, 640, L163

Goldwurm, A. 2007, Comptes Rendus Physique, 8, 35

Goldwurm, A., Brion, E., Goldoni, P., Ferrando, P., Daigne, F., Decourchelle, A., Warwick, R. S., & Predehl, P. 2003, ApJ, 584, 751

Gomez, J. L., Alberdi, A., & Marcaide, J. M. 1994, A&A, 284, 51

Goss, W. M., Brown, R. L., & Lo, K. Y. 2003, Astronomische Nachrichten Supplement, 324, 497

Gwinn, C. R., Danen, R. M., Tran, T. K., Middleditch, J., & Ozernoy, L. M. 1991, ApJ, 381, L43

Gwinn, C. R., Moran, J. M., Reid, M. J., & Schneps, M. H. 1988, ApJ, 330, 817

Hardee, P. E. 1987, ApJ, 318, 78

Heeschen, D. S., Krichbaum, T., Schalinski, C. J., & Witzel, A. 1987, AJ, 94, 1493

Herrnstein, J. R., et al. 1999, Nature, 400, 539

Herrnstein, R. M., Zhao, J., Bower, G. C., & Goss, W. M. 2004, AJ, 127, 3399

Hirabayashi, H., et al. 1998, Science, 281, 1825

Högbom, J. A. 1974, A&AS, 15, 417

Homan, D. C., Kadler, M., Kellermann, K. I., Kovalev, Y. Y., Lister, M. L., Ros, E., Savolainen, T., & Zensus, J. A. 2009, ApJ, 706, 1253

Homan, D. C., & Lister, M. L. 2006, AJ, 131, 1262

Homan, D. C., & Wardle, J. F. C. 1999, AJ, 118, 1942

Hong, X., Sun, C., Zhao, J., Jiang, D., Shen, Z., An, T., Wang, W., & Yang, J. 2008, Chinese Journal of Astronomy and Astrophysics, 8, 179

Hong, X. Y., Venturi, T., Wan, T. S., Jiang, D. R., Shen, Z., Liu, X., Nicolson, G., & Umana, G. 1999, A&AS, 134, 201

Hong, X. Y., Zhao, J. H., An, T., Jiang, D. R., Wang, H., Feng, W. X., & Sun, C. H. 2004, in European VLBI Network on New Developments in VLBI Science and Technology, ed. R. Bachiller, F. Colomer, J.-F. Desmurs, & P. de Vicente, 77–80

Hornstein, S. D., Matthews, K., Ghez, A. M., Lu, J. R., Morris, M., Becklin, E. E., Rafelski, M., & Baganoff, F. K. 2007, ApJ, 667, 900

Hoyle, F., & Fowler, W. A. 1963, MNRAS, 125, 169

Huang, L., Cai, M., Shen, Z.-Q., & Yuan, F. 2007, MNRAS, 379, 833

Huang, L., Liu, S., Shen, Z.-Q., Yuan, Y.-F., Cai, M. J., Li, H., & Fryer, C. L. 2009a, ApJ, 703, 557

Huang, L., Takahashi, R., & Shen, Z. 2009b, ApJ, 706, 960

J. Franco & A. Carraminana, ed. 1999, Interstellar Turbulence, Proceedings of the 2nd Guillermo Haro Conference, ed. J. Franco & A. Carraminana

Jauncey, D. L., et al. 1989, AJ, 98, 44

Jenness, T., Robson, E. I., & Stevens, J. A. 2009, MNRAS, 1762

Jennison, R. C. 1958, MNRAS, 118, 276

Jorstad, S. G., Marscher, A. P., Mattox, J. R., Wehrle, A. E., Bloom, S. D., & Yurchenko, A. V. 2001, ApJS, 134, 181

Junkkarinen, V. 1984, PASP, 96, 539

Kellermann, K. I., & Moran, J. M. 2001, ARA&A, 39, 457

Kellermann, K. I., & Pauliny-Toth, I. I. K. 1969, ApJ, 155, L71

—. 1981, ARA&A, 19, 373

Kellermann, K. I., Sramek, R., Schmidt, M., Shaffer, D. B., & Green, R. 1989, AJ, 98, 1195

Khachikian, E. Y., & Weedman, D. W. 1974, ApJ, 192, 581

Konigl, A. 1981, ApJ, 243, 700

Kovalev, Y. Y., Lobanov, A. P., Pushkarev, A. B., & Zensus, J. A. 2008, A&A, 483, 759

Kraus, A., et al. 2003, A&A, 401, 161

Krichbaum, T., Witzel, A., & Zensus, J. A. 2000, in EVN Symposium 2000, Proceedings of the 5th european VLBI Network Symposium, ed. J. E. Conway, A. G. Polatidis, R. S. Booth, & Y. M. Pihlström , 25

Krichbaum, T. P. 1996, in Science with Large Millimetre Arrays, ed. P. A. Shaver, 95

Krichbaum, T. P., Alef, W., Witzel, A., Zensus, J. A., Booth, R. S., Greve, A., & Rogers, A. E. E. 1998a, A&A, 329, 873

Krichbaum, T. P., Graham, D. A., Bremer, M., Alef, W., Witzel, A., Zensus, J. A., & Eckart, A. 2006, Journal of Physics Conference Series, 54, 328

Krichbaum, T. P., Witzel, A., Standke, K. J., Graham, D. A., Schalinski, C. J., & Zensus, J. A. 1994, in Compact Extragalactic Radio Sources, ed. J. A. Zensus & K. I. Kellermann, 39

Krichbaum, T. P., et al. 1993, A&A, 274, L37

—. 1998b, A&A, 335, L106

—. 1998c, A&A, 335, L106

—. 2008, ArXiv e-prints

Kunneriath, D., et al. 2010, A&A, accepted

Laor, A. 2000, ApJ, 543, L111

Lazio, T. J. W. 2004, ApJ, 613, 1023

Lazio, T. J. W., & Cordes, J. M. 1998, ApJ, 505, 715

Lazio, T. J. W., & Fey, A. L. 2001, ApJ, 560, 698

Lee, S., Lobanov, A. P., Krichbaum, T. P., Witzel, A., Zensus, A., Bremer, M., Greve, A., & Grewing, M. 2008, AJ, 136, 159

Leppänen, K. J. 1993, VLBA Scientific Memorandum, 1

Li, J., Shen, Z., Miyazaki, A., Huang, L., Sault, R. J., Miyoshi, M., Tsuboi, M., & Tsutsumi, T. 2009, ApJ, 700, 417

Li, J., Shen, Z.-Q., Miyazaki, A., Huang, L., Sault, R. J., Miyoshi, M., Tsuboi, M., & Tsutsumi, T. 2008, Journal of Physics Conference Series, 131, 012007

Lind, K. R., & Blandford, R. D. 1985, ApJ, 295, 358

Liu, S., Melia, F., & Petrosian, V. 2006a, ApJ, 636, 798

Liu, S., Petrosian, V., & Melia, F. 2004, ApJ, 611, L101

Liu, Y., Jiang, D. R., & Gu, M. F. 2006b, ApJ, 637, 669

Lo, K. Y., Backer, D. C., Ekers, R. D., Kellermann, K. I., Reid, M., & Moran, J. M. 1985, Nature, 315, 124

Lo, K. Y., Backer, D. C., Kellermann, K. I., Reid, M., Zhao, J. H., Goss, W. M., & Moran, J. M. 1993, Nature, 362, 38

Lo, K. Y., Shen, Z.-Q., Zhao, J.-H., & Ho, P. T. P. 1998, ApJ, 508, L61

Lobanov, A. 2007, Imaging Across the Spectrum: Synergies Between SKA and Other Future Telescopes (Springer-Verlag), 39

Lobanov, A. P. 1998, A&A, 330, 79

Lu, R., Krichbaum, T. P., Eckart, A., König, S., Kunneriath, D., Witzel, G., Witzel, A., & Zensus, J. A. 2008, Journal of Physics Conference Series, 131, 012059

Lynden-Bell, D. 1969, Nature, 223, 690

Lynden-Bell, D., & Rees, M. J. 1971, MNRAS, 152, 461

Macquart, J.-P., & Bower, G. C. 2006, ApJ, 641, 302

Macquart, J.-P., Kedziora-Chudczer, L., Rayner, D. P., & Jauncey, D. L. 2000, ApJ, 538, 623

Macquart, J.-P., Wu, K., Sault, R. J., & Hannikainen, D. C. 2002, A&A, 396, 615

Marcaide, J. M., Alberdi, A., Lara, L., Pérez-Torres, M. A., & Diamond, P. J. 1999, A&A, 343, 801

Marcaide, J. M., et al. 1992, A&A, 258, 295

Markoff, S., Bower, G. C., & Falcke, H. 2007, MNRAS, 379, 1519

Markoff, S., Falcke, H., Yuan, F., & Biermann, P. L. 2001, A&A, 379, L13

Marrone, D. P., Moran, J. M., Zhao, J., & Rao, R. 2006a, Journal of Physics Conference Series, 54, 354

Marrone, D. P., Moran, J. M., Zhao, J.-H., & Rao, R. 2006b, ApJ, 640, 308

—. 2007, ApJ, 654, L57

Marrone, D. P., et al. 2008, ApJ, 682, 373

Marscher, A. P. 1983, ApJ, 264, 296

Mauerhan, J. C., Morris, M., Walter, F., & Baganoff, F. K. 2005, ApJ, 623, L25

Mayer-Hasselwander, H. A., et al. 1998, A&A, 335, 161

Melia, F. 1994, ApJ, 426, 577

Melia, F., Bromley, B. C., Liu, S., & Walker, C. K. 2001, ApJ, 554, L37

Melia, F., & Falcke, H. 2001, ARA&A, 39, 309

Meyer, L., Do, T., Ghez, A., Morris, M. R., Witzel, G., Eckart, A., Bélanger, G., & Schödel, R. 2008, ApJ, 688, L17

Meyer, L., Eckart, A., Schödel, R., Duschl, W. J., Mužić, K., Dovčiak, M., & Karas, V. 2006a, A&A, 460, 15

Meyer, L., Schödel, R., Eckart, A., Karas, V., Dovčiak, M., & Duschl, W. J. 2006b, A&A, 458, L25

Middelberg, E., Roy, A. L., Walker, R. C., & Falcke, H. 2005, A&A, 433, 897

Miyazaki, A., Tsutsumi, T., Miyoshi, M., Tsuboi, M., & Shen, Z.-Q. 2005, ArXiv Astrophysics e-prints

Miyazaki, A., Tsutsumi, T., & Tsuboi, M. 2004, ApJ, 611, L97

Miyoshi, M., & Kameno, S. 2002, in International VLBI Service for Geodesy and Astrometry General Meeting Proceeding, p. 199, 199

Miyoshi, M., Moran, J., Herrnstein, J., Greenhill, L., Nakai, N., Diamond, P., & Inoue, M. 1995, Nature, 373, 127

Molnar, L. A., Mutel, R. L., Reid, M. J., & Johnston, K. J. 1995, ApJ, 438, 708

Monnier, J. D. 2007, New Astronomy Review, 51, 604

Moran, J. M., & Dhawan, V. 1995, in Astronomical Society of the Pacific Conference Series, Vol. 82, Very Long Baseline Interferometry and the VLBA, ed. J. A. Zensus, P. J. Diamond, & P. J. Napier, 161

Moran, J. M., Rodriguez, L. F., Greene, B., & Backer, D. C. 1990, ApJ, 348, 147

Morris, M., & Serabyn, E. 1996, ARA&A, 34, 645

Mukherjee, R., et al. 1997, ApJ, 490, 116

Narayan, R., & Hubbard, W. B. 1988, ApJ, 325, 503

Narayan, R., Mahadevan, R., Grindlay, J. E., Popham, R. G., & Gammie, C. 1998, ApJ, 492, 554

Narayan, R., Yi, I., & Mahadevan, R. 1995, Nature, 374, 623

Nishiyama, S., Tamura, M., Hatano, H., Nagata, T., Kudo, T., Ishii, M., Schödel, R., & Eckart, A. 2009, ApJ, 702, L56

Nord, M. E., Lazio, T. J. W., Kassim, N. E., Goss, W. M., & Duric, N. 2004, ApJ, 601, L51

O'Sullivan, S. P., & Gabuzda, D. C. 2009, MNRAS, 400, 26

Özel, F., Psaltis, D., & Narayan, R. 2000, ApJ, 541, 234

Pacholczyk, A. G. 1970, Radio astrophysics. Nonthermal processes in galactic and extragalactic sources (ed. San Francisco: Freeman)

Pearson, T. J., & Readhead, A. C. S. 1984, ARA&A, 22, 97

Porcas, R. W., & Rioja, M. J. 2002, in Proceedings of the 6th EVN Symposium, ed. E. Ros, R. W. Porcas, A. P. Lobanov, & J. A. Zensus, 65

Porquet, D., Predehl, P., Aschenbach, B., Grosso, N., Goldwurm, A., Goldoni, P., Warwick, R. S., & Decourchelle, A. 2003, A&A, 407, L17

Porquet, D., et al. 2008, A&A, 488, 549

Qian, S., Zhang, X., Krichbaum, T. P., Kraus, A., Witzel, A., & Zensus, J. A. 2001, Chinese Journal of Astronomy and Astrophysics, 1, 296

Quataert, E. 2002, ApJ, 575, 855

Rayner, D. P., Norris, R. P., & Sault, R. J. 2000, MNRAS, 319, 484

Readhead, A. C. S. 1994, ApJ, 426, 51

Readhead, A. C. S., Walker, R. C., Pearson, T. J., & Cohen, M. H. 1980, Nature, 285, 137

Readhead, A. C. S., et al. 1983, Nature, 303, 504

Rees, M. J. 1966, Nature, 211, 468

Reid, M. J., Broderick, A. E., Loeb, A., Honma, M., & Brunthaler, A. 2008, ApJ, 682, 1041

Reid, M. J., & Brunthaler, A. 2004, ApJ, 616, 872

Reid, M. J., Menten, K. M., Trippe, S., Ott, T., & Genzel, R. 2007, ApJ, 659, 378

Reid, M. J., Readhead, A. C. S., Vermeulen, R. C., & Treuhaft, R. N. 1999, ApJ, 524, 816

Reid, M. J., et al. 2009, ApJ, 700, 137

Reynolds, S. P., & McKee, C. F. 1980, ApJ, 239, 893

Rickett, B. J. 1990, ARA&A, 28, 561

Rogers, A. E. E., Doeleman, S. S., & Moran, J. M. 1995a, AJ, 109, 1391

Rogers, A. E. E., Moffet, A. T., Backer, D. C., & Moran, J. M. 1984, Radio Science, 19, 1552

Rogers, A. E. E., Phillips, R. B., & Lonsdale, C. J. 1995b, in Bulletin of the American Astronomical Society, Vol. 27, Bulletin of the American Astronomical Society, 1300

Rogers, A. E. E., et al. 1994, ApJ, 434, L59

Roland, J., Britzen, S., Kudryavtseva, N. A., Witzel, A., & Karouzos, M. 2008, A&A, 483, 125

Romani, R. W., Narayan, R., & Blandford, R. 1986, MNRAS, 220, 19

Romney, J., et al. 1984, A&A, 135, 289

Roy, A. L., Rottmann, H., Teuber, U., & Keller, R. 2007, ArXiv Astrophysics e-prints

Roy, S., & Pramesh Rao, A. 2003, Astronomische Nachrichten Supplement, 324, 391

Rybicki, G. B., & Lightman, A. P. 1979, Radiative processes in astrophysics (New York, Wiley-Interscience, 1979. 393 p.)

Salow, R. M., & Statler, T. S. 2004, ApJ, 611, 245

Salpeter, E. E. 1964, ApJ, 140, 796

Sault, R. J., & Macquart, J.-P. 1999, ApJ, 526, L85

Schmidt, M. 1963, Nature, 197, 1040

Schödel, R., et al. 2002, Nature, 419, 694

Serabyn, E., Carlstrom, J., Lay, O., Lis, D. C., Hunter, T. R., & Lacy, J. H. 1997, ApJ, 490, L77

Seyfert, C. K. 1943, ApJ, 97, 28

Shen, Z., Liang, M. C., Lo, K. Y., & Miyoshi, M. 2003, Astronomische Nachrichten Supplement, 324, 383

Shen, Z., et al. 1997, AJ, 114, 1999

Shen, Z.-Q. 2006, Journal of Physics Conference Series, 54, 377

Shen, Z.-Q., Lo, K. Y., Liang, M.-C., Ho, P. T. P., & Zhao, J.-H. 2005, Nature, 438, 62

Shepherd, M. C. 1997, in Astronomical Society of the Pacific Conference Series, Vol. 125, Astronomical Data Analysis Software and Systems VI, ed. G. Hunt & H. Payne, 77

Spangler, S. R., & Cordes, J. M. 1988, ApJ, 332, 346

Stirling, A. M., et al. 2003, MNRAS, 341, 405

The HESS Collaboration. 2009, ArXiv e-prints

Thompson, A. R., Moran, J. M., & Swenson, Jr., G. W. 2001, Interferometry and Synthesis in Radio Astronomy, 2nd Edition (New York: Wiley)

Thorne, K. S. 1974, ApJ, 191, 507

Trippe, S., Paumard, T., Ott, T., Gillessen, S., Eisenhauer, F., Martins, F., & Genzel, R. 2007, MNRAS, 375, 764

Trotter, A. S., Moran, J. M., & Rodriguez, L. F. 1998, ApJ, 493, 666

Tsuboi, M. 2008, Journal of Physics Conference Series, 131, 012048

Tsuboi, M., Miyazaki, A., & Tsutsumi, T. 1999, in Astronomical Society of the Pacific Conference Series, Vol. 186, The Central Parsecs of the Galaxy, ed. H. Falcke, A. Cotera, W. J. Duschl, F. Melia, & M. J. Rieke, 105

Urry, C. M., & Padovani, P. 1995, PASP, 107, 803

van der Laan, H. 1966, Nature, 211, 1131

van Langevelde, H. J., Frail, D. A., Cordes, J. M., & Diamond, P. J. 1992, ApJ, 396, 686

Vitrishchak, V. M., Gabuzda, D. C., Algaba, J. C., Rastorgueva, E. A., O'Sullivan, S. P., & O'Dowd, A. 2008, MNRAS, 391, 124

Wardle, J. F. C., & Homan, D. C. 2003, Ap&SS, 288, 143

Wardle, J. F. C., Homan, D. C., Ojha, R., & Roberts, D. H. 1998, Nature, 395, 457

Webb, J. R., Smith, A. G., Leacock, R. J., Fitzgibbons, G. L., Gombola, P. P., & Shepherd, D. W. 1988, AJ, 95, 374

Whitney, A. R., et al. 1971, Science, 173, 225

Wilkinson, P. N., Narayan, R., & Spencer, R. E. 1994, MNRAS, 269, 67

Yuan, F., Markoff, S., & Falcke, H. 2002, A&A, 383, 854

Yuan, F., Quataert, E., & Narayan, R. 2003, ApJ, 598, 301

—. 2004, ApJ, 606, 894

Yuan, F., Shen, Z., & Huang, L. 2006, ApJ, 642, L45

Yusef-Zadeh, F., Cotton, W., Wardle, M., Melia, F., & Roberts, D. A. 1994, ApJ, 434, L63

Yusef-Zadeh, F., Roberts, D., Wardle, M., Heinke, C. O., & Bower, G. C. 2006a, ApJ, 650, 189

Yusef-Zadeh, F., Wardle, M., Cotton, W. D., Heinke, C. O., & Roberts, D. A. 2007, ApJ, 668, L47

Yusef-Zadeh, F., Wardle, M., Heinke, C., Dowell, C. D., Roberts, D., Baganoff, F. K., & Cotton, W. 2008, ApJ, 682, 361

Yusef-Zadeh, F., et al. 2006b, ApJ, 644, 198

—. 2009, ApJ, 706, 348

Zamaninasab, M., et al. 2010, A&A, 510, A3

Zel'Dovich, Y. B., & Novikov, I. D. 1965, Soviet Physics Doklady, 9, 834

Zensus, J. A. 1997, ARA&A, 35, 607

Zensus, J. A., Diamond, P. J., & Napier, P. J., eds. 1995, Astronomical Society of the Pacific Conference Series, Vol. 82, Very Long Baseline Interferometry and the VLBA (San Francisco: ASP)

Zhao, J., Bower, G. C., & Goss, W. M. 2001, ApJ, 547, L29

Zhao, J., Ekers, R. D., Goss, W. M., Lo, K. Y., & Narayan, R. 1989, in IAU Symposium, Vol. 136, The Center of the Galaxy, ed. M. Morris, 535

Zhao, J., Goss, W. M., Lo, K., & Ekers, R. D. 1992, in Astronomical Society of the Pacific Conference Series, Vol. 31, Relationships Between Active Galactic Nuclei and Starburst Galaxies, ed. A. V. Filippenko, 295

Zhao, J., Young, K. H., Herrnstein, R. M., Ho, P. T. P., Tsutsumi, T., Lo, K. Y., Goss, W. M., & Bower, G. C. 2003, ApJ, 586, L29

Zhao, J.-H., Herrnstein, R. M., Bower, G. C., Goss, W. M., & Liu, S. M. 2004, ApJ, 603, L85

7 Appendix-A

Statistical analysis   Here we summarize some basic parameters used for variability studies of an observable. More details can be found in e.g., Bevington & Robinson (2003). Let x_i be the ith individual measurement with error σ_i. The weighted mean $\bar{x}$ and the standard deviation σ are given by:

$$\bar{x} = \frac{\sum\limits_{i=1}^{n} \frac{1}{\sigma_i^2} \cdot x_i}{\sum\limits_{i=1}^{n} \frac{1}{\sigma_i^2}}, \tag{7.1}$$

and

$$\sigma = \sqrt{\frac{n}{n-1} \cdot \frac{\sum\limits_{i=1}^{n} \frac{1}{\sigma_i^2} \cdot (x_i - \bar{x})^2}{\sum\limits_{i=1}^{n} \frac{1}{\sigma_i^2}}}, \tag{7.2}$$

where n is the number of measurements.

Modulation Index m is defined as the standard deviation σ normalized by its mean $\bar{x}$, which describes the strength of the observed variability:

$$m[\%] = 100 \cdot \frac{\sigma}{\bar{x}}. \tag{7.3}$$

Variability Amplitude Y is defined as:

$$Y = 3 \times \sqrt{m^2 - m_0^2}, \tag{7.4}$$

where m_0 is the modulation index of the secondary calibrator. Y corresponds to a $3\,\sigma$ variability amplitude, from which systematic variations m_0, which are still seen in the calibrator, are subtracted (Heeschen et al. 1987).

χ^2**-test** is used in our analysis to test the hypothesis of stationarity of an observable. The fit of a constant function $\bar{x}$ to the data follows:

$$\chi^2 = \sum_{i=1}^{n} \frac{1}{\sigma_i^2} \cdot (x_i - \bar{x})^2.$$

(7.5)

Normally, it is convenient to use the reduced chi-square (χ_ν^2) as a measure of goodness of fit, which is simply the χ^2 divided by the number of degrees of freedom (here $n-1$). The χ_ν^2 is an estimate of the ratio of the "estimated variance of the fit" to the parent variance of the data. When the fitting function accurately predicts the means of the parent distribution, the estimated variance should agree well with the variance of the parent distribution and their ratio should be close to unity (Bevington & Robinson 2003). According to the χ^2 probability distribution, one determines the probability that a constant function is a good fit of the data. In intra-day variability (IDV) studies, sources are usually considered to be variable when the the probability that they can be fitted by a constant function is $\leq 0.1\,\%$ (Kraus et al. 2003, and references therein).

8 Appendix-B

We show in this appendix the clean images of Sgr A* at 22, 43, and 86 GHz along with model-fitting results obtained during the 10-day campaign.

8.1 (1): 22 GHz, 2007/05/15   8.1 (2): 22 GHz, 2007/05/16
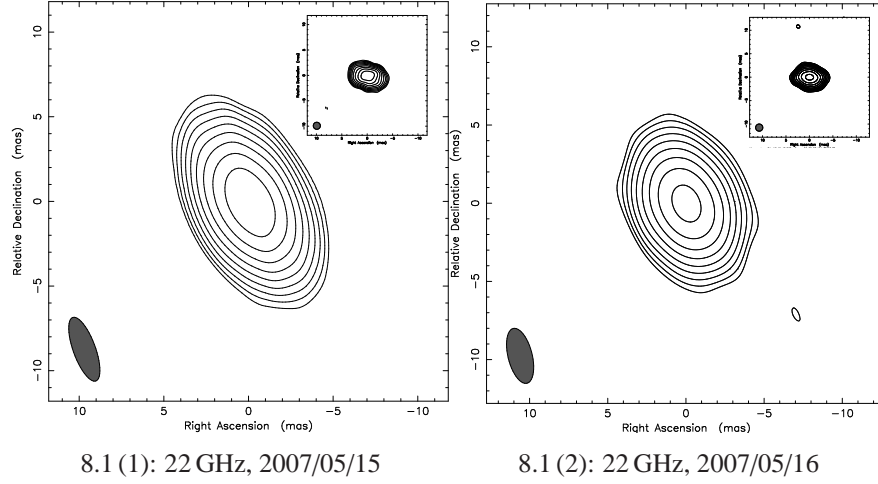
Figure 8.1: Uniformly weighted VLBA images of Sgr A* between May 15 and May 24, 2007 at 22 , 43 and 86 GHz . For each image, the inset shows a slightly super-resolved image restored with a circular beam corresponding to the minor axis of the elliptical beam (shown as an ellipse in the lower-left corner) of the image. The parameters of the images are listed in Table 8.1.
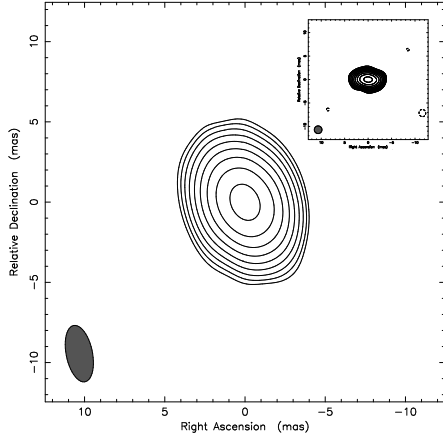
8.1 (3): 22 GHz, 2007/05/17
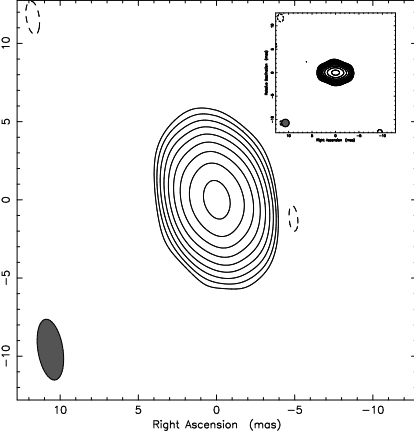
8.1 (4): 22 GHz, 2007/05/18
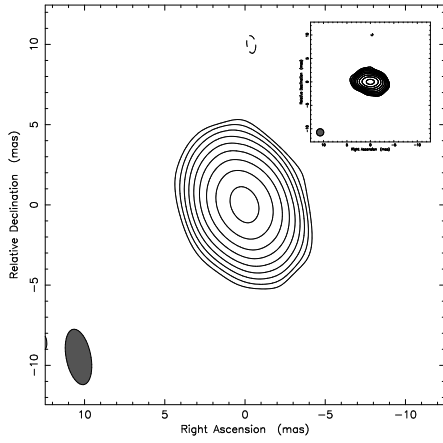
8.1 (5): 22 GHz, 2007/05/19
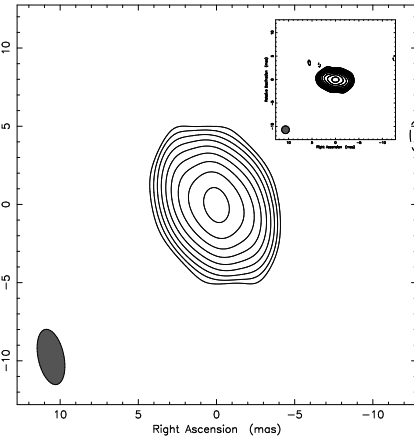
8.1 (6): 22 GHz, 2007/05/20
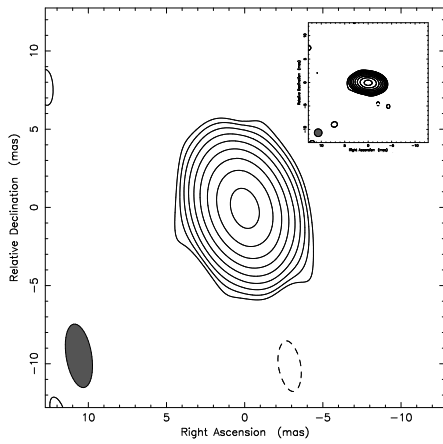
8.1 (7): 22 GHz, 2007/05/21
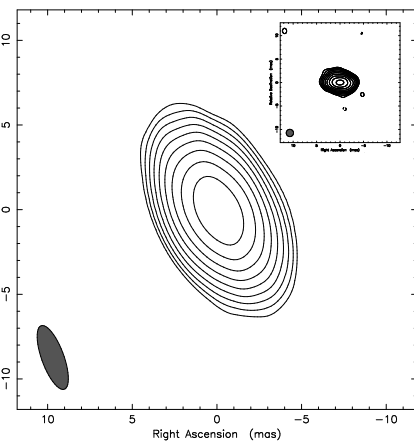
8.1 (8): 22 GHz, 2007/05/22

Figure 8.1: *-continued.*
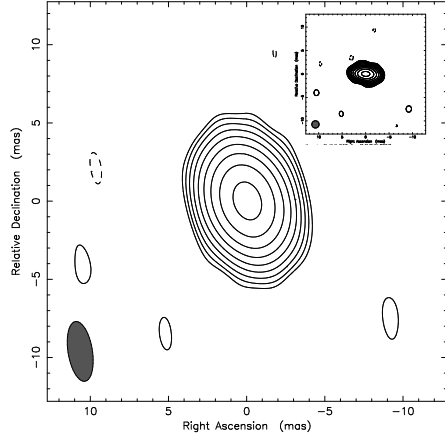
8.1 (9): 22 GHz, 2007/05/23
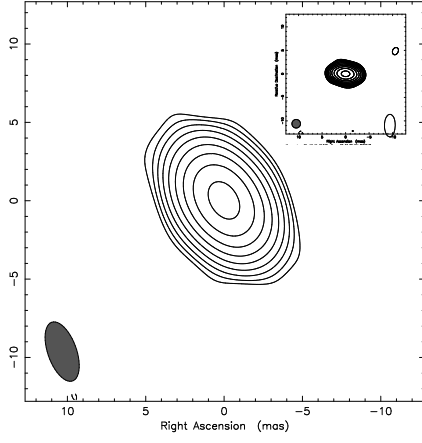
8.0 (10): 22 GHz, 2007/05/24
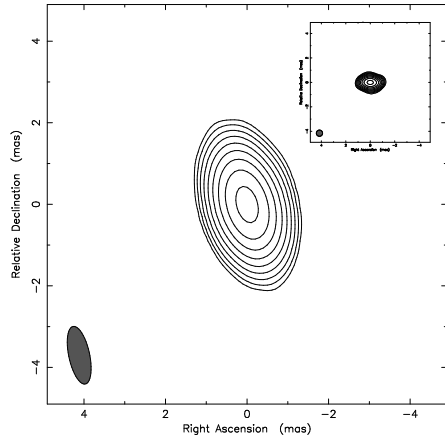
8.0 (11): 43 GHz, 2007/05/15
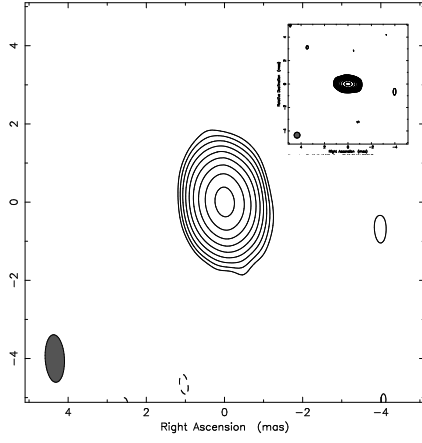
8.0 (12): 43 GHz, 2007/05/16
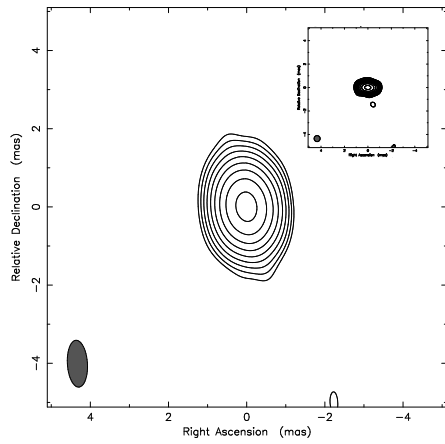
8.0 (13): 43 GHz, 2007/05/17
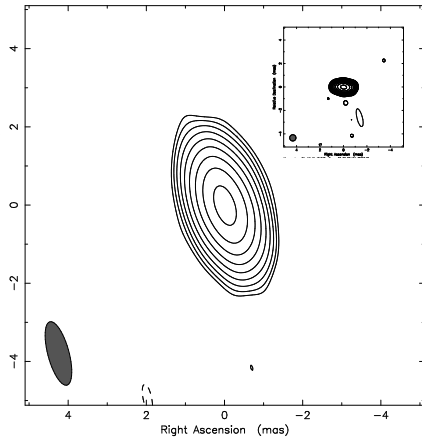
8.0 (14): 43 GHz, 2007/05/18

Figure 8.0: *-continued.*
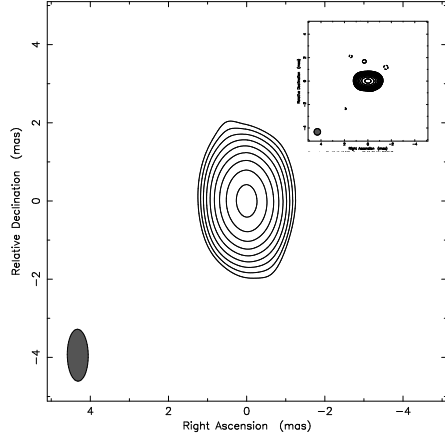
8.0 (15): 43 GHz, 2007/05/19
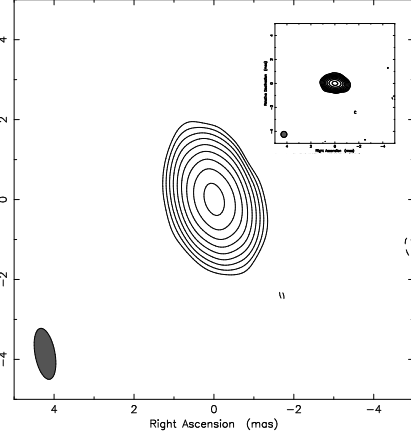
8.0 (16): 43 GHz, 2007/05/20
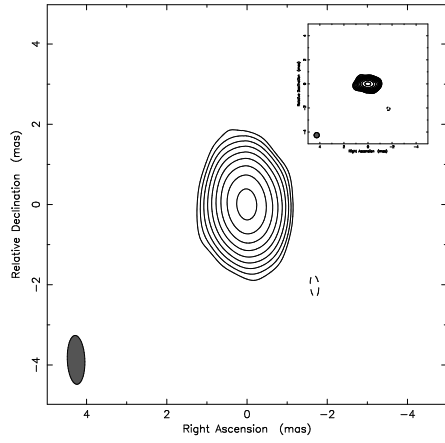
8.0 (17): 43 GHz, 2007/05/21
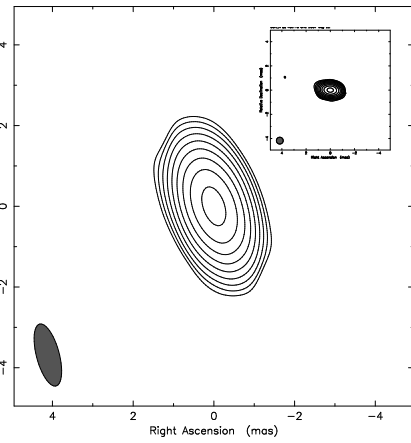
8.0 (18): 43 GHz, 2007/05/22
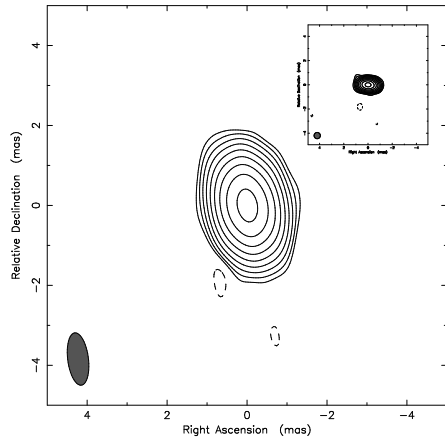
8.0 (19): 43 GHz, 2007/05/23
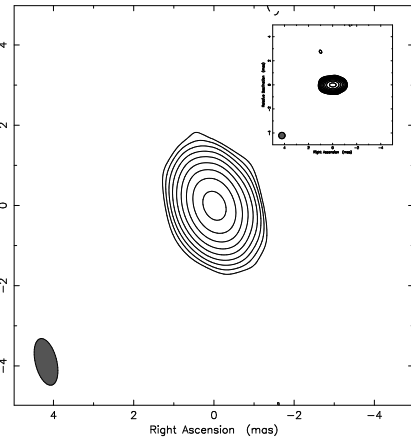
8.0 (20): 43 GHz, 2007/05/24

Figure 8.0: *-continued.*
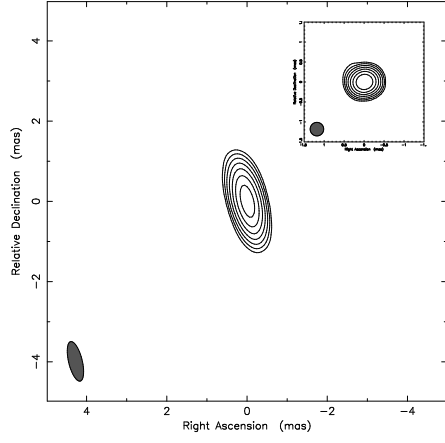
8.0 (21): 86 GHz, 2007/05/15
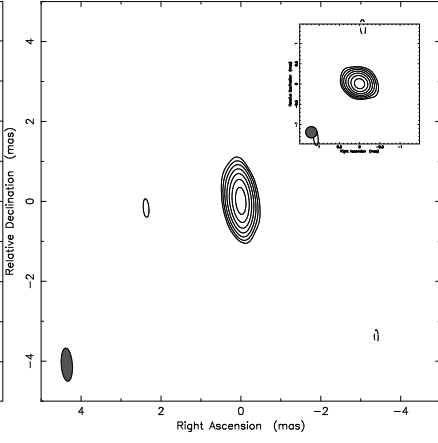
8.0 (22): 86 GHz, 2007/05/16
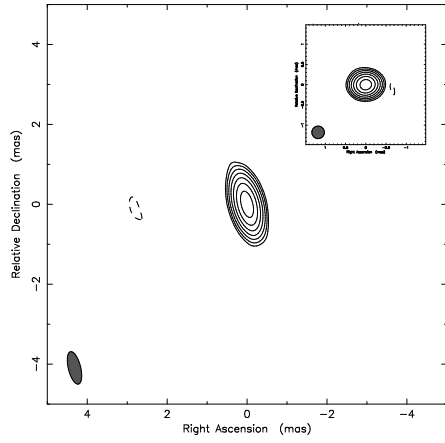
8.0 (23): 86 GHz, 2007/05/17
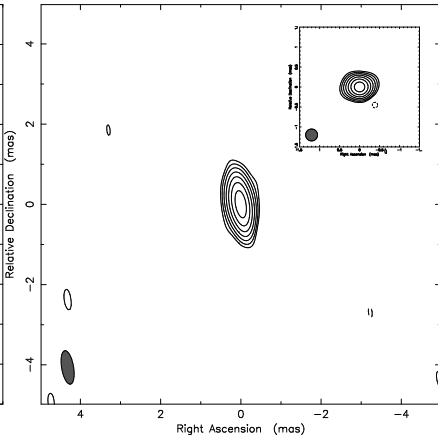
8.0 (24): 86 GHz, 2007/05/18
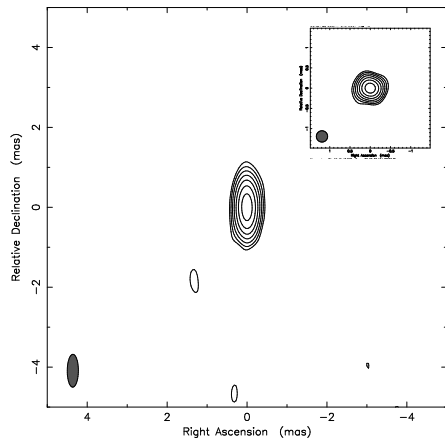
8.0 (25): 86 GHz, 2007/05/19
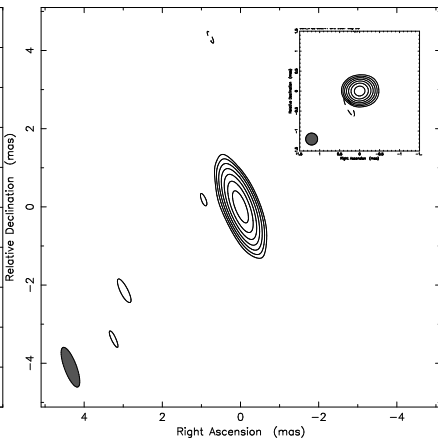
8.0 (26): 86 GHz, 2007/05/20

Figure 8.0: *-continued.*

8.0 (27): 86 GHz, 2007/05/21

8.0 (28): 86 GHz, 2007/05/22

8.0 (29): 86 GHz, 2007/05/23

8.0 (30): 86 GHz, 2007/05/24
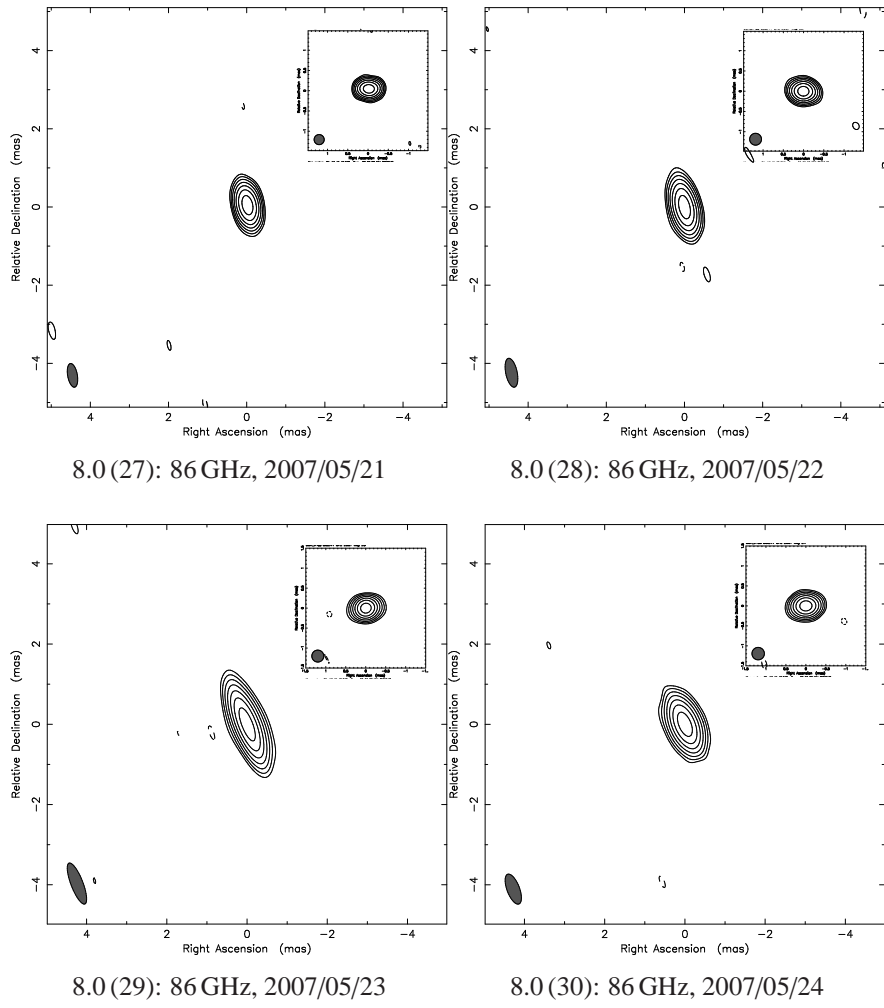
Figure 8.0: *-continued.*

Table 8.1: Description of VLBA images of Sgr A* shown in Figure 8.1.

| Epoch	ν	S_{peak}	Restoring Beam			Contours
			Major	Minor	P.A.	
	GHz	Jy/beam	mas	mas	deg	
(1)	(2)	(3)	(4)	(5)	(6)	(7)
2007/05/15	22	0.653 (0.456)	4	1.31	20.1	0.2, 0.4, 0.8, ..., 51.2
	43	1.20(1.08)	1.44	1.51	12.1	0.3, 0.6, 1.2, ..., 76.8
	86	2.98(2.89)	1.01	0.34	13.7	1, 2, 4, ..., 64
2007/05/16	22	0.567(0.448)	3.61	1.54	14.1	−0.3, 0.3, 0.6, ..., 76.8
	43	1.0 (0.98)	1.22	0.49	3.3	−0.3, 0.3, 0.6, ..., 76.8
	86	2.48 (2.26)	0.83	0.28	4.0	−1, 1, 2, ..., 64
2007/05/17	22	0.777(0.701)	3.58	1.64	11.5	−0.3, 0.3, 0.6, ..., 76.8
	43	1.16 (1.1)	1.20	0.51	3.6	−0.3, 0.3, 0.6, ..., 76.8
	86	3.27 (3.21)	0.83	0.31	14.0	−1, 1, 2, ..., 64
2007/05/18	22	0.649(0.584)	3.93	1.60	9.2	−0.3, 0.3, 0.6, ..., 76.8
	43	0.934(0.885)	1.68	0.54	15.1	−0.3, 0.3, 0.6, ..., 76.8
	86	2.45 (2.41)	0.85	0.30	9.6	−1, 1, 2, ..., 64
2007/05/19	22	0.676(0.589)	3.61	1.54	10.1	−0.3, 0.3, 0.6, ..., 76.8
	43	1.08 (1.07)	1.33	0.54	0.8	−0.3, 0.3, 0.6, ..., 76.8
	86	3.01 (2.75)	0.82	0.28	-0.4	−1, 1, 2, ..., 64
2007/05/20	22	0.608(0.563)	3.60	1.65	12.0	−0.3, 0.3, 0.6, ..., 76.8
	43	0.926(0.851)	1.30	0.50	10.5	−0.3, 0.3, 0.6, ..., 76.8
	86	2.73 (2.66)	1.09	0.30	19.8	−1, 1, 2, ..., 64
2007/05/21	22	0.71 (0.645)	4.11	1.64	9.2	−0.3, 0.3, 0.6, ..., 76.8
	43	1.0 (0.886)	1.22	0.44	2.3	−0.3, 0.3, 0.6, ..., 76.8
	86	3.03 (2.90)	0.62	0.25	10.2	−1, 1, 2, ..., 64
2007/05/22	22	0.67 (0.599)	3.97	1.56	11.6	−0.3, 0.3, 0.6, ..., 76.8
	43	1.19 (1.14)	1.22	0.44	2.3	0.3, 0.3, 0.6, ..., 76.8
	86	3.10 (3.04)	0.75	0.29	11.9	−1(1), 1(2), 2(4), ..., 64
2007/05/23	22	0.685(0.623)	3.87	1.56	11.0	−0.3, 0.3, 0.6, ..., 76.8
	43	1.07 (1.0)	1.32	0.52	7.3	−0.3, 0.3, 0.6, ..., 76.8
	86	2.84 (2.78)	1.09	0.30	21.2	−1, 1, 2, ..., 64
2007/05/24	22	0.767 (0.707)	3.98	1.83	19.6	−0.3, 0.6, 1.2, ..., 76.8

			Restoring Beam			
Epoch	ν	S_{peak}	Major	Minor	P.A.	Contours
	GHz	Jy/beam	mas	mas	deg	
(1)	(2)	(3)	(4)	(5)	(6)	(7)
	43	1.09 (1.07)	1.19	0.54	13.9	−0.3, 0.6, 1.2, ..., 76.8
	86	2.37 (2.31)	0.79	0.31	20.9	−1, 1, 2, ..., 64

Notes: (1) Epoch, (2) Observing frequency, (3) Peak flux density, the numbers in brackets correspond to the peak intensity of images in the inset of each map in Figure 8.1, (4), (5), (6) Parameters of the restoring elliptical Gaussian beam: the full width at half maximum (FWHM) of the major and minor axes and the position angle (P.A.) of the major axis, (7) Contour levels of the image, expressed as a percentage of the peak intensity. Numbers in brackets are for the super-resolved map shown in the inset of the corresponding map in Figure 8.1.

Table 8.2: Results from the modeling of the VLBA observations of Sgr A*.

Date	ν	S	θ_{major}	Ratio	P.A.
	[GHz]	[Jy]	[mas]		[deg]
May 15	22.2	1.51±0.02	2.56±0.03	0.59±0.04	78.6±1.7
	43.1	2.02±0.09	0.71±0.01	0.58±0.06	81.7±2.3
	86.2	4.06±0.57	0.25±0.02	0.68±0.08	79.8±8.0
May 16	22.2	1.18±0.02	2.55±0.06	0.50±0.03	82.0±1.1
	43.1	1.59±0.07	0.72±0.01	0.53±0.04	82.1±0.8
	86.2	2.89±0.83	0.19±0.01	1.00	-
May 17	22.2	1.52±0.03	2.55±0.04	0.63±0.05	78.0±1.7
	43.1	1.99±0.06	0.72±0.01	0.62±0.05	82.0±2.4
	86.2	3.96±0.90	0.21±0.01	0.81±0.16	82.5±6.7
May 18	22.2	1.23±0.02	2.56±0.05	0.60±0.03	79.8±1.0
	43.1	1.61±0.04	0.71±0.01	0.54±0.09	84.1±1.1
	86.2	2.83±0.36	0.18±0.01	0.69±0.06	82.2±9.8
May 19	22.2	1.38±0.03	2.53±0.03	0.57±0.02	79.6±1.3
	43.1	1.86±0.07	0.71±0.01	0.51±0.06	84.7±3.1

Table 8.2 – continued

Date	ν	S	θ_{major}	Ratio	P.A.
	[GHz]	[Jy]	[mas]		[deg]
	86.2	3.68±0.83	0.19±0.02	1.00	-
May 20	22.2	1.16±0.02	2.53±0.02	0.53±0.02	80.2±1.3
	43.1	1.66±0.06	0.72±0.01	0.54±0.06	80.4±1.6
	86.2	3.24±0.37	0.20±0.02	0.54±0.13	86.4±4.4
May 21	22.2	1.42±0.04	2.58±0.02	0.61±0.02	77.2±0.8
	43.1	2.02±0.08	0.72±0.01	0.62±0.06	81.8±3.1
	86.2	4.18±0.50	0.23±0.01	0.69±0.08	80.4±7.7
May 22	22.2	1.36±0.02	2.56±0.03	0.58±0.02	78.9±0.5
	43.1	1.90±0.05	0.72±0.01	0.66±0.06	78.5±1.3
	86.2	3.73±0.73	0.21±0.01	0.54±0.09	84.4±11.8
May 23	22.2	1.37±0.04	2.55±0.03	0.54±0.04	80.7±0.8
	43.1	1.92±0.08	0.72±0.01	0.54±0.06	81.2±1.3
	86.2	3.26±0.57	0.18±0.02	0.62±0.10	77.7±6.1
May 24	22.2	1.35±0.01	2.57±0.01	0.54±0.02	81.1±0.9
	43.1	1.78±0.06	0.68±0.01	0.48±0.06	86.6±2.1
	86.2	2.88±0.54	0.23±0.01	0.50±0.11	92.6±9.6

Note: Listed are the observing date in 2007, observing frequency in [GHz], total flux density in [Jy], major axis of the elliptical Gaussian in [mas], the ratio of the minor axis to the major axis, and the position angle of the major axis.

9 Appendix-C

In this appendix, we show the clean images of NRAO 530 at 22, 43, and 86 GHz obtained during our 10-day observations in 2007 (Figure 9.1). Images from the archival data at 15 GHz are also included (Figure 9.2). Model-fitting results are summarized in Table 9.2. Labels indicate the identification of the Gaussian model fit components, described in Table 9.2

9.1 (1): 22 GHz, 2007/05/15   9.1 (2): 43 GHz, 2007/05/15   9.1 (3): 86 GHz, 2007/05/15

9.1 (4): 22 GHz, 2007/05/16   9.1 (5): 43 GHz, 2007/05/16   9.1 (6): 86 GHz, 2007/05/16
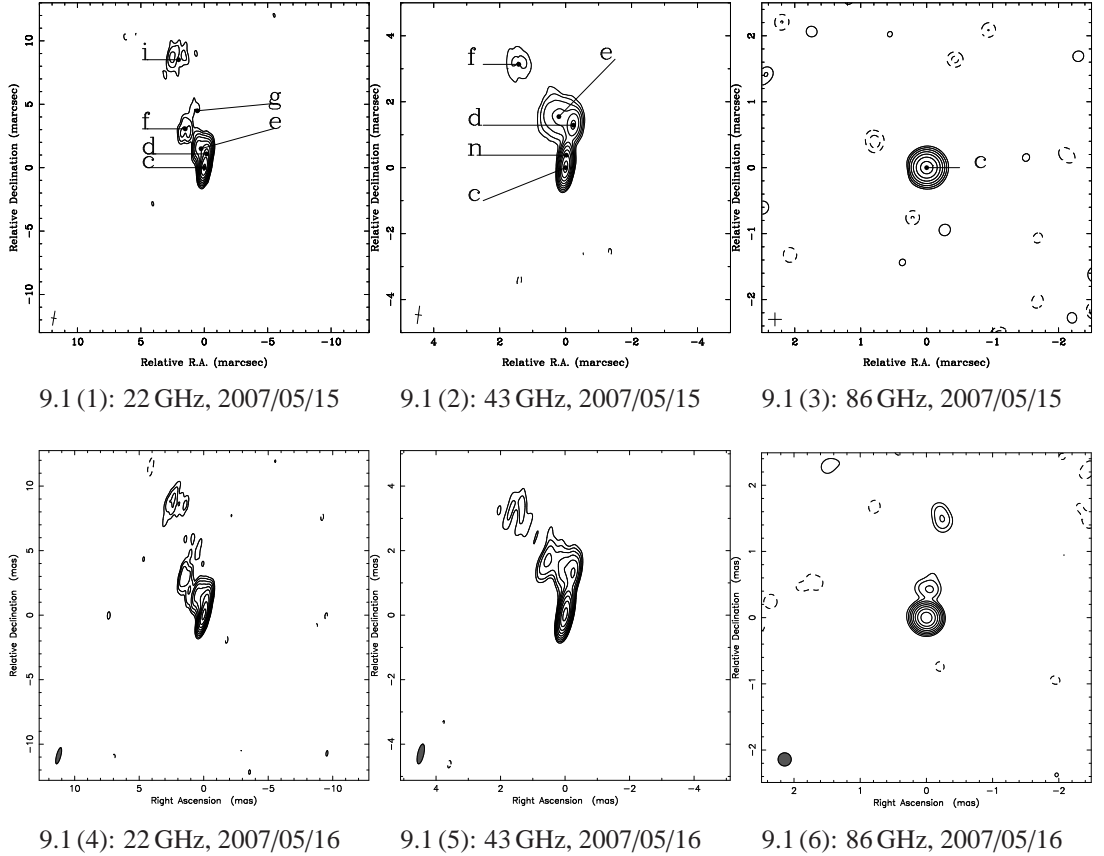
Figure 9.1: Clean images of NRAO 530.

9.1 (7): 22 GHz, 2007/05/17   9.1 (8): 43 GHz, 2007/05/17   9.1 (9): 86 GHz, 2007/05/17

9.1 (10): 22 GHz, 2007/05/18   9.1 (11): 43 GHz, 2007/05/18   9.1 (12): 86 GHz, 2007/05/18

9.1 (13): 22 GHz, 2007/05/19   9.1 (14): 43 GHz, 2007/05/19   9.1 (15): 86 GHz, 2007/05/19

Figure 9.1: *-continued.*

9.1 (16): 22 GHz, 2007/05/20   9.1 (17): 43 GHz, 2007/05/20   9.1 (18): 86 GHz, 2007/05/20

9.1 (19): 22 GHz, 2007/05/21   9.1 (20): 43 GHz, 2007/05/21   9.1 (21): 86 GHz, 2007/05/21

9.1 (22): 22 GHz, 2007/05/22   9.1 (23): 43 GHz, 2007/05/22   9.1 (24): 86 GHz, 2007/05/22

Figure 9.1: *-continued.*

126

9.1 (25): 22 GHz, 2007/05/23

9.1 (26): 43 GHz, 2007/05/23

9.1 (27): 86 GHz, 2007/05/23

9.1 (28): 22 GHz, 2007/05/24

9.1 (29): 43 GHz, 2007/05/24

9.1 (30): 86 GHz, 2007/05/24

Figure 9.1: *-continued.*

9.2 (1): 15 GHz, 1999.71   9.2 (2): 15 GHz, 2000.03   9.2 (3): 15 GHz, 2000.33
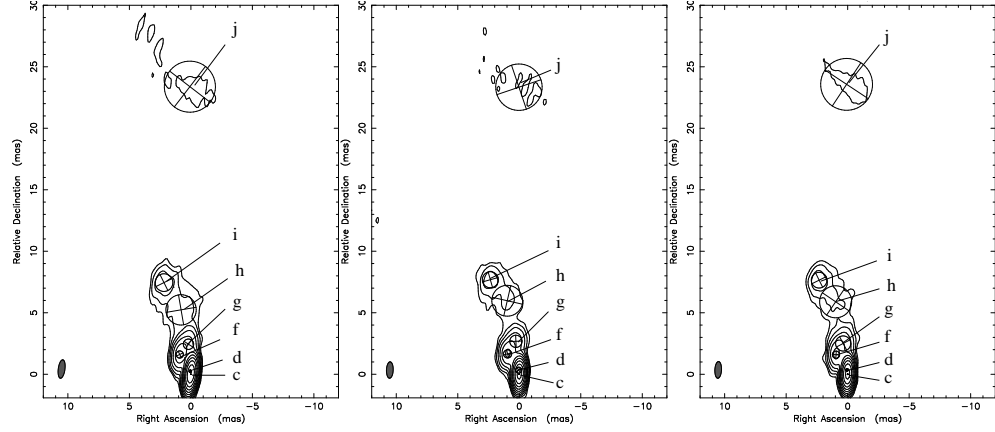
9.2 (4): 15 GHz, 2002.77   9.2 (5): 15 GHz, 2003.26   9.2 (6): 15 GHz, 2003.34.ps
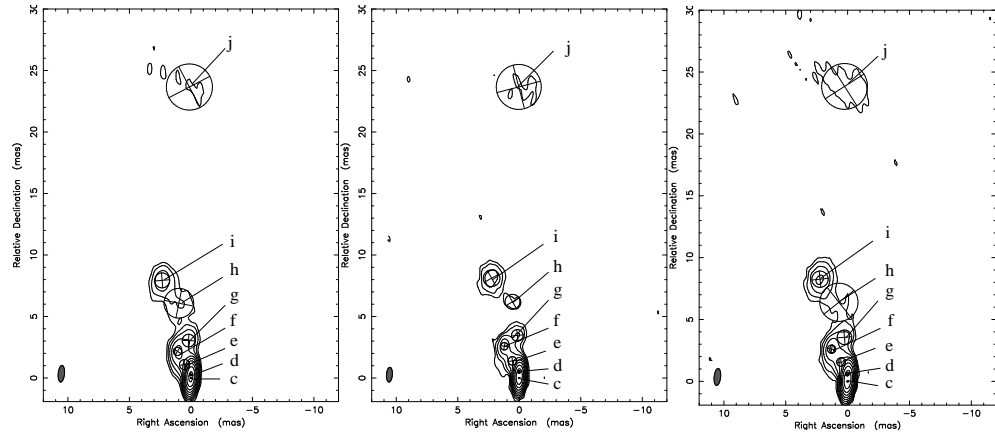
9.2 (7): 15 GHz, 2004.11   9.2 (8): 15 GHz, 2005.22   9.2 (9): 15 GHz, 2005.56

Figure 9.2: Clean images of NRAO 530 at 15 GHz.

128
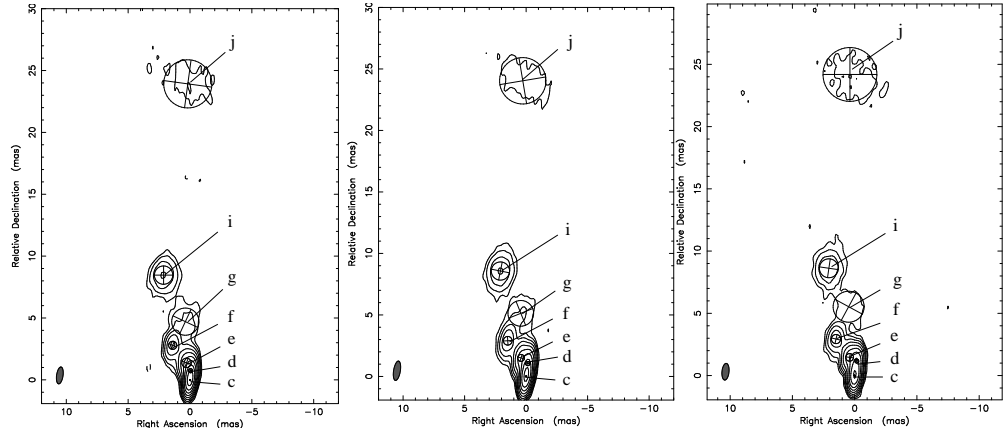
9.2 (10): 15 GHz, 2006.52   9.2 (11): 15 GHz, 2007.10   9.2 (12): 15 GHz, 2007.44
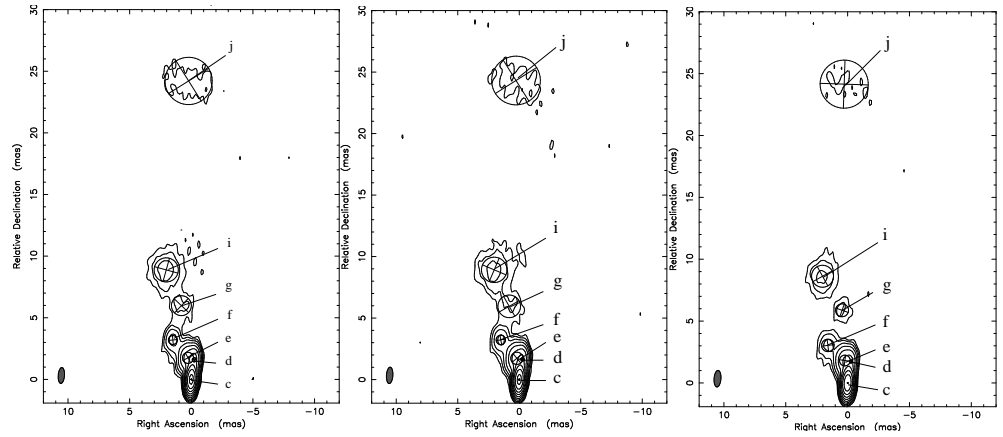
9.2 (13): 15 GHz, 2008.33   9.2 (14): 15 GHz, 2008.54   9.2 (15): 15 GHz, 2008.76
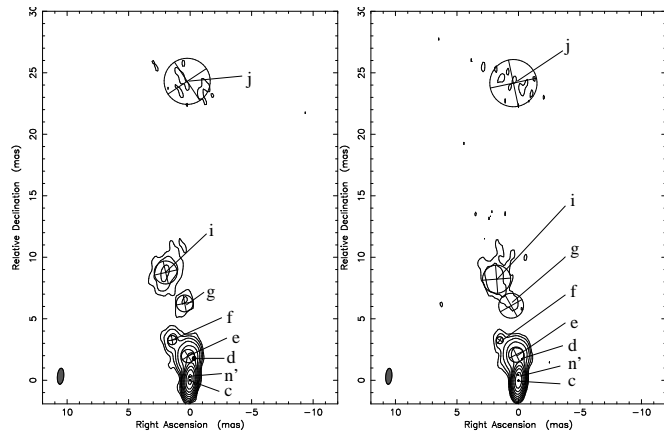
9.2 (16): 15 GHz, 2009.15   9.2 (17): 15 GHz, 2009.48

Figure 9.2: *-continued.*

Table 9.1: Description of VLBA images of NRAO 530 shown in Figure 9.1.

Epoch	ν	S_{peak}	Restoring Beam			Contours
			Major	Minor	P.A.	
	GHz	Jy/beam	mas	mas	deg	
(1)	(2)	(3)	(4)	(5)	(6)	(7)
2007/05/15	22	1.32	1.19	0.344	−12.8	−0.3, 0.3, 0.6, ..., 76.8
	43	1.33	0.537	0.193	−7.7	−0.3, 0.3, 0.6, ..., 76.8
	86	0.74	0.2	0.2	0	−1, 1, 2, ..., 64
2007/05/16	22	1.31	1.29	0.344	−15.0	−0.3, 0.3, 0.6, ..., 76.8
	43	1.33	0.628	0.19	−12.9	−0.3, 0.3, 0.6, ..., 76.8
	86	1.20	0.2	0.2	0	−0.5, 0.5, 1, ..., 64
2007/05/17	22	1.29	1.14	0.367	−9.2	−0.3, 0.3, 0.6, ..., 76.8
	43	1.41	0.794	0.252	−11.2	-0.3, 0.3, 0.6, ..., 76.8
	86	1.06	0.2	0.2	0	−1, 1, 2, ..., 64
2007/05/18	22	1.38	1.24	0.367	−10.0	−0.3, 0.3, 0.6, ..., 76.8
	43	1.44	0.72	0.314	−12.0	−0.3, 0.3, 0.6, ..., 76.8
	86	1.25	0.2	0.2	0	−0.5, 0.5, 1, ..., 64
2007/05/19	22	1.32	1.15	0.374	−10.1	−0.3, 0.3, 0.6, ..., 76.8
	43	1.44	0.83	0.319	−10.0	−0.3, 0.3, 0.6, ..., 76.8
	86	1.04	0.2	0.2	0	−0.5, 0.5, 1, ..., 64
2007/05/20	22	1.27	1.12	0.42	−6.88	−0.3, 0.3, 0.6, ..., 76.8
	43	1.37	0.571	0.186	−8.6	0.3, 0.6, 1.2, ..., 76.8
	86	1.13	0.2	0.2	0	−0.5, 0.5, 1, ..., 64
2007/05/21	22	1.31	1.09	0.403	−5.95	−0.3, 0.3, 0.6, ..., 76.8
	43	1.37	0.604	0.198	−8.03	0.3, 0.6, 1.2, ..., 76.8
	86	1.01	0.2	0.2	0	−0.5, 0.5, 1, ..., 64
2007/05/22	22	1.37	1.26	0.424	−8.68	−0.3, 0.3, 0.6, ..., 76.8
	43	1.41	0.628	0.199	−9.78	0.3, 0.6, 1.2, ..., 76.8
	86	1.04	0.2	0.2	0	−0.5, 0.5, 1, ..., 64
2007/05/23	22	1.34	1.20	0.43	−6.14	−0.3, 0.3, 0.6, ..., 76.8
	43	1.37	0.553	0.197	−7.02	0.3, 0.6, 1.2, ..., 76.8
	86	1.19	0.2	0.2	0	−0.5, 0.5, 1, ..., 64
2007/05/24	22	1.33	1.37	0.405	−11.8	−0.3, 0.3, 0.6, ..., 76.8

Table 9.1 – continued

Epoch	ν	S_{peak}	Restoring Beam			Contours
			Major	Minor	P.A.	
	GHz	Jy/beam	mas	mas	deg	
(1)	(2)	(3)	(4)	(5)	(6)	(7)
	43	1.45	0.663	0.183	−12.8	0.3, 0.6, 1.2, ..., 76.8
	86	1.13	0.2	0.2	0	−0.5, 0.5, 1, ..., 64
1999.71	15	2.07	1.35	0.495	−6.8	0.25, 0.5, 1, ..., 64
2000.03	15	1.83	1.42	0.505	−9.0	−0.25, 0.25 ,0.5, ..., 64
2000.33	15	1.99	1.35	0.509	−2.6	−0.3, 0.3 ,0.6, ..., 76.8
2002.77	15	4.73	1.51	0.547	−7.7	0.1, 0.2 ,0.4, ..., 51.2
2003.26	15	4.15	1.34	0.55	−2.2	0.15, 0.15 ,0.3, ..., 76.8
2003.34	15	4.23	1.36	0.544	−2.8	0.15, 0.3 ,0.6, ..., 76.8
2004.11	15	3.36	1.35	0.519	−5.2	0.15, 0.3 ,0.6, ..., 76.8
2005.22	15	2.81	1.2	0.483	−3.9	−0.2, 0.2 ,0.4, ..., 51.2
2005.56	15	2.29	1.37	0.529	−6.0	0.2, 0.4 ,0.8, ..., 51.2
2006.52	15	1.72	1.38	0.524	−8.3	−0.25, 0.25, 0.5, ..., 64
2007.10	15	1.54	1.59	0.551	−9.3	−0.3, 0.3, 0.6, ..., 76.8
2007.44	15	1.20	1.34	0.568	−5.7	−0.35, 0.35, 0.7, ..., 89.6
2008.33	15	2.76	1.29	0.509	−4.2	−0.15, 0.15, 0.3, ..., 76.8
2008.54	15	2.91	1.33	0.524	−3.7	−0.15, 0.15, 0.3, ..., 76.8
2008.76	15	3.19	1.34	0.559	−4.2	−0.2, 0.2 ,0.4, ..., 51.2
2009.15	15	3.63	1.31	0.524	−5.4	0.15, 0.3, 0.6, ..., 76.8
2009.48	15	3.19	1.30	0.51	−4.5	0.25, 0.5, 1, ..., 64

Note: (1) Epoch, (2) Observing frequency, (3) Peak flux density, (4), (5), (6) Parameters of the restoring elliptical Gaussian beam: the full width at half maximum (FWHM) of the major and minor axes and the position angle (P.A.) of the major axis, (7) Contour levels of the image, expressed as a percentage of the peak intensity.

Table 9.2: Model-fitting results for NRAO 530.

Epoch	Id.	Flux [mJy]	Core Separation [mas]	P.A. [degree]	Size [mas]
		$\nu = 22\,\mathrm{GHz}$			
2007/05/15	c	1332.9±23.6	0.00±0.00	0.0±0.0	0.08±0.01
	d	385.9±40.5	1.10±0.06	−9.5±3.1	0.28±0.02
	e	377.8±72.1	1.52±0.08	9.6±2.9	0.87±0.15
	f	99.1±26.5	3.41±0.10	26.1±1.6	0.81±0.20
	g	29.5±11.2	4.52±0.22	7.0±2.8	0.32±0.09
	i	138.3±44.2	8.75±0.30	13.4±2.0	1.99±0.61
2007/05/16	c	1317.6±60.3	0.00±0.00	0.0±0.0	0.10±0.01
	d	390.3±45.4	1.16±0.06	−9.6±3.0	0.28±0.03
	e	358.2±74.2	1.48±0.08	10.8±3.0	0.83±0.16
	f	76.1±19.8	3.28±0.06	28.1±1.1	0.56±0.12
	g	52.6±23.6	4.56±0.31	9.4±3.8	1.49±0.61
	i	116.7±38.6	8.94±0.26	13.6±1.6	1.64±0.52
2007/05/17	c	1289.7±43.2	0.00±0.00	0.0±0.0	0.09±0.01
	d	435.9±54.6	1.15±0.06	−9.6±3.0	0.32±0.03
	e	298.9±58.2	1.54±0.07	13.2±2.5	0.78±0.14
	f	98.8±24.5	3.27±0.10	26.9±1.8	0.88±0.20
	g	26.3±16.2	4.82±0.20	6.4±2.4	0.41±0.19
	i	123.0±42.1	8.88±0.28	13.0±1.8	1.74±0.57
2007/05/18	c	1387.8±30.8	0.00±0.00	0.0±0.0	0.14±0.01
	d	413.1±36.2	1.17±0.06	−10.7±2.9	0.25±0.02
	e	345.6±63.1	1.54±0.06	10.6±2.2	0.74±0.12
	f	97.8±20.9	3.13±0.06	29.6±1.1	0.48±0.08
	g	14.2±13.2	5.19±0.16	7.3±1.7	0.54±0.31
	i	83.3±29.1	8.87±0.21	15.1±1.3	1.29±0.42
2007/05/19	c	1313.5±27.7	0.00±0.00	0.0±0.0	0.09±0.01
	d	392.4±25.0	1.18±0.06	−9.9±2.9	0.27±0.01
	e	352.3±62.8	1.42±0.07	10.8±2.7	0.82±0.13
	f	89.0±16.9	3.31±0.06	27.3±1.0	0.70±0.12
	g	58.3±27.6	4.31±0.39	8.4±5.2	1.78±0.79

Table 9.2 – continued

Epoch	Id.	Flux	Core Separation	P.A.	Size
		[mJy]	[mas]	[degree]	[mas]
	i	121.1±35.8	8.89±0.20	13.4±1.6	1.73±0.49
2007/05/20	c	1249.7±28.4	0.00±0.00	0.0±0.0	0.09±0.01
	d	388.1±22.8	1.16±0.06	−10.7±3.0	0.30±0.01
	e	364.1±52.5	1.43±0.06	11.2±2.4	0.85±0.10
	f	94.1±23.0	3.33±0.08	26.6±1.3	0.73±0.15
	g	22.0±16.7	4.72±0.20	6.5±2.4	0.35±0.20
	i	100.5±30.1	8.95±0.20	14.3±1.3	1.43±0.39
2007/05/21	c	1298.3±42.6	0.00±0.00	0.0±0.0	0.08±0.01
	d	409.7±47.1	1.19±0.06	−9.4±2.9	0.32±0.03
	e	302.6±57.5	1.49±0.07	11.6±2.7	0.83±0.14
	f	89.7±23.6	3.35±0.10	26.6±1.7	0.82±0.19
	g	34.3±12.7	4.58±0.26	7.0±3.2	0.42±0.12
	i	112.0±36.9	8.91±0.26	13.6±1.7	1.66±0.52
2007/05/22	c	1336.8±41.5	0.00±0.00	0.0±0.0	0.06±0.01
	d	403.2±20.2	1.22±0.06	−9.8±2.8	0.24±0.01
	e	338.1±54.8	1.45±0.06	11.8±2.4	0.74±0.11
	f	82.6±11.3	3.22±0.06	27.9±1.1	0.55±0.06
	g	80.3±30.5	4.03±0.36	10.9±5.1	2.02±0.72
	i	118.5±29.1	9.04±0.18	13.0±1.1	1.56±0.36
2007/05/23	c	1344.6±34.4	0.00±0.00	0.0±0.0	0.09±0.01
	d	399.8±31.5	1.22±0.06	−10.4±2.8	0.26±0.02
	e	328.5±40.2	1.48±0.06	11.4±2.3	0.74±0.08
	f	79.9±15.2	3.24±0.06	27.9±1.1	0.56±0.09
	g	79.1±24.5	3.86±0.24	10.5±3.6	1.73±0.49
	i	140.2±30.5	8.88±0.19	12.9±1.2	1.83±0.37
2007/05/24	c	1294.6±37.0	0.00±0.00	0.0±0.0	0.08±0.01
	d	364.7±41.3	1.15±0.06	−10.0±3.0	0.25±0.02
	e	416.2±75.9	1.48±0.08	7.7±3.2	0.98±0.17
	f	89.5±21.9	3.35±0.07	28.7±1.1	0.63±0.13
	g	39.9±19.2	4.37±0.17	8.1±2.2	0.83±0.34

Table 9.2 – continued

Epoch	Id.	Flux [mJy]	Core Separation [mas]	P.A. [degree]	Size [mas]
	i	118.9±34.3	8.92±0.22	12.8±0.4	1.63±0.45
		$\nu = 43\,\text{GHz}$			
2007/05/15	c	1258.0±60.7	0.00±0.00	0.0±0.0	0.03±0.01
	n	272.9±22.4	0.38±0.03	−3.2±4.5	0.08±0.01
	d	221.2±27.7	1.31±0.03	−10.4±1.3	0.21±0.02
	e	250.3±40.2	1.56±0.05	7.5±2.0	0.70±0.11
	f	56.1±20.2	3.44±0.12	24.4±2.0	0.68±0.24
2007/05/16	c	1205.8±52.9	0.00±0.00	0.0±0.0	0.04±0.01
	n	295.5±17.4	0.35±0.02	−3.4±4.9	0.10±0.01
	d	217.7±42.0	1.32±0.03	−10.2±1.3	0.22±0.04
	e	245.8±49.2	1.57±0.07	8.6±2.5	0.72±0.14
	f	48.9±16.8	3.50±0.11	24.9±1.8	0.70±0.23
2007/05/17	c	1303.1±47.9	0.00±0.00	0.0±0.0	0.01±0.01
	n	233.1±19.2	0.42±0.03	−5.1±4.1	0.12±0.01
	d	235.9±32.8	1.34±0.03	−9.4±1.3	0.23±0.02
	e	195.5±35.4	1.67±0.06	11.1±1.9	0.67±0.11
	f	56.8±14.1	3.47±0.07	25.6±1.1	0.60±0.14
2007/05/18	c	1303.1±29.8	0.00±0.00	0.0±0.0	0.02±0.01
	n	261.9±22.0	0.39±0.03	−2.9±4.4	0.11±0.01
	d	276.4±40.4	1.36±0.03	−8.3±1.3	0.27±0.03
	e	181.0±41.3	1.70±0.07	12.5±2.3	0.66±0.14
	f	55.6±20.8	3.45±0.13	25.2±2.1	0.73±0.25
2007/05/19	c	1269.8±33.2	0.00±0.00	0.0±0.0	0.04±0.01
	n	302.8±19.1	0.36±0.03	−4.0±4.8	0.12±0.01
	d	261.9±36.6	1.36±0.03	−8.5±1.3	0.25±0.02
	e	181.1±35.6	1.67±0.06	11.9±2.0	0.66±0.11
	f	57.0±13.2	3.50±0.07	25.0±1.2	0.67±0.14
2007/05/20	c	1274.3±18.2	0.00±0.00	0.0±0.0	0.02±0.01
	n	234.4±22.0	0.37±0.03	−3.0±4.6	0.05±0.01
	d	206.9±25.7	1.33±0.03	−10.5±1.3	0.20±0.02
	e	253.5±57.9	1.56±0.08	8.0±2.9	0.73±0.15

Epoch	Id.	Flux	Core Separation	P.A.	Size
		[mJy]	[mas]	[degree]	[mas]
	f	51.9±17.7	3.33±0.10	25.0±1.8	0.65±0.20
2007/05/21	c	1287.2±51.5	0.00±0.00	0.0±0.0	0.01±0.01
	n	251.1±16.2	0.36±0.03	−3.4±4.8	0.06±0.01
	d	239.4±32.1	1.34±0.03	−10.0±1.3	0.22±0.02
	e	226.2±55.1	1.64±0.08	9.9±2.9	0.71±0.16
	f	52.3±15.7	3.34±0.10	25.5±1.7	0.70±0.20
2007/05/22	c	1265.3±11.6	0.00±0.00	0.0±0.0	0.02±0.01
	n	241.7±21.8	0.37±0.03	−3.2±4.6	0.06±0.01
	d	220.1±30.2	1.34±0.03	−10.1±1.3	0.21±0.02
	e	246.8±58.8	1.57±0.09	9.0±3.1	0.75±0.17
	f	52.8±14.9	3.18±0.08	24.6±1.5	0.63±0.17
2007/05/23	c	1308.5±18.9	0.00±0.00	0.0±0.0	0.02±0.01
	n	214.4±29.7	0.39±0.03	−2.7±4.4	0.02±0.01
	d	212.8±27.6	1.33±0.03	−10.2±1.3	0.20±0.02
	e	243.7±38.4	1.61±0.06	8.7±2.0	0.76±0.11
	f	53.3±17.0	3.42±0.11	25.6±1.9	0.76±0.23
2007/05/24	c	1337.4±19.0	0.00±0.00	0.0±0.0	0.03±0.01
	n	210.5±13.4	0.37±0.03	−2.3±4.6	0.02±0.01
	d	239.1±24.6	1.34±0.03	−10.5±1.3	0.20±0.02
	e	245.5±32.9	1.54±0.05	10.2±2.0	0.83±0.11
	f	50.5±14.5	3.43±0.09	24.6±1.5	0.67±0.18
	II	$\nu = 86\,\text{GHz}$			
2007/05/15	c	1214.4±186.3	0.00±0.00	0.0 ±0.0	0.16±0.02
2007/05/16	c	1187.5±106.8	0.00±0.00	0.0 ±0.0	0.06±0.01
	n	73.1±37.0	0.45±0.02	−9.6±2.5	0.08±0.01
	d	107.4±21.4	1.55±0.05	−9.7±1.8	0.08±0.02
2007/05/17	c	1077.2±94.0	0.00±0.00	0.0±0.0	0.03±0.01
	n	87.2±39.3	0.37±0.02	−6.7±3.1	0.06±0.01
	d	116.6±49.0	1.39±0.05	−4.9±2.1	0.08±0.02
2007/05/18	c	1194.6±70.3	0.00±0.00	0.0±0.0	0.05±0.01
	n	96.9±37.8	0.35±0.04	−4.5±6.0	0.12±0.07

Table 9.2 – continued

Epoch	Id.	Flux [mJy]	Core Separation [mas]	P.A. [degree]	Size [mas]
	d	109.8±56.2	1.55±0.07	−0.5±2.6	0.30±0.14
2007/05/19	c	1088.2±39.0	0.00±0.00	0.0±0.0	0.03±0.01
	n	59.4±11.4	0.37±0.02	−9.3±3.1	0.07±0.01
	d	114.6±52.4	1.32±0.10	−11.7±4.1	0.44±0.19
2007/05/20	c	1170.0±54.9	0.00±0.00	0.0±0.0	0.04±0.01
	n	72.2±39.2	0.35±0.02	−6.8±3.3	0.03±0.01
	d	53.9±27.1	1.47±0.05	−5.4±1.9	0.06±0.02
2007/05/21	c	1067.4±88.2	0.00±0.00	0.0±0.0	0.05±0.01
	n	71.0±36.8	0.31±0.02	−4.3±3.9	0.09±0.04
	d	53.4±24.5	1.43±0.05	−5.6±2.0	0.15±0.05
2007/05/22	c	1091.5±81.2	0.00±0.00	0.0±0.0	0.04±0.01
	n	125.9±49.7	0.43±0.06	−12.2±8.4	0.35±0.13
	d	86.3±30.4	1.33±0.04	−12.3±1.6	0.24±0.08
2007/05/23	c	1192.8±75.8	0.00±0.00	0.0±0.0	0.01±0.01
	n	55.2±29.4	0.35±0.02	−7.3±3.3	0.04±0.01
	d	142.5±40.7	1.39±0.05	−7.8±2.1	0.21±0.05
2007/05/24	c	1131.2±60.9	0.00±0.00	0.0±0.0	0.01±0.01
	n	75.7±29.3	0.36±0.02	−0.9±3.2	0.03±0.01
	d	116.1±47.9	1.57±0.11	4.8±3.9	0.59±0.21
		(II) 15 GHz			
1999.71	c	2013.6±48.7	0.00±0.00	0.0±0.0	0.09±0.01
	d	297.6±13.9	0.47±0.06	36.8±7.3	0.25±0.01
	f	145.5±12.0	1.10±0.06	29.1±3.1	0.09±0.01
	g	483.2±55.8	1.55±0.06	6.3±2.2	0.93±0.10
	x	36.5±9.7	3.00±0.06	16.0±1.1	0.43±0.09
	h	217.6±43.2	5.82±0.20	13.4±1.9	2.03±0.39
	j	108.9±46.3	23.06±0.93	1.0±2.3	4.42±1.86
2000.03	c	1679.3±31.3	0.00±0.00	0.0±0.0	0.06±0.01
	d	303.5±25.5	0.37±0.06	18.6±9.2	0.45±0.03
	f	228.7±27.8	1.12±0.06	31.0±3.1	0.35±0.03
	g	320.0±33.2	1.88±0.06	6.2±1.8	0.78±0.07

Table 9.2 – continued

Epoch	Id.	Flux	Core Separation	P.A.	Size
		[mJy]	[mas]	[degree]	[mas]
	x	22.9±6.8	2.64±0.06	26.4±1.3	0.11±0.02
	h	197.1±43.1	5.95±0.24	12.8±2.3	2.30±0.48
	j	98.2±43.5	23.79±1.31	0.6±3.1	5.94±2.61
2000.33	c	1691.1±51.2	0.00±0.00	0.0±0.0	0.07±0.01
	d	489.5±25.3	0.32±0.06	17.0±10.6	0.38±0.02
	f	275.1±27.9	1.24±0.06	29.7±2.8	0.40±0.03
	g	391.6±42.3	2.01±0.06	6.3±1.7	0.85±0.08
	x	19.3±8.3	2.66±0.06	24.5±1.3	0.06±0.02
	h	219.6±40.8	5.95±0.19	13.4±1.8	2.12±0.38
	j	119.6±43.5	23.18±0.87	0.6±2.2	4.89±1.75
2002.77	c	4150.2±81.5	0.00±0.00	0.0±0.0	0.03±0.01
	d	693.7±59.5	0.25±0.06	9.7±13.5	0.20±0.01
	f	390.5±41.1	1.85±0.06	29.4±1.9	0.59±0.05
	g	209.3±22.5	2.45±0.06	4.6±1.4	0.85±0.08
	h	129.8±23.0	5.30±0.21	8.7±2.3	2.47±0.42
	i	118.6±27.6	7.77±0.15	16.4±1.1	1.44±0.31
	j	128.1±33.3	23.38±0.53	0.2±1.3	4.15±1.07
2003.26	c	3870.0±88.9	0.00±0.00	0.0±0.0	0.04±0.01
	d	494.0±26.3	0.34±0.06	7.8±10.0	0.48±0.02
	f	374.0±36.6	1.91±0.06	29.8±1.8	0.67±0.05
	g	198.5±31.8	2.69±0.07	5.9±1.5	0.99±0.14
	h	138.2±28.6	6.06±0.25	9.3±2.4	2.51±0.50
	i	118.2±25.6	8.04±0.13	17.0±0.9	1.31±0.26
	j	136.4±42.6	23.34±0.58	0.1±1.4	3.78±1.16
2003.34	c	3907.3±79.1	0.00±0.00	0.0±0.0	0.05±0.01
	d	456.4±31.4	0.36±0.06	8.8±9.5	0.21±0.01
	f	348.7±38.3	1.85±0.06	30.8±1.9	0.59±0.05
	g	295.0±45.0	2.53±0.09	8.3±1.9	1.23±0.17
	h	146.0±25.9	5.97±0.22	9.4±2.2	2.61±0.45
	i	131.9±25.9	8.00±0.11	16.9±0.8	1.28±0.23

Table 9.2 – continued

Epoch	Id.	Flux [mJy]	Core Separation [mas]	P.A. [degree]	Size [mas]
	j	176.1±51.8	23.57±0.61	0.2±1.5	4.22±1.23
2004.11	c	2190.6±39.0	0.00±0.00	0.0±0.0	0.05±0.01
	d	1315.0±31.0	0.27±0.06	6.9±12.5	0.11±0.01
	e	145.1±17.2	1.21±0.06	25.3±2.8	0.83±0.09
	f	167.5±16.1	2.42±0.06	26.8±1.4	0.66±0.05
	g	107.9±19.9	3.05±0.09	3.6±1.6	1.03±0.17
	h	96.5±19.1	6.16±0.23	9.1±2.1	2.42±0.46
	i	111.4±18.2	8.28±0.09	16.4±0.6	1.22±0.18
	j	108.1±31.0	23.66±0.53	0.3±1.3	3.75±1.06
2005.22	c	2290.5±74.5	0.00±0.00	0.0±0.0	0.09±0.01
	d	874.2±48.5	0.49±0.06	2.0±7.0	0.21±0.01
	e	141.0±21.6	1.50±0.06	21.5±2.3	0.69±0.09
	f	138.9±19.0	2.85±0.06	25.2±1.2	0.60±0.07
	g	69.3±16.8	3.47±0.11	2.6±1.7	0.94±0.21
	h	31.7±12.9	6.22±0.23	5.1±2.1	1.21±0.46
	i	143.6±29.6	8.42±0.13	15.5±0.9	1.36±0.27
	j	133.8±46.1	23.67±0.63	0.1±1.5	3.66±1.25
2005.56	c	1845.7±53.1	0.00±0.00	0.0±0.0	0.09±0.01
	d	795.9±40.0	0.58±0.06	1.9±5.9	0.26±0.01
	e	139.4±23.1	1.65±0.06	18.8±2.1	0.70±0.10
	f	139.9±17.6	2.91±0.06	26.5±1.2	0.67±0.07
	g	70.3±16.6	3.57±0.13	4.1±2.0	1.18±0.26
	h	69.0±26.7	6.43±0.59	6.3±5.3	3.09±1.19
	i	148.5±23.7	8.55±0.10	15.1±0.7	1.32±0.20
	j	131.1±40.4	23.84±0.56	0.6±1.4	3.71±1.13
2006.52	c	1499.6±30.5	0.00±0.00	0.0±0.0	0.05±0.01
	d	502.0±22.9	0.74±0.06	−3.8±4.6	0.33±0.01
	e	265.8±24.4	1.41±0.06	11.6±2.4	0.76±0.06
	f	132.2±15.7	3.12±0.06	26.6±1.1	0.66±0.07
	g	89.5±23.9	4.72±0.28	4.6±3.4	2.20±0.57
	i	157.8±23.5	8.73±0.10	14.2±0.7	1.48±0.21

Table 9.2 – continued

Epoch	Id.	Flux	Core Separation	P.A.	Size
		[mJy]	[mas]	[degree]	[mas]
	j	132.6±40.1	23.92±0.58	0.4±1.4	3.90±1.17
2007.10	c	1378.7±51.5	0.00±0.00	0.0±0.0	0.07±0.01
	d	553.0±30.8	1.06±0.06	−7.3±3.2	0.35±0.01
	e	282.7±25.8	1.56±0.06	15.3±2.2	0.56±0.04
	f	124.7±17.3	3.26±0.06	27.2±1.1	0.70±0.08
	g	66.8±14.5	5.15±0.22	4.8±2.4	2.09±0.43
	i	152.5±21.5	8.82±0.10	13.7±0.6	1.48±0.19
	j	124.4±35.3	24.04±0.53	0.6±1.3	3.77±1.06
2007.44	c	1138.4±60.1	0.00±0.00	0.0±0.0	0.07±0.01
	d	545.9±20.6	1.17±0.06	−8.6±2.9	0.31±0.01
	e	310.9±47.4	1.52±0.06	15.4±2.3	0.62±0.09
	f	109.6±19.5	3.29±0.06	27.0±1.0	0.74±0.11
	g	67.1±19.4	5.55±0.35	5.0±3.6	2.49±0.70
	i	139.5±22.7	8.87±0.12	13.5±0.8	1.52±0.23
	j	121.9±37.0	24.19±0.65	0.9±1.5	4.33±1.30
2008.33	c	2765.9±57.8	0.00±0.00	0.0±0.0	0.04±0.01
	d	357.8±30.3	1.61±0.06	−8.8±2.1	0.33±0.02
	e	419.9±35.6	1.77±0.06	8.7±1.9	0.90±0.07
	f	89.8±15.0	3.53±0.06	25.1±1.0	0.72±0.11
	g	52.4±12.6	6.04±0.18	7.6±1.7	1.61±0.36
	i	157.9±27.5	9.11±0.16	12.9±1.0	1.96±0.33
	j	136.8±32.0	24.21±0.44	0.5±1.0	3.84±0.89
2008.54	c	2928.7±62.2	0.00±0.00	0.0±0.0	0.07±0.01
	d	225.0±24.5	1.65±0.06	−9.3±2.1	0.26±0.02
	e	516.2±34.8	1.74±0.06	6.3±2.0	0.99±0.06
	f	87.5±12.8	3.56±0.06	24.9±1.0	0.76±0.10
	g	60.6±15.7	6.01±0.22	7.8±2.1	1.84±0.45
	i	161.2±30.0	9.15±0.18	12.9±1.2	2.07±0.37
	j	143.0±34.9	24.32±0.48	0.6±1.1	3.96±0.95
2008.76	c	3197.9±39.9	0.00±0.00	0.0±0.0	0.05±0.01
	d	155.7±12.8	1.75±0.06	−9.1±2.0	0.22±0.01

Table 9.2 – continued

Epoch	Id.	Flux	Core Separation	P.A.	Size
		[mJy]	[mas]	[degree]	[mas]
	e	456.9±33.9	1.83±0.06	6.9±1.9	0.87±0.06
	f	83.0±15.9	3.43±0.09	27.7±1.4	1.01±0.17
	g	42.4±13.6	5.89±0.15	4.4±1.4	1.05±0.29
	i	160.1±29.7	8.86±0.16	13.2±1.0	1.78±0.31
	j	140.1±41.5	24.15±0.57	0.7±1.3	3.89±1.14
2009.15	c	2929.0±73.9	0.00±0.00	0.0±0.0	0.09±0.01
	n′	842.8±42.8	0.28±0.06	8.1±12.1	0.03±0.01
	d	89.2±19.2	1.80±0.06	−10.3±1.9	0.29±0.05
	e	489.0±57.5	1.97±0.06	4.9±1.7	1.07±0.12
	f	65.3±25.2	3.58±0.13	24.1±2.0	0.75±0.26
	g	43.3±16.8	6.26±0.25	4.0±2.3	1.36±0.51
	i	154.1±48.9	8.99±0.29	12.8±1.9	1.87±0.58
	j	126.4±53.5	24.31±0.79	0.6±1.9	3.75±1.57
2009.48	c	3125.8±86.9	0.00±0.00	0.0±0.0	0.09±0.01
	n′	166.3±32.2	0.46±0.06	2.9±7.4	0.06±0.01
	d	41.9±9.3	1.78±0.06	−9.4±1.9	0.11±0.02
	e	478.4±48.5	2.11±0.06	5.0±1.6	1.24±0.12
	f	39.4±9.5	3.65±0.07	24.7±1.1	0.67±0.14
	g	38.4±11.5	6.47±0.12	6.1±1.0	0.89±0.23
	i	166.0±38.6	8.83±0.26	12.9±1.7	2.32±0.52
	j	134.3±40.5	24.27±0.57	1.0±1.3	3.84±1.14

10 Erklärung

Ich versichere, daß ich die von mir vorgelegte Dissertation selbständig angefertigt, die benutzen Quellen und Hilfsmittel vollständig angegeben und die Stellen der Arbeit - einschließlich Tabellen, Karten und Abbildungen -, die anderen Werken im Wortlaut oder dem Sinn nach entnommen sind, in jedem Einzelfall als Entlehnung kenntlich gemacht habe; daß diese Dissertation noch keiner anderen Fakultät oder Universität zur Prüfung vorgelegen hat; daß sie - abgesehen von unten angegebenen Teilpublikationen - noch nicht veröffentlicht worden ist sowie, daß ich eine solche Veröffentlichung vor Abschluß des Promotionsverfahrens nicht vornehmen werde. Die Bestimmungen dieser Promotionsverfahrens sind mir bekannt. Die von mir vorgelegte Dissertation ist von Prof. Dr. Andreas Eckart betreut worden.

Köln, den 6.5.2010

Teilpublikationen:

Lu, R.-S., Krichbaum, T.P., Eckart, A., König, S., Kunneriath, D., Witzel, G., Witzel, A., & Zensus, J.A., "Multi-wavelength VLBI Observations of Sagittarius A*", submitted to A&A.

Lu, R.-S., Krichbaum, T.P., Eckart, A., König, S., Kunneriath, D., Witzel, G., Witzel, A., & Zensus, J.A., "High-frequency VLBI observations of Sgr A* during a multi-frequency campaign in May 2007" , Journal of Physics: Conference Series, Volume 131, Issue 1, pp. 012059 (2008)

Lu, R.-S., Shen, Z.-Q., Krichbaum, T.P., Alef, W., Iguchi, S., Kameno, S., & Titus, M., "Millimeter VLBI Observations of PKS 1749+096", in: The Central Engine of Active Galactic Nuclei, ASP Conference Series, Vol. 373, proceedings of the conference held 16 -21 October, 2006 at Xi'an Jioatong University, Xi'an, China. Edited by Luis C. Ho and Jian-Min Wang, 2007, ASPC, 373, p. 237.

11 Curriculum Vitae

Persönliche Daten

Name: Ru-Sen Lu

Geburtstdatum: 07. 20. 1978
Geburtsort: Hebei, China
Staatsangehörigkeit: chinesisch
Familienstand: Verheiratet

Anschrift:

Ru-Sen Lu
Max-Planck-Institut für Radioastronomie
Auf dem Hügel 69
53121 Bonn Germany
+49-228525358
rslu@mpifr-bonn.mpg.de

Schulische und universitäre Ausbildung:

September 1997-June 2001:

Pädagogische Universität Hebei, Physikstudium

September 2001-June 2003:

Hebei Huanghua high school, Physiklehrer

seit September 2003:

Shanghai Astronomical Observatory, Chinese Academic of Sciences, Doktorand

Mitglied der Graduate School of the Chinese Academy of Sciences, Beijing

seit June 2007: Doktorand in der VLBI-Gruppe des Max-Planck- Instituts für Radioastronomie in Bonn unter Betreuung von Dr. Thomas Krichbaum, Prof. Dr. J. Anton. Zensus und Prof. Dr. Andreas Eckart.

Mitglied der International Max Planck Research School for Astronomy and Astrophysics (IMPRS)